

RENSIT: RadioElectronics. NanoSystems. Information Technologies

Journal "Radioelectronics. Nanosystems. Information Technologies" (abbr. RENSIT) publishes original articles, reviews and brief reports, not previously published, on topical problems in **radioelectronics (including biomedical) and fundamentals of information, nano- and biotechnologies and adjacent areas of physics and mathematics.**

Designed for **researchers, graduate students, physics students of senior courses and teachers.**
It turns out **2 times a year** (that includes 2 issues)

Authors of journal are academicians, corresponding members and foreign members of Russian Academy of Natural Sciences (RANS) and their colleagues,

as well as other russian and foreign authors on presentation of their manuscripts by the members of RANS, which can be obtained by authors before sending articles to editors.

And also after its receiving - on recommendation of a member of editorial board of journal, or another member of Academy of Natural Sciences, that gave her opinion on article at request of editor.

The editors will accept articles in both **Russian and English** languages.

Articles are internally peer reviewed (**double-blind peer review**) by members of the Editorial Board.
Some articles undergo external review, if necessary.

Journal RENSIT is included in the **DB SCOPUS, EBSCO Publishing**, in the international abstracts database - **Ulrich's International Periodicals Directory**,(USA, New York, <http://www.ulrichsweb.com>), in the **AJ and DB VINITI RAS** (<http://wwwviniti.ru>), and DB **Russian Science Citation Index (RSCI)** (http://elibrary.ru/project_risc.asp).

Full-text content is posted in the DB of the **Russian Scientific Electronic Library**

- information resource on the Internet <http://elibrary.ru> and is available for registered users.

And also - in Open Access **CyberLeninka NEB** of Russian Federation <http://cyberleninka.ru>.

On journal's website <http://www.rensit.ru> posted metadata publications

and **RENSIT: Radioelectronics. Nanosystems. Infomation Technologies - english version** (cover-to-cover translation) of journal, which is a party to **CrossRef**.

The founder - the **Russian Academy of Natural Sciences**

Publisher - Publishing Center of the Russian Academy of Natural Sciences

Publisher Address: 119002 Moscow, per. Sivtsev Vrazhek 29/16

CONTENTS

RADIOLOCATION

INTENSITY OF ELECTROMAGNETIC WAVE INTO LAYERS WITH FLUCTUATIONS OF DIELECTRIC PERMITTIVITY

Gennady I. Grigor'ev, Tatiana M. Zaboronkova, Lev P. Kogan 3

RADIOELECTRONICS

THERMAL DEFORMATION MODEL OF THE SUBMODULE OF THE X-BAND OUTPUT POWER AMPLIFIER

Alexander M. Hodakov, Ruslan G. Tarasov, Vyacheslav A. Sergeev, Alexander A. Kulikov 13

ANALYSIS OF THE PROBABILISTIC CHARACTERISTICS OF THE ELECTRICAL PARAMETERS OF A BROADBAND BALANCED MIXER OF MICROWAVE RADIO SIGNALS BASED ON RESONANT TUNNELING DIODES AND AN ASSESSMENT OF ITS RELIABILITY

Kirill V. Cherkasov, Ivan A. Romanov, Sergey A. Meshkov, Vasily D. Shashurin . 19
CONTROLLABLE INDUCTORS AND TRANSFORMERS BASED ON FERROMAGNET-PIEZOELECTRIC HETEROSTRUCTURES

Leonid Yu. Fetisov, Dmitry V. Chashin, Yuri K. Fetisov 27

NANOSYSTEMS

SYNTHESIS AND STUDY OF COMPOSITE BASED ON POROUS ANODIC ALUMINA MODIFIED BY SILVER NANOWIRES

Mikhail Yu. Vasilkov, Ilya N. Mikhailov, Alexander E. Isaev, David Z. Safoshkin, Igor D. Kosobudskii, Nikolai M. Ushakov 39

NUCLEAR PHYSICS OF PLASMA AND CONDENSED MATTER

LENR AS A MANIFESTATION OF WEAK NUCLEAR INTERACTIONS. NEW APPROACH TO CREATING LENR REACTORS

Alexander G. Parkhomov, Roman V. Karabanov 45
HOT LASER FUSION OR LOW TEMPERATURE NUCLEAR REACTIONS? ANALYSIS AND CURRENT PROSPECTS OF THE FIRST EXPERIMENTS ON LASER FUSION

Vladimir I. Vysotskii, Alla A. Kornilova Mykhaylo V. Vysotskyy 59

INFORMATION TECHNOLOGIES

THE STUDY OF DYNAMICAL PROCESSES IN PROBLEMS OF MESOFRACTURE LAYERS EXPLORATION SEISMOLOGY BY METHODS OF MATHEMATICAL AND PHYSICAL SIMULATION

Maxim V. Muratov, Polina V. Stognii, Igor B. Petrov, Alexey A. Anisimov, Nazim A. Karaev 71

MATHEMATICAL MODELING OF TEMPERATURE CHANGES IMPACT ON ARTIFICIAL ICE ISLANDS

Maxim V. Muratov, Vladimir A. Biryukov, Denis S. Konov, Igor B. Petrov . 79
SOFTWARE ARCHITECTURE FOR DISPLAY CONTROLLER AND OPERATING SYSTEM INTERACTION

Konstantin V. Pugin, Kirill A. Mamrosenko, Alexander M. Giatsintov 87
THE PROBLEM OF INCREASING THE CAPACITY OF MOBILE COMMUNICATION CHANNELS AND POSSIBLE SOLUTIONS

Andrey S. Tyutyunik, Alexey A. Badashev, Vladimir S. Gurchenko 95

IN MEMORIAM

IN MEMORY OF ARKADY B. TSEPELEV 104

CRONICLE

GRAPHENE OXIDE IS A NEW ELECTRODE
NANOMATERIAL FOR CHEMICAL CURRENT SOURCES

Denis Yu. Kornilov 105



RUSSIAN ACADEMY
OF NATURAL SCIENCES

DEPARTMENT OF
RADIOELECTRONICS,
NANOPHYSICS AND
INFORMATION TECHNOLOGIES
PROBLEMS

REN SIT:

RADIOELECTRONICS.
NANOSYSTEMS.
INFORMATION
TECHNOLOGIES.

2021, VOL. 13, № 1

FOUNDED IN 2009
4 ISSUES PER YEAR
MOSCOW

Editor-in-Chief

Vладимир И. ГРАЧЕВ

grachev@cprire.ru

Deputy Chief Editor

Alexander S. Ilyushin, DrSci, MSU

Deputy Chief Editor

Sergey P. Gubin, DrSci, IGIC RAS

Executive Secretary

Rostislav V. Belyaev, PhD, IRE RAS

belyaev@cprire.ru

EDITORIAL BOARD

Anatoly V. Andreev, DrSci, MSU
Vladimir A. Bushuev, DrSci, MSU
Vladimir A. Cherepenin, DrSci, c-mRAS, IRE
Alexander S. Dmitriev, DrSci, IRE
Yuri K. Fetisov, DrSci, MIREA
Yuri V. Gulyaev, DrSci, acad.RAS, IRE
Yaroslav A. Ilyushin, DrSci, MSU
Anatoly V. Kozar, DrSci, MSU
Vladimir V. Kolesov, PhD, IRE
Albina A. Kornilova, PhD, MSU
Vladimir A. Makarov, DrSci, MSU
Alexander V. Okotrub, DrSci, SB RAS
Aleksey P. Oreshko, DrSci, MSU
Igor B. Petrov, DrSci, c-m RAS, MIPT
Alexander A. Potapov, DrSci, IRE
Vyacheslav S. Rusakov, DrSci, MSU
Alexander S. Sigov, DrSci, c-m RAS, MIREA
Valentine M. Silonov, DrSci, MSU
Eugeniy S. Soldatov, PhD, MSU
Lkhamsuren Enkhtoor, DrSci (Mongolia)
Yoshiyuki Kawazoe, DrSci (Japan)
Kairat K. Kadyrzhanov, DrSci (Kazakhstan)
Peter Paul Mac Kenn, DrSci (USA)
Deleg Sangaa, DrSci (Mongolia)
Andre Skirtach, DrSci (Belgium)
Enrico Verona, DrSci (Italy)

ISSN 2414-1267

The journal on-line is registered by the Ministry of Telecom and Mass Communications of the Russian Federation. Certificate El. no. FS77-60275 on 19.12.2014

All rights reserved. No part of this publication may be reproduced in any form or by any means without permission in writing from the publisher.

©RANS 2021

EDITORIAL BOARD ADDRESS

218-219 of., 7 b., 11, Mokhovaya str.,
125009 MOSCOW, RUSSIAN FEDERATION,
TEL. +7 495 629 3368
FAX +7 495 629 3678 FOR GRACHEV

DOI: 10.17725/rensit.2021.13.003

Intensity of Electromagnetic Wave into Layers with Fluctuations of Dielectric Permittivity

Gennady I. Grigor'ev

Radiophysical Research Institute, Lobachevsky National Research State University of Nizhny Novgorod,
<http://www.nirfi.unn.ru/>

Nizhny Novgorod 603950, Russian Federation

E-mail: grig19@list.ru

Tatiana M. Zaboronkova

Lobachevsky National Research State University of Nizhny Novgorod, <http://www.unn.ru/>

Nizhny Novgorod 603950, Russian Federation

R.E. Alekseev Technical University of Nizhny Novgorod, <http://www.nntu.ru/>

Nizhny Novgorod 603950, Russian Federation

E-mail: t.zaboronkova@rambler.ru

Lev P. Kogan

Nizhny Novgorod State University of Architecture and Civil Engineering, <http://www.nngasu.ru/>

Nizhny Novgorod 603950, Russian Federation

E-mail: L_kog@list.ru

Received January 25, 2021, peer-reviewed 29 January, 2021, accepted 09 February, 2021

Abstract: The study is made of the intensity of a plane electromagnetic wave propagating into the layer with random discrete irregularities of the dielectric permittivity. The mean intensity of scattered field as a function of the parameters of random irregularities of rectangular and triangular forms is analyzed. It is shown that the deviation of the average intensity from the unperturbed value increases both the average amplitude and its standard of fluctuations. It is found that the amplitude of the intensity oscillations for a layer with irregularities of the rectangular shape is significantly greater than for fluctuations with the triangular profile.

Keywords: electromagnetic wave, scattering, random medium, fluctuations of dielectric permeability, average field intensity

UDC 538.574

Acknowledgments: The calculation method was developed within the framework of project No. 0729-2020-0057 (the basic part of the State Task of the Ministry of Science and Higher Education - Grigor'ev G.I.); numerical calculations and discussion of the results were supported by the Russian Science Foundation grant No. 20-12-00114 (Zaboronkova T.M.).

For citation: Gennady I. Grigor'ev, Tatiana M. Zaboronkova, Lev P. Kogan. Intensity of Electromagnetic Wave into Layers with Fluctuations of Dielectric Permittivity. *RENSIT*, 2021, 13(1):3-12. DOI: 10.17725/rensit.2021.13.003.

CONTENTS

- 1. INTRODUCTION (4)**
- 2. PROBLEM STATEMENT AND CALCULATION METHOD (4)**
- 3. RESULTS OF NUMERICAL CALCULATIONS AND THEIR DISCUSSION (6)**

3.1. FIELD INTENSITY IN A LAYER WITH

**RECTANGULAR DIELECTRIC CONSTANT
INHOMOGENEITIES (6)**

**3.2. FIELD INTENSITY IN A LAYER WITH
TRIANGULAR DIELECTRIC CONSTANT
INHOMOGENEITIES (8)**

- 4. CONCLUSION (10)**
- REFERENCES (11)**

1. INTRODUCTION

A considerable amount of work has been devoted to the scattering of electromagnetic waves in randomly inhomogeneous media with large-scale or delta-correlated disturbances of the medium [1–5]. The average intensity of the field of a wave incident along the normal to a layer with narrow (compared to the wavelength in vacuum) random discrete one-dimensional inhomogeneities under the condition of uniform distribution of the phase of the reflection coefficient of the wave from each inhomogeneity was analyzed in [6]. In [7], using the method of geometric optics, the mean electromagnetic field in a randomly inhomogeneous atmosphere was calculated. Taking into account the fractal properties of randomly inhomogeneous media, multiple scattering of waves was studied in [8]. The scattering of acoustic waves by a set of spherical inhomogeneities randomly located on a horizontal seabed was analyzed in [9]. Despite the large amount of research presented in these works, the properties of the mean intensity of the wave field in a medium with random rarefied fluctuations of the dielectric constant of an arbitrary shape have not been studied yet. It is possible to use these layers to model the propagation and reflection of electromagnetic waves

in the problems of sounding the Earth in shallow geophysics [10], as well as during the passage of radio emission through the troposphere (for example, [11, 12]).

In [13], the average intensity of the field of a plane wave incident on a one-dimensional layer with random rarefied rectangular dielectric permittivity inhomogeneities with zero mean amplitude is analyzed. In this paper, we generalize the results obtained in [13] to the case of a medium with rectangular permittivity perturbations with a nonzero mean value, and also consider wave propagation in a medium with triangular permittivity fluctuations. The dependence of the average intensity on the parameters of fluctuations (average width, average amplitude and standard of fluctuations in amplitude) is studied.

2. PROBLEM STATEMENT AND CALCULATION METHOD

The paper investigates the average intensity of a harmonic plane electromagnetic wave with an electric field strength $\vec{E}_0(x) = \vec{n} E_0 \exp(i\omega t - ikx)$ which falls on a layer ($0 \leq x \leq L$) with random one-dimensional inhomogeneous fluctuations of the dielectric constant of various shapes (Fig. 1). Here \vec{n} is the unit normal vector perpendicular to the

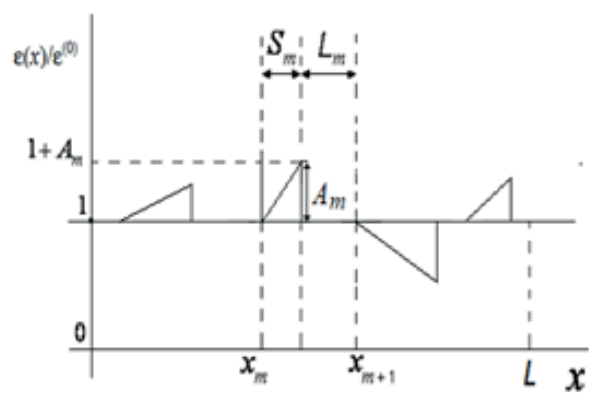
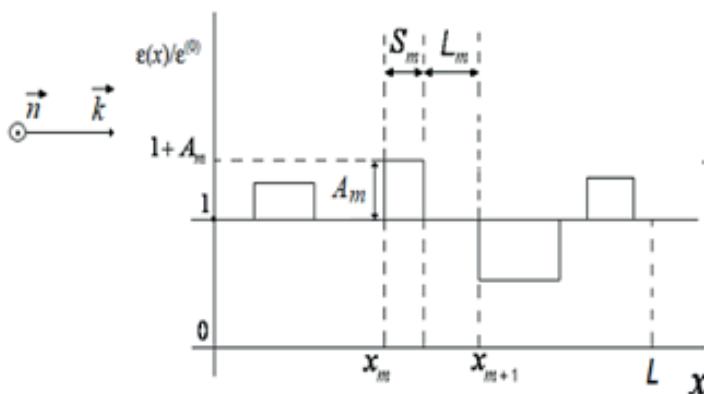


Fig. 1. The dielectric constant of the layer $\varepsilon(x)/\varepsilon^0$.

X axis, E_0 is the amplitude of the incident wave, $k = k_0 \sqrt{\epsilon^{(0)}}$, where $k_0 = 2\pi/\lambda_0$ is the wavenumber in vacuum, $\epsilon^{(0)}$ is the relative permittivity of the medium in the absence of disturbances.

The relative dielectric constant of the layer in an individual realization is given in the form

$$\epsilon(x) = \epsilon^{(0)} (1 + \sum_{m=1}^N f_m(x) [H(x - x_m) - H(x - x_m - S_m)]). \quad (1)$$

Here $H(z)$ is the Heaviside unit function, the function $f_m(x)$ determines the disturbance profile, N is the number of irregularities in the realization, x_m is the coordinate of the beginning of the m th irregularity, S_m and $|A_m| = \max |f_m(x)|$ – its width and amplitude, respectively; the distance between the inhomogeneities is $L_m = x_{(m+1)} - x_m - S_m$. We assume that x_m , S_m , and A_m are independent random variables (RVs). Parameters S_m and x_m have a truncated Gaussian distribution with average values $S = \langle S_m \rangle$ and $\langle x_m \rangle = \langle x \rangle + (m-1)\mathcal{L}$, (where $\mathcal{L} = S + \langle L_m \rangle$), as well as fluctuation standards σ_S and σ_x . We take the probability density for RV A_m in (1) in the form of a Gaussian distribution with an average value $\langle A_m \rangle = A$ and a fluctuation standard σ_A . The following restrictions are assumed to be met

$$\{\mathcal{L}, S\} \ll L, \sigma_x \ll \mathcal{L} - S, |A| + 3\sigma_A \ll 1, (k\sigma_x)^2 \gtrsim 1. \quad (2)$$

As in [13], we will assume that $\operatorname{Re}\epsilon(x) > 0$ and $\operatorname{Im}\epsilon(x) = 0$. Note that the reflection of electromagnetic waves from a randomly inhomogeneous medium with fluctuations of the complex permittivity was considered in [14] under the condition that fluctuations are delta-correlated and mutually independent.

The intensity of the field of a plane wave propagating in a layer with one-dimensional inhomogeneities, under conditions (2), is

determined by the following expression (see [13]):

$$\begin{aligned} I(x) = \pi I_0 \exp[\kappa(0.75L - x)] \times \\ \times \int_0^{+\infty} \frac{sh(\pi t)}{ch^2(\pi t)} \{2t \cos[2\kappa(L-x)t] + \\ + \sin[2\kappa(L-x)t]\} \exp(-\kappa Lt^2) dt. \end{aligned} \quad (3)$$

Here $I_0 = \frac{1}{2} E_0^2 \sqrt{\epsilon_0 \epsilon^{(0)} \mu_0^{-1}}$ is the intensity of the plane wave incident on the layer (where ϵ_0 and μ_0 are electric and magnetic constants); the parameter κ depends on the reflection coefficient R_m as follows: $\kappa = \mathcal{L}^{-1} \langle |R_m|^2 / (1 - |R_m|^2) \rangle$, the symbol $\langle \dots \rangle$ means averaging over the ensemble of realizations. Below, we proceed to calculating the coefficient κ in formula (3). To determine the value of κ , we first calculate the reflection coefficient R_m of a plane wave from a separate inhomogeneity with number m . The electric field strength E inside the m -th inhomogeneity with permittivity $\tilde{\epsilon}(\zeta) = \epsilon_0 [1 + f_m(\zeta)]$, set on the interval $0 \leq \zeta \leq S_m$ (where $\zeta = x - x_m$) is determined by the wave equation

$$E''(\zeta) + k^2 \tilde{\epsilon}(\zeta) E(\zeta) = 0, \quad (4)$$

where the prime means differentiation with respect to the argument; for $\zeta < 0$ and $\zeta > S_m$, one should set $\tilde{\epsilon}(\zeta) = \epsilon^{(0)}$. Let us denote two independent solutions of Eq. (4) as functions $\Phi_{1,2}(\zeta)$. Taking into account the conditions for the tangential components of the electromagnetic field at the boundaries of the inhomogeneity ($\zeta = 0$ and $\zeta = S_m$), we obtain the expression for the reflection coefficient R_m

$$R_m = \frac{k^2 C(S_m) - b(S_m) + ik[\alpha_1(S_m) + \alpha_2(S_m)]}{k^2 C(S_m) + b(S_m) + ik[\alpha_1(S_m) - \alpha_2(S_m)]}. \quad (5)$$

The following notations were introduced in (5):

$$\begin{aligned} b_1(S_m) &= \beta[\Phi'_2(0)\Phi'_1(S_m) - \Phi'_2(S_m)\Phi'_1(0)], \\ C(S_m) &= 1 - \beta\Phi_1(0)\Phi_2(S_m), \\ \alpha_1(S_m) &= \beta\Phi'_2(S_m)\Phi_1(0) - \Phi'_1(S_m)/\Phi_1(S_m), \\ \alpha_2(S_m) &= \beta\Phi'_1(0)\Phi_2(S_m) - \Phi'_2(0)/\Phi_2(0), \\ \beta^{-1} &= \Phi_1(S_m)\Phi_2(0). \end{aligned}$$

Below we consider the properties of the average intensity of the wave field in layers with fluctuations in the permittivity $\varepsilon(x)$ of rectangular and triangular shapes. In these cases, the solution to Eq. (4) can be obtained analytically.

3. RESULTS OF NUMERICAL CALCULATIONS AND THEIR DISCUSSION

3.1. FIELD INTENSITY IN A LAYER WITH RECTANGULAR DIELECTRIC CONSTANT INHOMOGENEITIES

The function $f_m(x)$ in relation (1) for a layer with rectangular inhomogeneities is a constant $f_m(x) = A_m$. Then the solution of equation (4) has the form: $\Phi_{1,2} = \exp(\pm ik\sqrt{1+A_m}x)$. In this case, from (5) we obtain the following expression for the reflection coefficient: $R_m = (Z_m^2 - 1)/(Z_m^2 + 1 - 2iZ_m \operatorname{ctg}\theta_m)$, where $\theta_m = k\sqrt{1+A_m}S_m$, $Z_m = (1+A_m)^{-1/2}$ is the impedance of the inhomogeneity, normalized to the impedance of the unperturbed medium $Z^{(0)} = [\mu_0/(\varepsilon_0\varepsilon^{(0)})]^{1/2}$. Note that the obtained expression for R_m coincides with the coefficient of reflection from a homogeneous plane layer given in [15]. Using the relationship between κ and the average reflection coefficient $\langle R_m \rangle$ under small values of A , for the averaged parameter κ in (3) we have:

$$\kappa = (\sigma_A^2 + A^2 - \exp(-g)[(\sigma_A^2 - k^2 S^2 \sigma_A^4 + A^2) \cos \alpha - 2kAS\sigma_A^2 \sin \alpha]) / 8L, \quad (6)$$

where $g = 2k^2\sigma_S^2 + k^2S^2\sigma_A^2/2$, $\alpha = 2k\sqrt{1+AS}$.

Below, we present the results of a numerical analysis of the dependence of the

normalized average intensity $I(S)/I_0$ on the average width of the inhomogeneities S for different values of the x coordinate inside the layer. All calculations were carried out for a layer with a thickness of $L = 2 \cdot 10^4 \lambda$, the average distance between neighboring inhomogeneities $\langle L_m \rangle = 2\lambda$, and the standard of fluctuations of the average disturbance width $\sigma_s = 0.01\lambda$.

The character of the $I(S)$ dependence is determined by the properties of the parameter κL , which is confirmed by the results of numerical calculations. **Fig. 2** shows the $\kappa(S)L$ dependence (curves 1–3) at $A = 0.05, 0, -0.05$, respectively, and the fluctuation standard $\sigma_A = 0.07$. From expression (6) it is easy to obtain that $\kappa(S)L$ is an oscillating function with a period $\lambda/(2\sqrt{1+A})$ where $\lambda = \lambda_0\sqrt{\varepsilon^{(0)}}$, which is illustrated in Fig. 2.

Fig. 3 shows the dependence of the average intensity $I(S)$ (normalized to I_0) on the dimensionless width of the inhomogeneities S/λ at the fluctuation standard $\sigma_A = 0.07$. Curves 1–5 in Fig. 3a correspond to the values $x = 0.025L, 0.5L, 0.75L, L$ and $A = 0.05$; curves 1–6 in Fig. 3b correspond to parameters $A = 0.05, 0, -0.05$ at $x = 0$ (curves 1–3) and $x = L$ (curves 4–6).

At $x < L/2$, the intensity maxima $I(S)$ are achieved at the values of the average width of

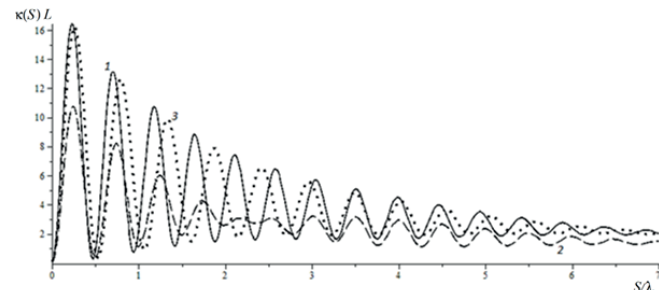


Fig. 2. Parameter $\kappa(S)L$ for a layer with rectangular inhomogeneities $\varepsilon(x)$ at $L = 2 \cdot 10^4 \lambda$, $\langle L_m \rangle = 2\lambda$, $\sigma_s = 0.01\lambda$, $\sigma_A = 0.07$. Curves 1–3 correspond to $A = 0.05, 0, -0.05$.

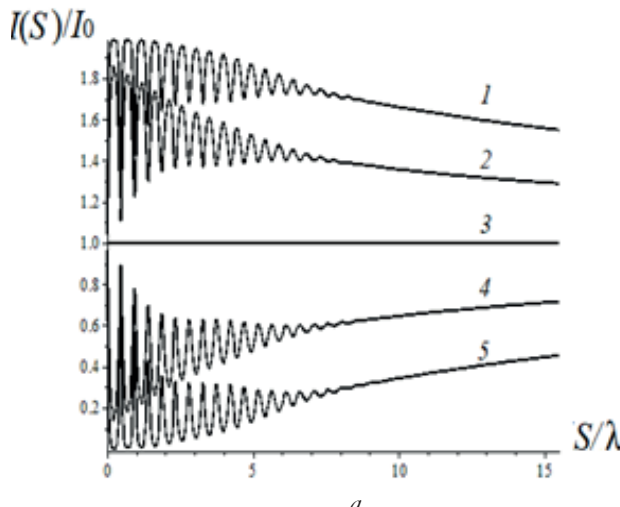
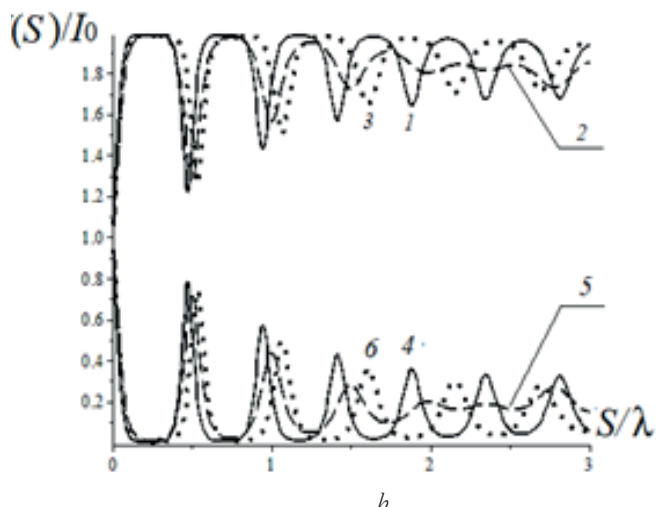


Fig. 3. Average intensity $I(S)/I_0$ for a layer with rectangular inhomogeneities $\varepsilon(x)$ at $\sigma_A = 0.07$ (a) $A = 0.05$; curves 1–5 correspond to the values $x = 0, 0.25L, 0.5L, 0.75L, L$; (b) $A = 0.05, 0, -0.05$; curves 1–3 at $x = 0$, curves 4–6 at $x = L$.

the disturbances $S_{\max} = (n + 0.5)\lambda / (2\sqrt{1+A})$, and the minima – at $S_{\min} = n\lambda / (2\sqrt{1+A})$, where $n = 0, 1, 2, 3, \dots$. For $x > L/2$, the oscillation phase of the function $I(S)$ is shifted by π in comparison with the case $x < L/2$ (curves 1 and 5, as well as curves 2 and 4 in Fig. 3a). For $x = L/2$, the ratio $I(S)/I_0 \equiv 1$ holds for all values of the average width of the inhomogeneities S . From Figures 2 and 3 and expressions (3), (6) it follows that the functions $\kappa(S)L$ and $I(S)$ have the same oscillation period. Figs. 2 and 3b show that the period of oscillations decreases with an increase in the value of A .

The amplitude of the intensity oscillations decreases with increasing S/λ . Fig. 3b shows that as the average value of the disturbance amplitude (at $\sigma_A = \text{const}$) decreases, the amplitude of the intensity fluctuations $I(S)$ decreases. With an increase in S , the intensity $I(S)$ also tends to the unperturbed value I_0 , while the coefficient $\kappa(S) \rightarrow 0$.

As follows from (6), under the condition $\sin\alpha = 0$ (which for small values of $|A| \ll 1$ is equivalent to $S = \lambda n/4$, where $n = 0, 1, 2, 3, \dots$) the value $\kappa \sim A^2$; moreover, $I(A) = I(-A)$. **Fig. 4** shows the dependence of the



parameter $\kappa(A)L$ at $\sigma_A = 0.02$ and $\sigma_A = 0.07$ (solid and dotted lines, respectively). Curves 1 and 3 correspond to the value $n = 4$, curve 2 – $n = 20$.

Fig. 5 shows the results of calculating $I(A)$ for the average width of inhomogeneities $S = \lambda$ ($n = 4$, Fig. 5a), $S = 5\lambda$ ($n = 20$, Fig. 5b) for $x = 0, 0.25L, 0.5L, 0.75L, L$ and the standard of fluctuations $\sigma_A = 0.02$ (solid curves 1–5), $\sigma_A = 0.07$ (dashed curves 1'–5'). Figs. 4 and 5 show that for integer values of

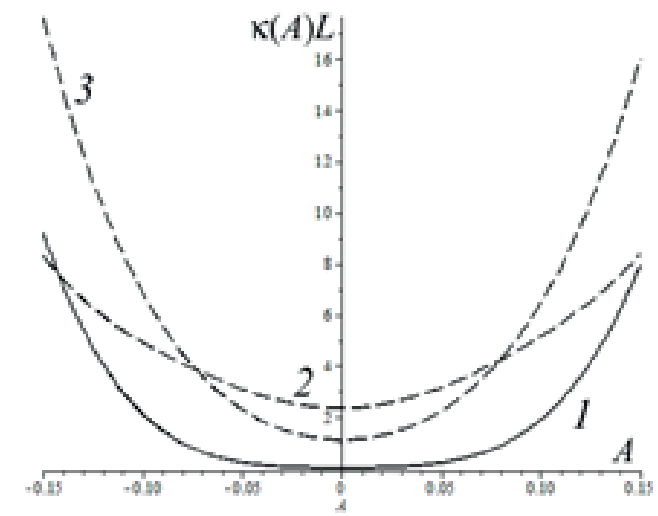


Fig. 4. Parameter $\kappa(A)L$ for a layer with rectangular inhomogeneities $\varepsilon(x)$ at $\sigma_A = 0.02$ (solid line), $\sigma_A = 0.07$ (dashed lines). Curves 1 and 3 correspond to $S = \lambda$, curve 2 – $S = 5\lambda$.

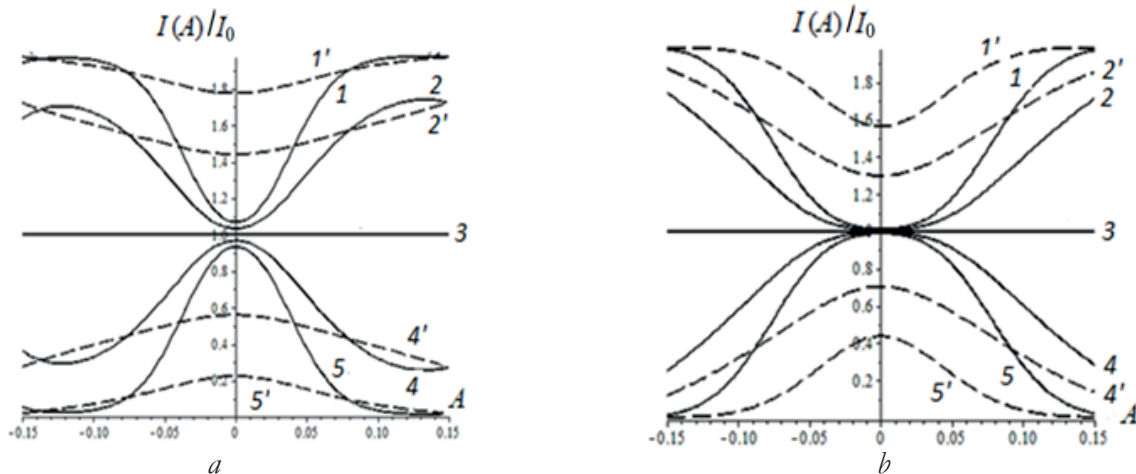


Fig. 5. Average intensity $I(A)/I_0$ for a layer with rectangular inhomogeneities $\varepsilon(x)$ at $\sigma_A = 0.02$ (solid curves), $\sigma_A = 0.07$ (dashed curves); $x = 0$ (curves 1 and 1'), $x = 0.25L$ (curves 2 and 2'), $x = 0.5L$ (curve 3), $x = 0.75L$ (curves 4 and 4'), $x = L$ (curves 5 and 5'); (a) $S = \lambda$, (b) $S = 5\lambda$.

n corresponding to the case of a symmetric dependence of the functions $\kappa(A)L$, the average field intensity is also independent of the sign of A .

Numerical calculations of the dependences $\kappa(A)L$ and $I(A)$ plotted for $S = 1.9\lambda$ and $S = 2.1\lambda$ and for the same other parameter values as in Fig. 5, confirm the conclusion about the asymmetry of the coefficient $\kappa(A)$ and intensity $I(A)$ at non-integer values of S/λ ($\sin\alpha \neq 0$).

3.2. FIELD INTENSITY IN A LAYER WITH TRIANGULAR DIELECTRIC CONSTANT INHOMOGENEITIES

For a layer with inhomogeneities of the dielectric constant in the form of right-angled triangles (Fig. 1), the functions $f_m(x)$ in (1) are written as $f_m(x) = p_m(x - x_m)$, where $p_m = A_m/S_m$. In this case, the solution to equation (4) has the form [16]:

$$\Phi_{1,2}(\zeta) = (1 + p_m \zeta)^{0.5} H_{1/3}^{(1,2)}[(2/3)kp_m^{-1}(1 + p_m \zeta)^{1.5}]. \quad (7)$$

Here $H_{1/3}^{(1,2)}(\zeta)$ are the Hankel functions of the first and second kind with index $1/3$, $\zeta = x - x_m$. In this case, the reflection coefficient R_m from one triangular inhomogeneity is determined by expression (5), in which the functions $\Phi_{1,2}(\zeta)$ are given by relation (7).

Fig. 6 shows the dependence of the parameter $\kappa(S)L$ on the normalized average width of inhomogeneities S/λ for the considered case $\varepsilon(x)$ at $\sigma_A = 0.07$ and $A = 0, 0.1, -0.1$ (curves 1–3, Fig. 6). Numerical calculations show that the $\kappa(S)L$ dependence for different values of the parameter A has a similar form as in a layer with rectangular inhomogeneities $\varepsilon(x)$ (i.e., the oscillation period decreases with increasing A).

Fig. 7 illustrates the dependence $\kappa(A)L$ at $S = 2.1\lambda$, $\sigma_A = 0.02$ and $\sigma_A = 0.07$ (curves 1 and 2); the values of the parameters L , $\langle L_m \rangle$ and σ_S are the same as in Section 3.1. It follows from the calculation results that, in the case of triangular perturbations $\varepsilon(x)$, the

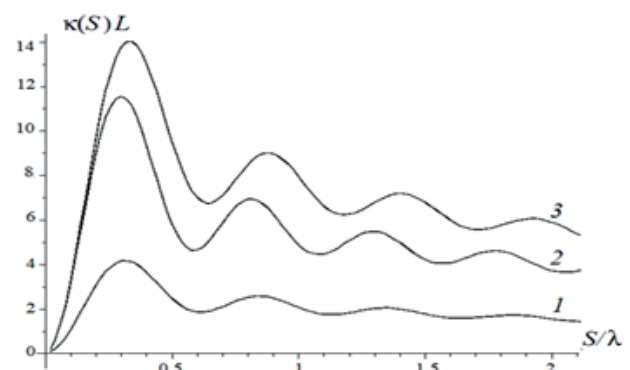


Fig. 6. Parameter $\kappa(S)L$ for a layer with triangular inhomogeneities $\varepsilon(x)$ at $\sigma_A = 0.07$; $A = 0$ (curve 1), $A = 0.1$ (curve 2), $A = -0.1$ (curve 3).

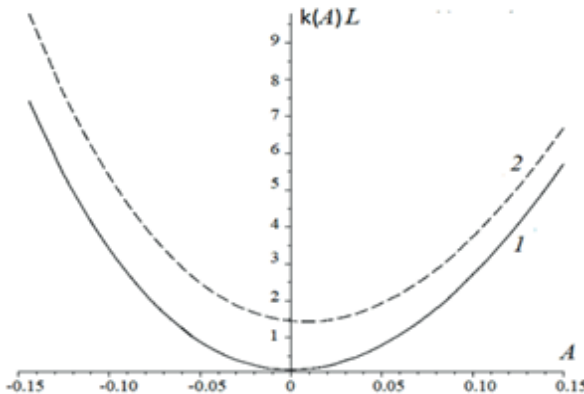


Fig. 7. Parameter $\kappa(A)L$ for a layer with triangular inhomogeneities $\varepsilon(x)$ at $S = 2.1\lambda$; $\sigma_A = 0.02$ (curve 1), $\sigma_A = 0.07$ (curve 2).

function $\kappa(A)L$ depends on the sign of A for any values of the normalized average width of the inhomogeneities S/λ .

Fig. 8 shows the average intensity $I(S)/I_0$; in Fig. 8a, curves 1–5 corresponding to $x = 0, 0.25L, 0.5L, 0.75L, L$ correspond to the values of $\sigma_A = 0.07, A = 0.1$; curves 1–6 in Fig. 8b correspond to $\sigma_A = 0.07, A = 0; 0.1; -0.1$ at $x = 0$ (curves 1–3) and $x = L$ (curves 4–6). Comparing Fig. 8 and Fig. 3, we come to the conclusion that the periods of oscillations of the function $I(S)$ for fluctuations $\varepsilon(x)$ of triangular and rectangular shapes practically

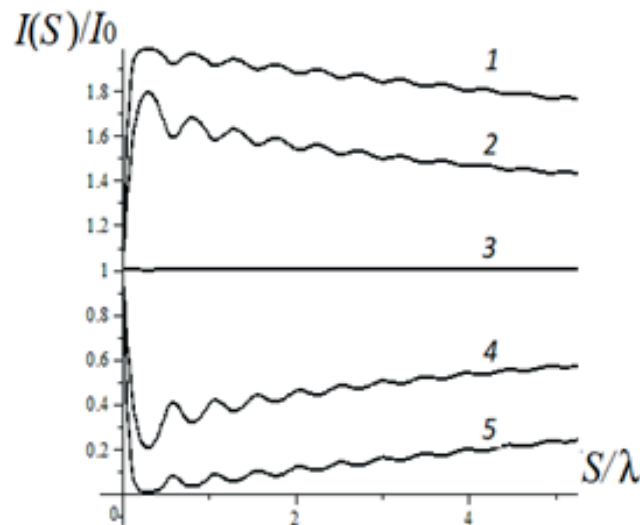


Fig. 8. Average intensity $I(S)/I_0$ for the layer with triangular inhomogeneities $\varepsilon(x)$ at $\sigma_A = 0.07$ (a) $A = 0.1$, curves 1–5 correspond to $x = 0, 0.25L, 0.5L, 0.75L, L$; (b) $A = 0, 0.1, -0.1$; $x = 0$ (curves 1–3), $x = L$ (curves 4–6).

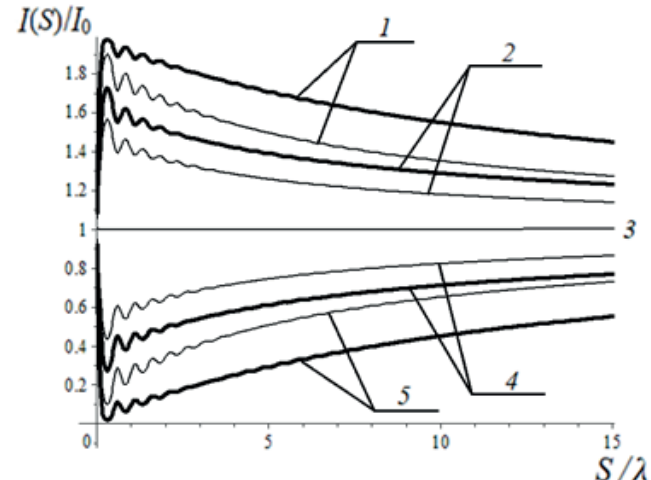
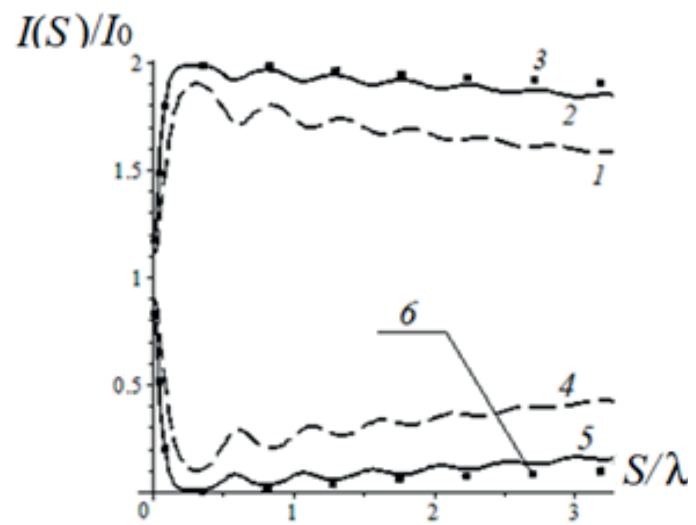


Fig. 9. Average intensity $I(S)/I_0$ for a layer with triangular inhomogeneities $\varepsilon(x)$ at $\sigma_A = 0.07, A = 0$ (thin lines), $A = 0.1$ (bold lines); curves 1–5 correspond to $x = 0, 0.25L, 0.5L, 0.75L, L$.

coincide, while the amplitude of oscillations for triangular inhomogeneities turns out to be significantly smaller (Figs. 4 and 7).

Fig. 9 shows the normalized average intensity $I(S)/I_0$ for a layer with triangular inhomogeneities $\varepsilon(x)$ at $x = 0, 0.25L, 0.5L, 0.75L, L$ (curves 1–5). The curves in the figure correspond to the $I(S)/I_0$ dependence at $\sigma_A = 0.07, A = 0$ (thin lines), and $A = 0.1$ (bold lines). It should be noted that the difference between the intensities $|I(S) - I_0|$ increases with increasing $|A|$ and σ_A .



Thus, it is shown that for a layer with triangular inhomogeneities $\varepsilon(x)$, the intensity $I(\mathcal{A})$ depends on the sign of \mathcal{A} for any values of the average width of inhomogeneities, in contrast to the case of dielectric constant with rectangular inhomogeneities. This is explained by the fact that the reflection coefficient from a single inhomogeneity with a linear dependence $\varepsilon(x)$ is a function of the parameter \mathcal{A} , in contrast to the case of constant $\varepsilon(x)$ inside the inhomogeneity. Note that despite of the asymmetric shape of the inhomogeneities $\varepsilon(x)$ of a triangular shape, the layer with inhomogeneities of this shape, as well as the layer with rectangular fluctuations $\varepsilon(x)$, does not possess anisotropy properties, i.e. the distribution of the average intensity inside the layer with one-dimensional discrete fluctuations $\varepsilon(x)$ does not depend on the direction of incidence of the wave on the layer. This is due to the multiple reflection of the wave from a large number of random irregularities within the layer.

4. CONCLUSION

The problem of scattering of a plane electromagnetic wave by a dielectric layer with one-dimensional random discrete inhomogeneities of arbitrary width is considered. When calculating the intensity of the scattered field, it was assumed that the coordinates of the points of origin of inhomogeneities, as well as their width and amplitude, are independent random variables distributed over Gaussian. The cases of layers with perturbations of the permittivity of rectangular and triangular shapes are investigated. One of the results of this work is the lack of localization of mean intensity. The localization of plane waves in chaotically layered media are discussed in [17-21]. In particular, it was shown in [17] that dynamic localization takes place for individual realizations of the

field, while statistical energy localization expresses the properties of the entire statistical ensemble of realizations. The main conclusion of the authors of [17] is that, despite the presence of field localization in individual realizations, it may be absent for the average wave intensity for the entire statistical ensemble of realizations. The calculation method used in our work is based on averaging the field intensity over all random realizations.

It is shown in this work that the amplitude of intensity oscillations $I(S)$ for a layer with rectangular inhomogeneities $\varepsilon(x)$ is significantly larger than for fluctuations with a triangular profile. With an increase in the average width of inhomogeneities, the amplitude of oscillations of the average intensity at a nonzero average value of the amplitude of fluctuations decreases faster than at $\mathcal{A} = 0$. The period of oscillations for both types of disturbances is the same and is approximately equal. The deviation of the average intensity $I(S)$ from the unperturbed value turns out to be proportional to the amplitude $|\mathcal{A}|$ and the standard of fluctuations $\sigma_{\mathcal{A}}$ of inhomogeneities and decreases with an increase in the average width S . Differences in the behavior of the average intensity when the wave is scattered by layers with inhomogeneities of the dielectric constant with a constant and linear dependence on the x coordinate inside the inhomogeneities are explained by the features of the reflection coefficients of the wave from individual fluctuations of rectangular and triangular shapes [12]. For a layer with rectangular inhomogeneities, the $I(\mathcal{A})$ dependence is a symmetric function of the average value of the parameter \mathcal{A} at integer values of S/λ for small fluctuation amplitudes. For a layer with fluctuations

in the permittivity of a triangular shape, the dependences $\kappa(A)$ and $I(A)$ are not symmetric functions of A at any width of the inhomogeneities, as well as the modulus of the reflection coefficient from an individual inhomogeneity. The noted fact can be used in the diagnostics of natural environments.

REFERENCES

1. Klyatskin VI. Propagation of electromagnetic waves in a randomly inhomogeneous medium as a problem of statistical mathematical physics. *UFN*, 2004, 174 (2):177-195.
2. Klyatskin VI. *Stochastic equations. Theory and its applications to acoustics, hydrodynamics and radiophysics. Vol. 1.* Moscow, Fizmatlit, 2008, 320 p.
3. Abramovich BS, Gurbatov SN, Ryzhov YA. Multiple scattering of waves in a one-dimensional randomly inhomogeneous medium. *Izv. VUZov. Radiofizika*, 1979, 22 (5):566-576.
4. Zaboronkova TM, Kogan LP, Tamoikin VV. Propagation of electromagnetic waves in a half-space with one-dimensional stochastically inhomogeneous disturbances of the height and impedance of the boundary. *RE*, 2005, 50(5):552-563.
5. Novikov FV, Akulinichev YP. Comparative assessment of the influence of tropospheric inhomogeneities and irregularities of the earth's surface on the characteristics of the electromagnetic field. *TUSUR Reports*, 2011, 1(23):60-64.
6. Gazaryan YL. On the one-dimensional problem of wave propagation in a medium with random inhomogeneities. *JETF*, 1969, 56(6):1856-1871.
7. Zakharov FN, Akulinichev YP. Calculation of the level of the average electromagnetic field by a numerical method in a randomly inhomogeneous atmosphere. *TUSUR Reports*, 2015, 2(36):10-18.
8. Potapov AA. Multiple scattering of waves in fractal randomly inhomogeneous media from the point of view of radar of self-similar multiple group targets. *RENSIT*, 2018, 10(1):3-22. DOI: 10.17725/rensit.2018.10.003.
9. Gurbatov SN, Gryaznova IU, Ivaschenko EN. Investigation of backscattering of acoustic waves by discrete inhomogeneities of different sizes. *Acoustic Journal*, 2016, 62(2):203-207.
10. Manshtein AK. *Shallow geophysics.* Novosibirsk, Institute of Geophysics SB RAS Publ., 1997, 136 p.
11. Tatarsky VI. Wave propagation in a turbulent atmosphere. Moscow, Nauka Publ., 1967, 548 p.
12. Semenov AA, Arsenyan TI. Fluctuations of electromagnetic waves on surface paths. Moscow, Nauka Publ., 1978, 272 p.
13. Grigoriev GI, Zaboronkova TM, Kogan LP. Scattering of electromagnetic fields on a layer with one-dimensional rectangular inhomogeneities. *RE*, 2017, 62(10):945-952.
14. Krainyukov IA, Zernov NI. On the reflection of electromagnetic waves from a randomly inhomogeneous medium with fluctuations in the complex dielectric constant. *RE*, 2013, 58(6):578-582.
15. Brekhovskikh LM. *Waves in layered media.* Moscow, Publishing house of the Academy of Sciences of the USSR, 1957, 343 p.
16. Kamke E. *Handbook of ordinary differential*

- equations. 4th edition.* Moscow, Nauka Publ., 1971, 576 p.
17. Klyatskin VI. *Essays on the dynamics of stochastic systems.* Moscow, URSS Publ., 2012, 442 p.
18. Vinogradov AP, Merzlikin AM. Band gap theory of localization in one-dimensional system. *Phys. Rev. E*, 2004, 70(2Pt2): 026610-1-026610-4.
19. Blioch UP. Random resonators. *Izv. universities. Applied Nonlinear Dynamics*, 2012, 20(4):85-97.
20. Bliokh YP, Chaikina EI, Lizarraya N, Freilikher V, Mendes E, and Nori F. Disorder-induced cavities, resonances, and lasing in randomly-layered media. *Phys. Rev.B*, 2012, 86(8):054204-054208.
21. Shadrivov IV, Bliokh K, Bliokh YP, and Freilikher V. Bistability of Anderson localized states in nonlinear random media. *Phys. Rev. Letters*, 2010, 104(12):123902 (4).

DOI: 10.17725/rensit.2021.13.013

Thermal deformation model of the submodule of the X-band output power amplifier

Alexander M. Hodakov, Ruslan G. Tarasov, Vyacheslav A. Sergeev, Alexander A. Kulikov

Kotelnikov Institute of Radioelectronics and Electronics of RAS, Ulyanovsk Branch, <http://www.ulireran.ru/>

Ulyanovsk 432071, Russian Federation

E-mail: ln23al@yandex.ru, zavod@npp-iskra.ru, sva@ulstu.ru, kulikova36@yandex.ru

Received February 18, 2021, peer-reviewed 26 February, 2021, accepted 09 March, 2021

Abstract. The results of 3D modeling in the Comsol Multiphysics software environment and calculation of temperature and thermal deformation fields of GaAs crystals of monolithic integrated circuits (MIC) of microwave amplifiers as part of the submodule of the X-band output power amplifier (OPA) and their contact connections with the substrate in pulse modes of operation with different duty cycles are presented. It is shown that the maximum temperature and thermomechanical stresses in the MIC crystal in the dynamic mode of operation significantly exceed the calculated values for the stationary mode and strongly depend on the pulse duty cycle of the power dissipated by the MIS. Thermomechanical stresses take the maximum value in some narrow region near the boundary of the adhesive connection of the MIC crystal with the mounting plate; this maximum value strongly depends on the temperature coefficient of expansion (TCE) of the adhesive and takes the lowest value when the TCE of the adhesive is equal to the TCE of the GaAs crystal.

Keywords: thermal deformation, a microwave amplifier, the duty cycle of the pulse

UDC 621.382.029

Acknowledgments: The work was carried out within the framework of the state task and was supported by the Russian Foundation for Basic Research and Government of Ulyanovsk region (RFBR project No. 18-47-730024).

For citation: Alexander M. Khodakov, Ruslan G. Tarasov, Vyacheslav A. Sergeev, Alexander A. Kulikov. Thermal deformation model of the submodule of the X-band output power amplifier. *RENSIT*, 2021, 13(1):13-18. DOI: 10.17725/rensit.2021.13.013.

CONTENTS

1. INTRODUCTION (13)

2. THERMODEFORMATIONAL MODEL OF THE OUTPUT POWER AMPLIFIER SUBMODULE (14)

3. CONCLUSION (17)

REFERENCES (17)

1. INTRODUCTION

The main element base of modern submodules of output power amplifiers

(OPAs) of receiving and transmitting modules of active phased phased array antennas are solid-state monolithic integrated circuits of microwave power amplifiers on GaAs or GaN crystals [1,2]. To obtain the required output power in the OPA, the summation of the microwave power of two or more MICs is usually used. The efficiency of modern OPA, as a rule, does not exceed 20-25%, and the power released in the MIC leads to their significant heating. The inhomogeneous

heating of the MIC and the difference in the temperature coefficients of the material of the contact joint and the MIC crystal lead to large thermomechanical stresses in the area of the contact joint of the MIC with the substrate. The efforts of the developers are aimed at reducing the overheating of the MIC during operation, but reducing the average temperature of the substrate does not eliminate the problem of local dynamic overheating of the MIC in pulse modes of operation. Thermal models and thermal modes of operation of the OPA X-band were considered in many works [3-5]. However, estimates of the thermomechanical stresses occurring in MIC crystals and in the region of their contact connections with a substrate in pulsed operating modes have not been given in the literature. At the same time, these thermal deformations are one of the main reasons for the increase in the thermal resistance of the contact joint as a result of the accumulation of microcracks [6] and gradual (degradation) failures of the OPA.

2. THERMODEFORMATIONAL MODEL OF THE OPA SUBMODULE

The object of research in this paper is the submodule of the X-range OPA, the thermal model of which is considered by us in [7]. With a OPA efficiency of 20%, the pulse power dissipated by the OPA MIC is 60 W, and the average for the period of radio pulses is 12 W. With an uniform distribution of power between the MIC, each MIC dissipates 6 W of average power. The power dissipated by other OPA elements can be neglected.

The geometry of the OPA thermal model is presented in **Fig. 1** in the

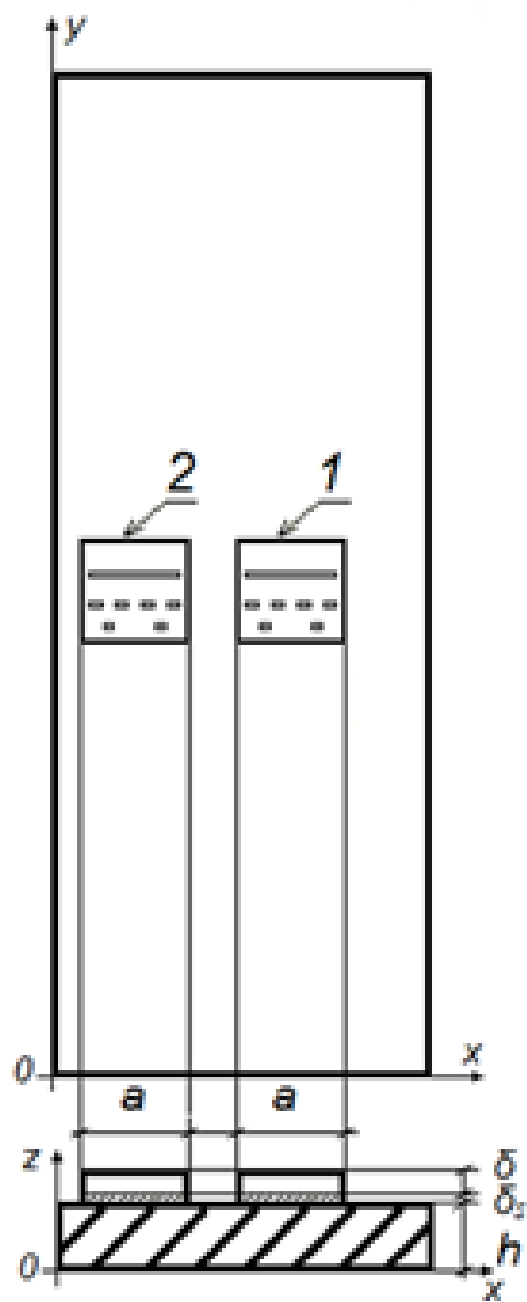


Fig. 1. Geometry of the OPA model: 1, 2 - MIC with the location of heat sources on the crystal surface.

form of two identical rectangular GaAs MIC crystals with sides of size $b \times a$ and thickness δ , fixed on a copper heat sink plate of thickness h using an adhesive layer of thickness δ_s and with a thermal conductivity coefficient λ ; the dimensions of the MIC crystal $b \times a \times \delta = 4.29 \times 4.94 \times 0.1$ mm; the dimensions of the mounting plate $17 \times 46 \times 5.5$ mm. To calculate and analyze

the thermodeformational processes in the OPA submodule, the equation of thermoelasticity was added to the non-stationary heat equation in its mathematical thermal model [8]:

$$\mu_i \nabla^2 \vec{u}_i + (\lambda_i + \mu_i) \nabla (\nabla \vec{u}_i) - (3\lambda_i + 2\mu_i) \alpha_i \nabla (T_i - T_0) = 0, \quad i=1,\dots,5 \quad (1)$$

where $\vec{u}_i(x, y, z, t)$ is the deformation displacement of the elements of the structure OPA; T_0 is the ambient temperature; $\lambda_i = \frac{v_i E_i}{(1+v_i)(1-2v_i)}$, $\mu_i = \frac{E_i}{2(1+v_i)}$ - Lame coefficients; E_i , v_i , α_i - modulus of elasticity, Poisson's ratio and coefficient of thermal expansion of the materials of the structure $\nabla = \nabla(x, y, z)$. All external surfaces of the elements of the OPA structure are considered free.

The numerical solution of the model problem was performed by the finite element method using the COMSOL

Multiphysics software environment. The values of the mechanical characteristics of GaAs and copper were taken from the Comsol Multiphysics library. For the basic design version, silver-containing epoxy adhesive XH9960-1 from NAMICS was chosen as the adhesive, thickness $\delta_s = 15$ microns with a temperature coefficient of expansion (TCE) $\alpha = 29e-6 \cdot K^{-1}$ and other mechanical and thermophysical characteristics that were found from the technical specification of the adhesive [9]. The critical temperature of the GaAs crystal is $T_c = 460$ K. The ultimate shear strength of the crystal for this type of glue $\sigma_c = 13$ MPa.

As shown by the calculated studies, the maximum value of the mechanical stress in the structure is concentrated in a small critical area at the edge of the adhesive joint of the MIC crystal with the mounting plate (**Fig. 2**).

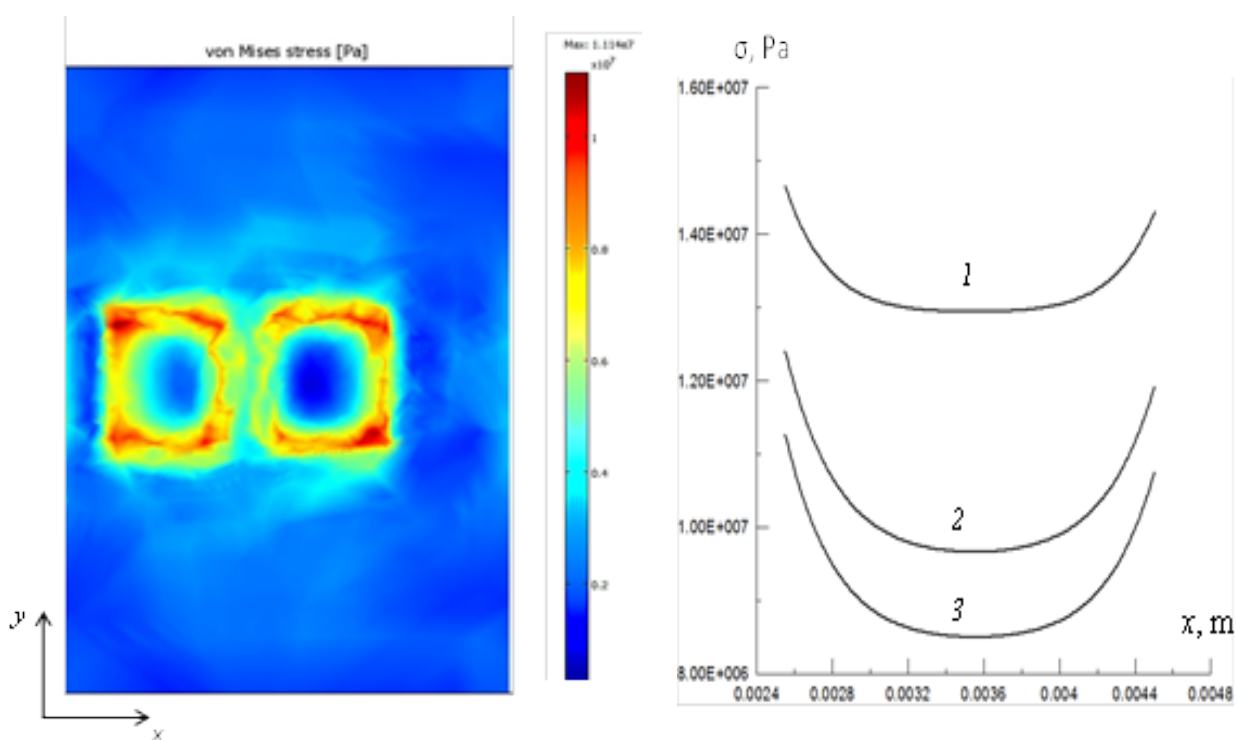


Fig. 2. Distribution of mechanical stress in the area of the glued joint; a: 1 - $3e-6 \cdot K^{-1}$, 2 - $29e-6 \cdot K^{-1}$, 3 - $9e-6 \cdot K^{-1}$; $W = 6$ W.

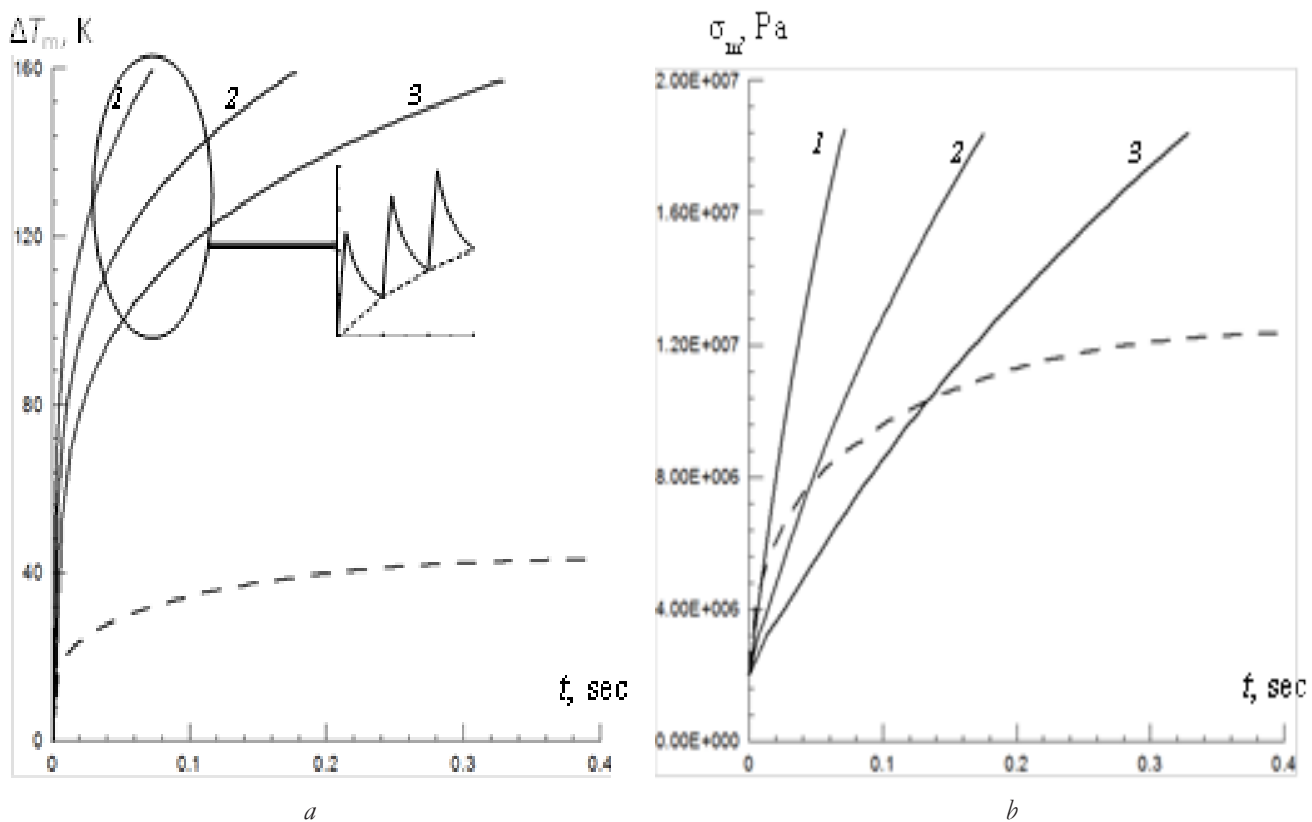


Fig. 3. Kinetics of the overheating temperature of the center of the upper surface of the MIC crystal (a) and the maximum mechanical stress of the adhesive joint (b); pulse duration $\tau = 10 \mu\text{s}$; duty cycle Q : 1 - 2, 2 - 5, 3 - 10; $T_c = 460 \text{ K}$.

Time dependence of the temperature of the center of the upper surface of the crystal MIC and the maximum stress in the critical region at the edge of the adhesive bonding of the crystal with a mounting plate, as shown in **Fig. 3**. The dashed line corresponds to the temperature behavior during dissipating in each of MIC 6 W average power during the period, and the solid lines - 30 W of pulsed power, with a pulse duration $\tau = 10 \mu\text{s}$ and duty cycle of Q varying in the range $Q = 2 \div 10$. The maximum temperature and mechanical stress in the dynamic mode (at $Q \sim 10$) reach the limit values in just tenths of a second.

Calculations of the maximum thermomechanical stress acting in the critical region at the edge of the adhesive joint for several brands of electrically

conductive adhesives used for mounting

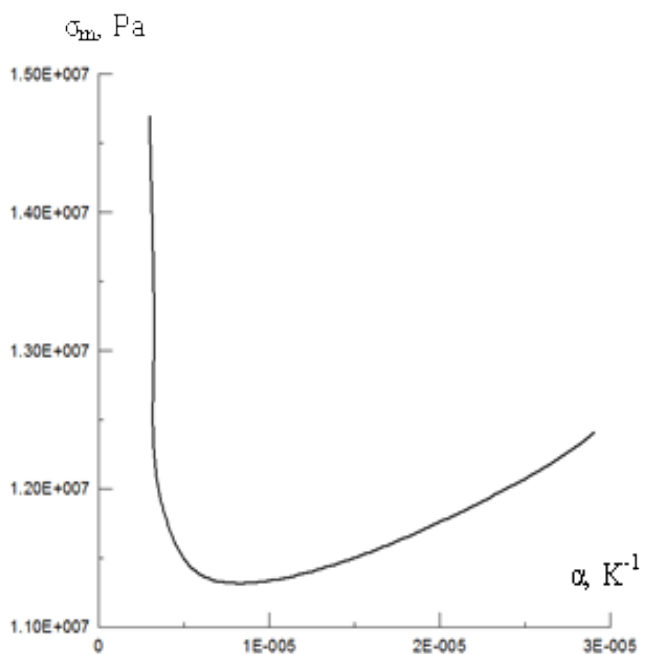


Fig. 4. Dependence of the maximum mechanical stress on the thermal expansion coefficient at $W = 6 \text{ W}$.

crystals [9-11], with a TCE varying within $\alpha = (3 \div 30) \text{e-}6 \cdot \text{K}^{-1}$, showed that the calculated curve has a minimum when the TCE of the glue and the GaAs crystal are equal (**Fig. 4**).

Even with a small decrease in the TCE of the adhesive compared to the GaAs TCE, the maximum stress in the critical area of the contact joint increases sharply, which must be taken into account when choosing the material of the contact joint.

3. CONCLUSION

Modeling of thermal and thermal processes in the submodule OPA showed that the maximum temperature and thermomechanical stresses in the crystal MIC and in contact with the substrate coupling in dynamic mode substantially exceed the calculated values for the stationary regime and highly dependent on the duty cycle of MIC dissipated power. The maximum values of the thermomechanical stresses in the area solder joints crystal MIC with a mounting plate are accepted in some narrow region near the boundary of the crystal dimension. The maximum mechanical stress σ_m strongly depends on the TCE of the glue and takes the lowest value when the TCE of the glue and the GaAs crystal are equal.

REFERENCES

1. Vikulov I. Monolithic Microwave ICs the Technology Basis of AESA. *Electronics: Science, Technology, Business Journal*, 2012, 7:60-73.
2. Krasnikov GIa, Volosov AV, Kotliarov EI. X-Band Transmit/Receive Module. *Electronics. Series 3. Microelectronics*, 2016, 3:23-29.
3. Kolomeytsev VA, Ezopov AV, Semenov AE. Thermal state of output power amplifier of receiving and transmitting module of active phased antenna array. *Antennas*, 2012, 8(183):15-19.
4. Sergeev VA, Tarasov RG, Kulikov AA. Diagnostics of the quality of output power amplifiers of AFAR transceiver modules by temperature fields. *Automation of management processes*, 2019, 1:112-117.
5. Sergeev VA, Tarasov RG. Quality control of submodules of X-band output power amplifiers by transient thermal characteristics. *Automation of management processes*, 2020, 2:124-129.
6. Parfenov AN. Introduction to the theory of strength of brazed joints. *Technologies in the Electronics Industry*, 2008, 2:46-52.
7. Sergeev VA, Tarasov RG, Khodakov AM. Calculation and measurement of thermal parameters of monolithic integrated circuits of microwave amplifiers as part of X-band output power amplifiers. *Radio electronics journal* [electronic journal], 2019, 8. Access mode: <http://jre.cplire.ru/jre/sep19/1/text.pdf>. DOI 10.30898/1684-1719.2019.8.12.
8. Pain B, Weiner J. *Theory of temperature stresses*. Moscow, Mir Publ., 1964, 520 p.
9. XH9960-1 silver epoxy adhesive [electronic resource] <https://namics.co.jp>.
10. Electrically conductive adhesives [electronic resource] <https://ostec-materials.ru/materials/>

dlya - proizvodstva - mi / klei-
elektroprovodyashchie.php.

11. Isaev AYu, Petrova AP, Lukina NF.
Conductive adhesives with different
fillers. Sat. *Proceedings of Vseros. Conf. on
fundamental and applied research in the field
of creating adhesives, adhesive binders and
adhesive prepregs.* Moscow, 2018, FSUE
"VIAM" Publ., p. 14-29.

DOI: 10.17725/rensit.2021.13.019

Analysis of the probabilistic characteristics of the electrical parameters of a broadband balanced mixer of microwave radio signals based on resonant tunneling diodes and an assessment of its reliability

Kirill V. Cherkasov, Sergey A. Meshkov, Vasiliy D. Shashurin

Bauman Moscow State Technical University, <http://bmstu.ru/>

Moscow 105005, Russian Federation

E-mail: kvcbe@mail.ru, sb67241@mail.ru, schashurin@bmstu.ru

Ivan A. Romanov

A.I. Berg Central Research Institute of Radioelectronics, <http://cnirti.ru/>

Moscow 107078, Russian Federation

E-mail: musicfox@yandex.ru

Received October 13, 2020, peer-reviewed 29 October, 2020, accepted 09 November, 2020

Abstract: The object of research is the broadband balanced SHF mixer (BM) based on resonant-tunneling diodes (RTDs). The research goals are to perform the statistical analysis of BMs design parameters technological errors impact on its electrical characteristics scatter, and to analyze the kinetics of these characteristics under the destabilizing factors influence. The ranging of BMs design parameters technological errors impacts on its electrical characteristics scatter revealed that the biggest impact is made by the technological errors of the BMs non-linear elements I-V characteristics. The BMs reliability study revealed that to ensure the studied BMs reliability during operation under high temperatures impact the design and technological optimization of the BMs electrical characteristics is required.

Keywords: resonant tunneling diode, nonlinear frequency converters of radio signals, reliability, computer statistical experiment

Acknowledgments: The reported study was funded by RFBR, project number 19-37-90125/19.

For citation: Kirill V. Cherkasov, Ivan A. Romanov, Sergey A. Meshkov, Vasily D. Shashurin. Analysis of the probabilistic characteristics of the electrical parameters of a broadband balanced mixer of microwave radio signals based on resonant tunneling diodes and an assessment of its reliability. *RENSIT*, 2021, 13(1):19-26. DOI: [10.17725/rensit.2021.13.019](https://doi.org/10.17725/rensit.2021.13.019).

CONTENTS

1. INTRODUCTION (19)
2. RESEARCH OBJECT'S DESCRIPTION (21)
3. STUDY OF THE RTD-BASED BMs DESIGN PARAMETERS TECHNOLOGICAL ERRORS IMPACT ON ITS ELECTRICAL PARAMETERS DISTRIBUTION (21)
4. STUDY OF THE RTD BM's ELECTRICAL PARAMETERS' KINETICS DURING OPERATION (23)
5. CONCLUSION (25)
- REFERENCES (25)

1. INTRODUCTION

Nonlinear frequency converters (FC) are radiotechnical systems key elements since they are used to perform general radiotechnical conversions. FCs electrical parameters determine the electrical parameters of most radiotechnical systems. One of the ways to improve FCs electrical parameters is to use nanoelectronic devices, such as resonant-tunneling diodes (RTD) based on AlGaAs/GaAs multilayer heterostructures with transverse current transport [4]. The improvement of the FCs electrical parameters

is achieved by picking the optimal shape of the diodes current-voltage characteristic (I-V characteristic). The optimal shape of diodes I-V characteristic is obtained by varying thicknesses and chemical composition of the resonant-tunneling structures (RTS) layers [14,15]. The RTD usage allows to widen the operating frequencies range up to THz [1-3,6,10,13,16] and increase the FCs noise immunity. The RTD can be manufactured using proven microelectronics technologies.

During FCs design stage, the task of ensuring its reliability in given operating conditions is a priority one along with the task of ensuring the devices electrical parameters. To solve the former task the reliability assessment of the device being developed is required. As the reliability assessment by experimental means is costly, it seems topical to study the kinetics of RTD-based FCs electrical parameters under destabilizing factors impact considering the effect of its design parameters technological errors on its electrical parameters distributions and to assess the devices reliability for gradual failures by the means of computer statistical experiment. The FCs gradual failure is caused by the gradual deterioration of its electrical parameters. This deterioration is caused by the irreversible degradation of the RTDs I-V characteristic under destabilizing factors impact.

One of the possible ways to solve the task of ensuring the FCs reliability in given operating conditions is the micro- and nanodevices design methodology listed in [5]. This methodology proposes to introduce the design and technological optimization stage, which allows to determine the corrections of the devices design parameters and electrical characteristics, leaving the technological tolerances on its design parameters and designer-determined tolerances on the device's electrical parameters intact. The gamma-percentage time to failure is used as the goal function. The described approach supposes the usage of the imitational (including

probabilistic) modeling of the devices electrical parameters to determine their degradation patterns in given operating conditions, considering the technological errors and is based on the research results of the devices elements electrical parameters degradation processes in given operating conditions.

Based on the above, to solve the problem of ensuring the reliability of the frequency converter of radio signals, it seems most expedient to use a software package that allows analyzing the reliability of the frequency converter by calculation methods and perform the design and technological optimization of the RTD-based FCs electrical parameters to ensure the required reliability indicators in given operating conditions. Having such a software complex would allow to improve RTD-based FCs reliability and quality as well as improve their manufacturing efficiency. To improve optimization algorithms efficiency and speed it seems appropriate to determine the FCs design parameters making the main contribution to its electrical parameters' distribution. Thus, it seems relevant to solve the problem of determining the FCs design parameters, technological errors of which make the maximal contribution to the FCs electrical parameters distribution.

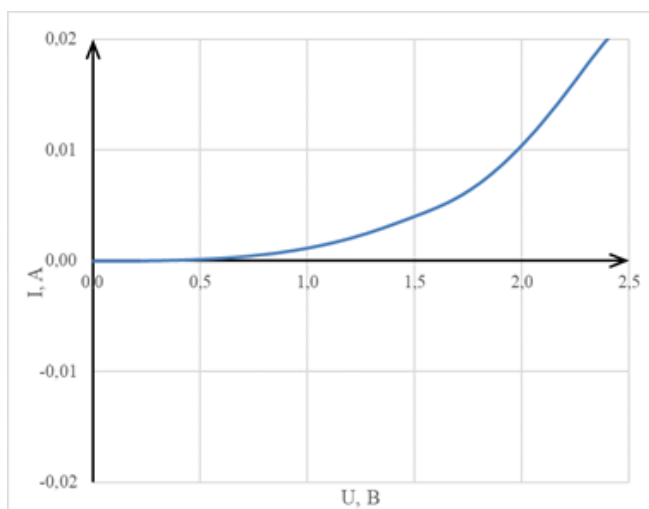


Fig. 1. The initial section of the RTDs I-V characteristic

2. RESEARCH OBJECTS DESCRIPTION

In this paper the RTD-based broadband balanced microwave frequency mixer (RTD BM) of 4-8 GHz range is being studied. The initial section of the RTDs I-V characteristic is shown in **Fig. 1**. The simulation of the BMs electrical parameters is performed in the AWR Microwave Office CAD.

3. STUDY OF THE RTD-BASED BMS DESIGN PARAMETERS TECHNOLOGICAL ERRORS IMPACT ON ITS ELECTRICAL PARAMETERS DISTRIBUTION

The conversion losses of the output signals spectrum components (OSSC) 1-1 and 2-2 are considered as the RTD BMs electrical parameters (**Fig. 2**). The first index in the OSSCs number designates the n -th harmonic of the signal, the second one – m -th harmonic of the heterodyne, which form the OSSC $n\cdot m$: $n\cdot f_s \pm m\cdot f_b$. Signals frequency is f_s , heterodynes f_b .

The RTD BM's design parameters are separated into 3 groups: nonlinear elements (NE) I-V characteristic, BMs topology parameters and substrates parameters. All parameters distributions obey the Gauss law. NEs I-V characteristics distribution is caused by the combined impact of the NEs design parameters technological errors: RTS and near-contact areas thicknesses and chemical compositions, mesas and ohmic contacts areas. Microstrip transmission lines widths and lengths are considered as the

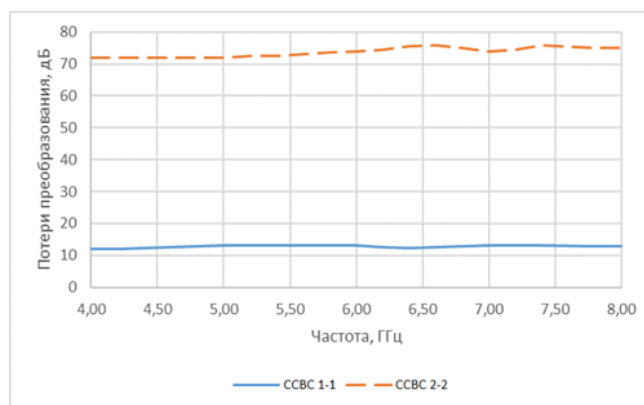


Fig. 2. Nominal values of the OSSC 1-1 and 2-2 conversion losses of the studied RTD BM.

Table 1.
RTD design parameters maximum deviations values

Parameter	Maximum deviation
Thickness of spacers, well and barriers	± 1 monolayer
Al doping level in barriers and spacers	$\pm 1\%$
Ohmic contacts' contact resistivity	$\pm 0.25 \mu\text{Ohm}\cdot\text{sm}^2$ (nominal value – $1 \mu\text{Ohm}\cdot\text{sm}^2$)
Mesa diameter	$\pm 2 \mu\text{m}$ (nominal value $20 \mu\text{m}$)

BMs topology parameters. Tolerances on these parameters is $\pm 12 \mu\text{m}$. Substrate parameters are its thickness and relative permittivity. The substrate is considered to be made of polycor, its relative permittivity is $9.8 \pm 0.1 \text{ F/m}$, thickness – $1 \pm 0.03 \text{ mm}$. Since modern microelectronics CADs dont have RTD models allowing to calculate the diodes I-V characteristic basing on RTDs design parameters, special software complex was developed by the authors. This complex allows to simulate the initial section of the RTDs I-V characteristic, simulate its kinetics in given operating conditions and carry out the computer statistical experiment studying the impact of the RTDs design parameterstecnological errors on the I-V characteristics distribution [15]. To carry out the study, a bunch of 100 diodes was modelled (RTDs design parameters maximal deviations listed in **Table 1**, current distribution in the operating point (1.36 V) – on **Fig. 3**).

To assess the impact of RTD BMs design parameters technological errors on its electrical parameters distribution several batches of RTD BMs were modelled, per 100 devices each. In the first one only RTDs design parameters were

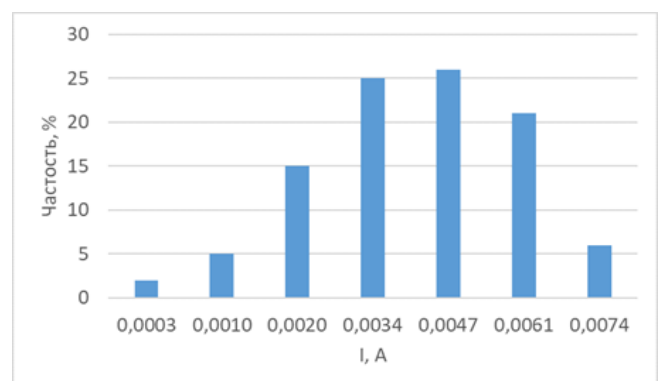


Fig. 3. RTD I-V characteristics current distribution in the operating point.

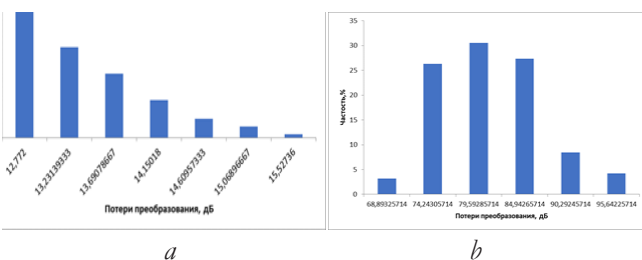


Fig. 4. Simulated distributions of OSSC 1-1 (a) and 2-2 (b) conversion losses at the signal frequency 7.5 GHz under the combined impact of technological errors of NEs I-V characteristics, microstrip lines sizes, and substrates thickness and relative permittivity.

varied while other parameter groups were set constant and equal to their nominal values. In the second batch microstrip lines lengths and widths were varied, in the third one – substrates thickness, in the fourth – substrates relative permittivity. Finally, the fifth batch was modelled using combined impact of all listed parameters technological errors.

Simulated distributions of the BMs electrical parameters for the combined impact of all design parameters technological errors case are shown on the Fig. 4a,b, distributions parameters are listed in Table 2. Dispersions of the BMs electrical parameters under the separate impact of various BMs design parameters groups can be assessed basing on the Table 2 and contributions of said parameters groups in the total dispersion (Fig. 5, 6).

To rank contributions of different RTD BMs design parameters technological errors in the total dispersion of its electrical parameters graphs showing each technological errors contribution

Table 2. Parameters of simulated distributions of OSSC 1-1 (a) and 2-2 (b) conversion losses at the signal frequency 7.5 GHz under the combined impact of technological errors of NEs I-V characteristics, microstrip lines sizes, and substrates thickness and relative permittivity

Electrical parameter	Mean value, dB	Standard deviation, dB ²	Dispersion, dB ²
OSSC 1-1 conversion losses	13.8	0.66	0.44
OSSC 2-2 conversion losses	79.59	5.35	28.62

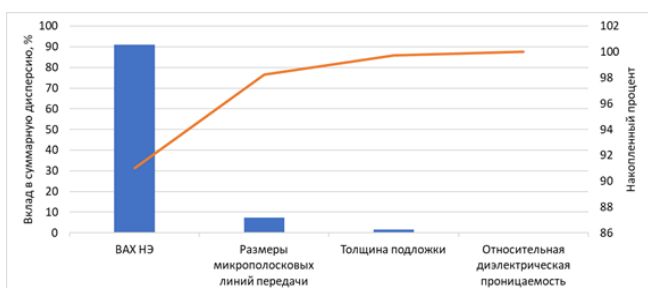


Fig. 5. Contributions of OSSC 1-1 conversion losses dispersions under the impact of different RTD BM's design parameters technological errors in the total dispersion.

in the total dispersion were plotted. Each technological errors contribution is evaluated by the ratio of the electrical parameters dispersion under the impact of said design parameters technological error to the dispersion of that electrical parameter under the combined impact of all design parameters' technological errors (Fig. 5, 6).

The analysis of different RTD BMs (microstrip lines sizes, substrates thickness and relative permittivity) and its NEs design parameters groups technological errors impacts on the RTD BMs electrical parameters distribution revealed that the maximal contribution in the total dispersion of the RTD BMs electrical parameter is made by the RTDs I-V characteristics technological error – RTD BMs electrical parameters dispersion under this factors influence is 91% from the total dispersion (Fig. 5, 6). In turn, the technological error of RTDs I-V characteristic is caused by the

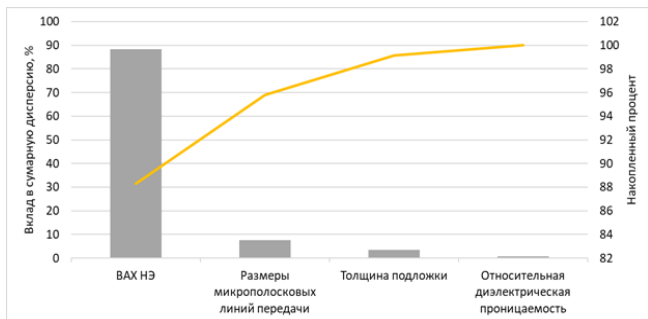


Fig. 6. Contributions of OSSC 2-2 conversion losses' dispersions under the impact of different RTD BM's design parameters technological errors in the total dispersion

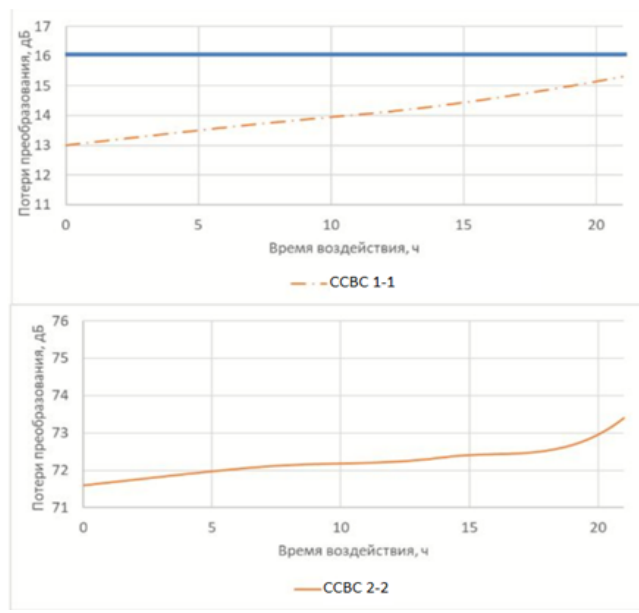
combined influence of RTD's design parameters technological errors: RTS layers thicknesses and chemical compositions, mesas area, and RTDs ohmic contacts parameters. Thus, it can be concluded that the NE's I-V characteristics technological error is the dominant factor determining the properties of the RTD BMs electrical parameters distribution. Obtained distributions of the RTD BMs electrical parameters under the combined impact of all design parameters technological errors are required for carrying out the BMs reliability assessment.

4. THE STUDY OF THE RTD BM'S ELECTRICAL PARAMETERS' KINETICS DURING OPERATION

For the nonlinear elements the impact of 250°C temperature during 21 h and gamma-irradiation dose of 375.1 Mrad was modelled. The measured I-V characteristic of the RTD of the given type was used as the initial I-V characteristic, the kinetics was modeled by the means of the software complex developed by the authors, using the models described in [7,11-12]. Obtained I-V characteristics were put into the studied BMs model in the AWR Microwave Office CAD as approximated polynomial current-voltage

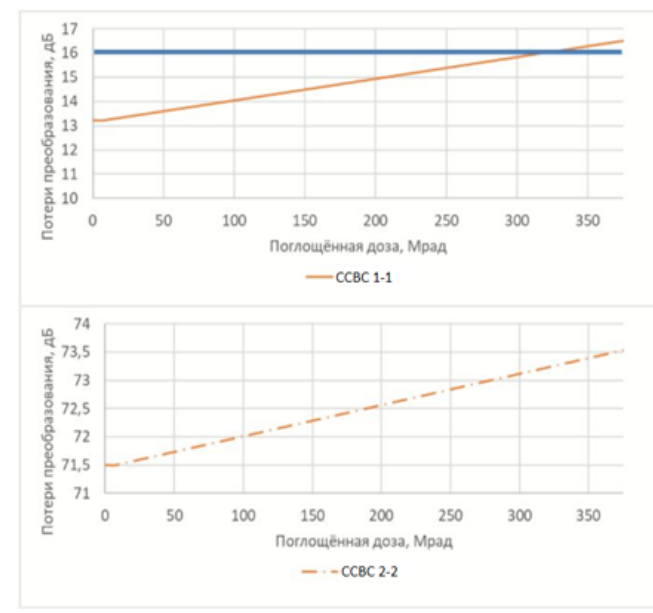
dependencies. Basing on the results of modeling of the studied RTD BMs electrical parameters, their kinetics under the ionizing irradiations and high temperatures impact at the signal frequency of 7.5 GHz is plotted (Fig. 7a,b). During the analysis, the failure is considered to occur if at least one of the following conditions is completed: OSSC 1-1 conversion losses are more than 16 dB; OSSC 2-2 conversion losses are less than 66 dB.

As shown in the Figures above, OSSC 1-1 and 2-2 conversion losses kinetics has a monotonously increasing trend both in the case of ionizing irradiation and high temperatures impact. The horizontal lines indicate the threshold values, on exceeding which a failure is recorded. Thresholds for OSSC 2-2 conversion losses are beyond the plot area since they're the lower boundary while conversion losses are increasing monotonously under destabilizing factors impact. Thus, the failure is only possible to occur because of the OSSC 1-1 conversion losses exceeding their threshold value. In the case of the ionizing irradiation exposure, the failure corresponds to 325 Mrad dose. The failure under the high temperatures impact wasnt registered on the studied time span. By the OSSC 1-1

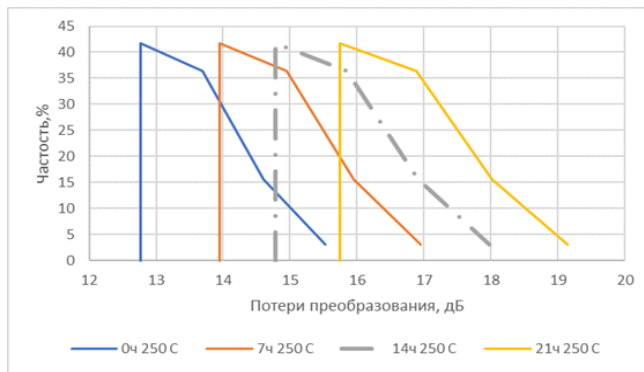


a

Fig. 7. Kinetics of the RTD BMs OSSC 1-1 and 2-2 conversion losses at the signal frequency of 7.5 GHz: (a) under the impact of 250°C temperature; (b) under the ionizing irradiations doses impact.



b



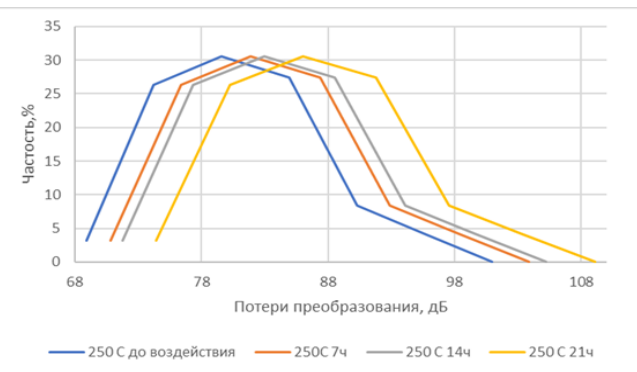
a

Fig. 8. The group kinetics of the RTD BM's OSSC 1-1 (a) and 2-2 (b) conversion losses at the signal frequency of 7.5 GHz under the impact of 250°C temperature.

conversion losses kinetics curve extrapolation it was revealed that the failure corresponds to the 25 h of exposure to the 250°C temperature.

Basing on the RTD BMs electrical parameters kinetics obtained for the single device in given operating condition (Fig. 7a,b) and the distributions of said electrical parameters obtained during the previous research (Fig. 4a,b), the group kinetics of the RTD BMs electrical parameters in given operating conditions were plotted (Fig. 8, 9a,b).

To obtain the gamma-percentage time to failure for $\gamma = 0.99$ corresponding to the actual operating conditions, the obtained values were converted into time to failure in actual operating conditions, using the technique described in [7,11-12]. The studied RTD BMs is supposed to be a part of near-earth orbit space crafts (SC) onboard equipment. The impact of the temperatures up to +200°C and ionizing irradiation doses up to 30 krad/year (according

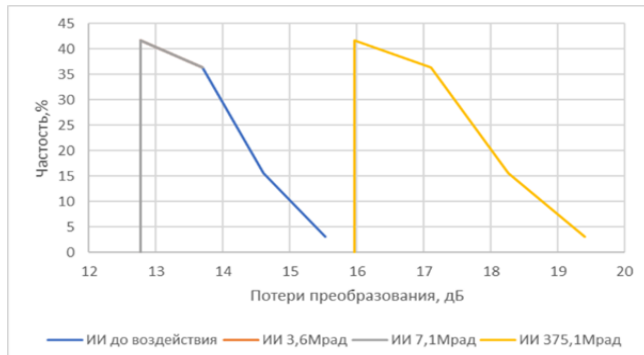


b

to [8-9,17], the absorbed dose for the onboard SCs equipment behind the mass protection of 1...2 г/cm² (which corresponds to typical values for protective material used in SCs), is 10...30 krad/year).

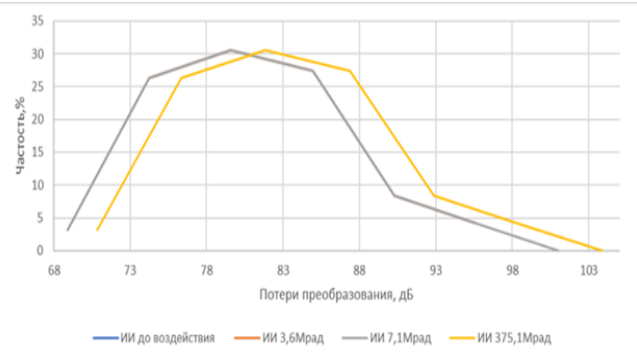
The obtained results analysis revealed that RTD usage as the BMs NE doesn't ensure proper reliability of the mixer during its operation under the high temperatures impact (the gamma-percentage time to failure $t_\gamma = 0.99$ under the 200°C temperatures impact doesn't exceed 6.5 years). Thus, it seems promising to develop the design and technological optimization algorithms along with the software complex implementing them to improve the mixers reliability.

To assess the studied BMs gamma-percentage time to failure under the ionizing irradiations impact the gamma-radiations dose causing the failure was converted into the operating time. Gamma-percentage time-to-failure $t_\gamma = 0.99$ for this case is more than 25 years, which proves high



a

Fig. 9. The group kinetics of the RTD BM's OSSC 1-1 (a) and 2-2 (b) conversion losses at the signal frequency of 7.5 GHz under the gamma-irradiation impact.



b

reliability of the studied BM under the ionizing irradiations impact.

5. CONCLUSION

The technique of assessment of the RTD-based FCs reliability for gradual failures in give operating conditions, considering the impact of the FCs design parameters technological errors on its electrical parameters distribution is developed.

The analysis of different groups of the broadband RTD BMs design parameters technological errors impact on the distribution of its electrical parameters was performed. The distributions of the RTD BMs electrical parameters under the impact of its design parameters (BMs topology, RTDs I-V characteristic, substrate thickness and relative permittivity) technological errors were obtained. It is revealed that the maximal contribution to the RTD BMs electrical parameters distribution is made by the technological error of RTDs I-V characteristic.

The broadband RTD BMs electrical parameters kinetics under ionizing irradiation and high temperatures impact was studied. The RTD BMs electrical parameters kinetics in given operating conditions is obtained. It is revealed that the BMs failure occurs due to the growth of the mixers conversion losses. Assessments of the BMs gamma-percentage time to failure corresponding to the operating conditions as part of the SCs onboard equipment at the near-earth orbit were obtained. The studied RTD BM doesn't provide sufficient reliability under the high temperatures impact. To increase the RTD BMs reliability under the said factors reliability it seems promising to perform the design and technological optimization of the RTD BMs electrical parameters.

REFERENCES

1. Diebold S, Tsuruda K, Kim J-Y, Mukai T, Fujita M, Nagatsuma T. A terahertz monolithic integrated resonant tunneling diode oscillator and mixer circuit. *Proc. of SPIE 9856, Terahertz Physics, Devices, and Systems X: Advanced Applications in Industry and Defense* (Baltimore), 2016, 9856 (Washington: SPIE), 98560U.
2. Hori T, Ozono T, Orihashi N, Asada M. Frequency mixing characteristics of room temperature resonant tunneling diodes at 100 and 200 GHz. *Journal of applied physics*, 2006, 99(6):064508-064508-7.
3. Kanaya H, Shibayama H, Suzuki S and Asada M. Fundamental Oscillation up to 1.31 THz in Resonant Tunneling Diodes with Thin Well and Barriers. *Applied Physics Express*, 2012, 5:124101.
4. Mizuta H and Tanoue T. High-speed and functional applications of resonant tunnelling diodes. In: *The Physics and Applications of Resonant Tunnelling Diodes*. New York: Cambridge university press, p. 133.
5. Meshkov SA. Methodology for consideration of technological and operational factors in design of micro- and nanodevices. *J. of Instr. Eng.*, 2019, 62:921-928
6. Srivastava A. Microfabricated Terahertz Vacuum Electron Devices: Technology, Capabilities and Performance Overview. *European Journal of Advances in Engineering and Technology*, 2015, 2(8):54-64.
7. Makeev MO, Meshkov SA and Cherkasov KV. Modeling of Resonant-Tunneling Diodes I-V Characteristics Kinetics Under Destabilizing Factors Influence During Operation. *Proc. Int. Russ. Automation Conf. (RusAutoCon 2019)*, p. 8867795.
8. Clowdsley M, Wilson J, Shinn J, Badavi F, Heinbockel J, Atwell W. Neutron Environment Calculations for Low Earth Orbit. *SAE Technical Papers*, 2001, 01ICES-2327.
9. Ravinarayana B. New Radiation Dose Model for Geostationary Orbit. *Journal of Spacecraft and Rocket*, 2009, 46(3):712-715.
10. Maekawa T, Kanaya H, Suzuki S and Asada M. Oscillation up to 1.92 THz in resonant tunneling diode by reduced conduction loss. *Applied Physics Express*, 2016, 9:024101.

11. Makeev MO, Sinyakin VYu and Meshkov SA. Reliability prediction of resonant tunneling diodes and non-linear radio signal converters based on them under influence of temperature factor and ionizing radiations. *Adv. in Astronautical Sci.*, 2018, 170:655-665.
12. Makeev MO, Meshkov SA, Sinyakin VYu, Ivanov YuA and Razoumny YuN. Reliability prediction of RFID passive tags power supply systems based on RTD under given operating conditions. *Adv. in Astronautical Sci.*, 2017, 161:475-483.
13. Wang J, Al-Khalidi A, Zhang C, Ofiare A, Wang L, Wasige E and Figueiredo JML. Resonant Tunneling Diode as High Speed Optical/Electronic Transmitter. In: *10th UK-Europe-China Workshop on Millimetre Waves and Terahertz Technologies* (UCMMT), Liverpool, UK, 11-13 Sept 2017: 1-4, ISBN 9781538627204 (doi: 10.1109/UCMMT.2017.8068497).
14. Sinyakin VYu, Makeev MO and Meshkov SA. RTD application in low power UHF rectifiers. *Journal of Physics: Conference Series*, 2016, 741:012160.
15. Ivanov YuA, Meshkov SA, Fedorenko IA, Fedorkova NV, Shashurin VD. Subharmonic mixer with improved intermodulation characteristics based on a resonant tunnel diode. *J. Commun. Technol. Electron.*, 2010, 55:921-927.
16. Nagatsuma T, Fujita M, Kaku A, Tsuji D, Nakai S, Tsuruda K, Mukai T. Terahertz Wireless Communications Using Resonant Tunneling Diodes as Transmitters and Receivers. *Proc. of Intern. Conf. on Telecommunications and Remote Sensing* (Luxembourg), 2014, 1:41-46.
17. Ravinarayana B, Upadhyaya N, Kulkarni R. Total radiation dose at geostationary orbit. *IEEE Transactions on Nuclear Science*, 2006, 52(2): 530-534.

DOI: 10.17725/rensit.2021.13.027

Controllable Inductors and Transformers Based On Ferromagnet-Piezoelectric Heterostructures

Leonid Yu. Fetisov, Dmitry V. Chashin, Yuri K. Fetisov

MIREA-Russian technological university, <https://mirea.ru/>

Moscow 119454, Russian Federation

E-mail: fetisovl@yandex.ru, chashindv@yandex.ru, fetisov@mirea.ru

Received January 19. 2021, peer-reviewed January 26.2021, accepted January 31.2021

Abstract: The elements of electrical circuits, which inductance L can be tuned electrically (the so-called "inductors"), and transforemers are used in modern electronics, radio engineering and low-power energy for galvanic isolation of circuits and converting voltage amplitudes. In this work, new devices of this type have been manufactured and investigated, using the magnetoelectric effect in ferromagnetic-piezoelectric heterostructures. The inductance of the manufactured inductor is tuned by 400% by a control electric field of up to 10 kV/cm applied to the piezoelectric layer of the structure, and by 1000% by an external magnetic field of up to 10 Oe, acting on the structure. The transformer operates in the range of input voltages of 0-8 V, has a power transfer coefficient of 30% and a voltage transformation ratio of 0-14, tunable by a control magnetic field of up to 80 Oe. Methods for calculating the characteristics of magnetoelectric inductor and transformer are described.

Keywords: magnetoelectric effect, transformer, inductor, piezoeffect, magnetostriction

UDC 538.955; 538.956

Acknowledgments: The research was funded by Russian Science Foundation (grant 19-79-10128).

For citation: Leonid Yu Fetisov, Dmitry V. Chashin, Yuri K. Fetisov. Controlled inductors and transformers based on ferromagnet-piezoelectric heterostructures. RENSIT, 2021, 13(1):27-38. DOI: 10.17725/rensit.2021.13.027.

CONTANTS

1. INTRODUCTION (27)
2. MAGNETOELECTRIC EFFECTS (28)
3. MAGNETOELECTRIC INDUCTOR (28)
 - 3.1. CONSTRUCTION OF THE INDUCTOR (29)
 - 3.2. INDUCTANCE SHIFT BY THE ELECTRIC FIELD (30)
 - 3.3. INDUCTANCE SHIFT BY THE MAGNETIC FIELD (31)
4. MAGNETOELECTRIC TRANSFORMER (34)
 - 4.1. CONSTRUCTION OF THE TRANSFORMER (34)
 - 4.2. CONTROL BY THE MAGNETIC FIELD (35)
 - 4.3. CALCULATION OF THE TRANSFORMER CHARACTERISTICS (37)
5. CONCLUSION (37)
- REFERENCES (37)

1. INTRODUCTION

Inductors (tunable inductance) and voltage transformers are among the most important components of modern electronics, radio engineering and low-power power engineering. Until recently, in the development of these devices, the main emphasis was on improving their parameters by improving the design and using new materials, increasing operational reliability, and reducing production costs. However, modern electronic components must not only be technically perfect and economical, but also "smart", what means that it is necessary to control their characteristics using external influences, which are usually understood as magnetic or electric fields.

Inductors are used in power supply control circuits, in telecommunication systems, data

acquisition and processing systems [1,2]. Currently, the most common are inductors, consisting of an electromagnetic coil, with a core made of a ferromagnetic material with high magnetic permeability inside. The inductance of the device is shifted by changing the magnetic permeability of the core using an external magnetic field.

Voltage transformers are used for conversion the amplitude of an alternating voltage and the galvanic isolation of elements of electronic circuits with respect to the dc voltage. Currently, compact transformers using the phenomenon of electromagnetic induction [3] and solid-state transformers using the piezoelectric effect [4] are widely used in low-power electronic circuits. However, both types of transformers have several disadvantages. In particular, electromagnetic transformers contain two volumetric coils, which makes them larger and more difficult to manufacture. Piezoelectric transformers have high input and output impedances. Both types of transformers do not allow quick rebuild the voltage transformation ratio.

In this work, the possibilities of creating a new type of inductors and transformers using magnetoelectric effects in ferromagnet-piezoelectric composite structures are demonstrated. It is shown that the characteristics of such devices can be easily controlled using electric and magnetic fields. In the beginning, the designs of some of the devices developed so far are described. Then a magnetoelectric inductor and a transformer of new designs, manufactured in the work, of higher characteristics, including tuning ranges, in comparison with the known ones, are described and investigated in detail.

2. MAGNETOELECTRIC EFFECTS

One of the ways to create controlled electronic devices is to use the so-called "magnetoelectric" (ME) effects in multiferroics. Materials that possess both magnetic and electrical ordering

are called multiferroics. These materials include a number of single crystals and artificially created composite materials containing ferromagnetic and ferroelectric components [5].

There are two types of ME effects: the direct ME effect is defined as the appearance (or change) of the electric moment of the sample P in an external magnetic field H , the inverse ME effect is defined as the appearance (change) of the magnetization of the sample M in an external electric field E .

The largest ME effect was found in layered composite heterostructures with ferromagnet and piezoelectric (FM-PE) layers. Magnetoelectric effect in such structures arise as a result of a combination of magnetostriction of FM layer and piezoelectricity in PE layer due to mechanical coupling between the layers. When the structure is exposed to an alternating magnetic field $b(f)$, magnetostriction leads to variable deformation of the FM layer, this deformation is transferred to the PE layer and it generates an alternating electric voltage $u(f)$ (direct ME effect). When an alternating electric field $e(f)$ is applied to the PE layer of the structure, it is deformed due to the inverse piezoelectric effect, the deformation is transferred to the FM layer, which, due to the reverse magnetostriction (or the Villari effect), leads to a periodic change in its magnetization $m(f)$ (reverse ME effect) [6,7].

By applying constant control magnetic or electric fields to the structure, the efficiency of ME conversions can be varied over a wide range. The use of layers made of various FM and PE materials also opens up wide possibilities for controlling the ME effects. Finally, we note that ME effects in composite heterostructures exist at room temperatures, which is extremely important for applications.

3. MAGNETOELECTRIC INDUCTOR

Inductors in which the inductance shift is carried out by a magnetic field due to a change in the magnetic permeability of a ferromagnetic core

are well known and described, for example, in [1]. Shift of inductance by an electric field was recently demonstrated in an inductor containing a ring of MnZn ferrite with a toroidal winding and a plate of lead zirconate titanate (PZT) inside the ring [8]. The inductance shift reached $\Delta L/L_{\min} = 20\%$ at field $E = 5 \text{ kV/cm}$. In an inductor based on a Metglas/PZT/Metglas planar structure placed inside an electromagnetic coil, a change in inductance by $\Delta L/L_{\min} = 450\%$ was observed under the action of a field $E = 12 \text{ kV/cm}$ [9]. In [10,11], the characteristics of electrically tunable planar inductors with FM layers made of Metglas, FeGa, MnZn- and NiCo-ferrites and PE layers made of PZT and PMN-PT ceramics were studied. In [12], an inductor based on a structure with layers of NiZn ferrite doped with Ga and PZT is described, which inductance was tuned by both a magnetic and an electric field.

3.1 CONSTRUCTION OF ME INDUCTOR

The design of the manufactured in the work ME inductor is schematically shown in **Fig. 1**. The main element of the inductor is a ring made of PE material with its outer surface covered with the FM material. The ring shape of the inductor core allows obtaining high inductance value while maintaining a small size of the device and also it minimizes electromagnetic stray fields in the interference with the surrounding space. The PE ring is made of widely used piezoceramics PZT-19 (manufactured by the

JSC Research Institute “Elpa”, Russia) and has an outer diameter $D = 17 \text{ mm}$, thickness $a_p = 1 \text{ mm}$ and height 5 mm.

The Ag electrodes $\sim 2 \mu\text{m}$ thick each, were deposited both on the outer and inner surfaces of the ring by firing. And the ring was polarized in the radial direction by applying a constant voltage of 600 V to the electrodes at a temperature of 100°C . The piezoceramics PZT-19 has a piezoelectric modulus $d_{31} = -175 \text{ pm/V}$ and density was $\rho_p = 7.5 \cdot 10^3 \text{ kg/m}^3$. An amorphous magnetic FeBSiC ribbon (Metglas 2605SA1, Metglas Co, USA) with a thickness $a_m \approx 25 \mu\text{m}$, width $b = 5 \text{ mm}$ and length 55 mm served as an FM layer. Amorphous FM alloy had a saturation inductance $B_s \approx 1.6 \text{ T}$, maximal magnetic permeability $\mu \approx 30000$, saturation magnetostriction $\lambda_s \approx 27 \cdot 10^{-6}$ and the resistivity $\rho_m = 130 \cdot 10^{-6} \text{ Ohm}\cdot\text{cm}$. The FM ribbon was glued to the outer surface of the PE ring using cyanoacrylate adhesive, which ensured the efficient transfer of deformations across the interface. The structure was embedded in a plastic frame with wound toroidal coil, which consisted of $N = 100$ turns of wire 0.2 mm in diameter. The active resistance of the coil with the structure inside was $R = 1.13 \text{ Ohm}$, the inductance was $L \approx 75 \mu\text{H}$, and the capacitance of the structure was $C = 3.5 \text{ nF}$. The inductance L and the quality factor $Q = 2\pi f L/R$ were measured by the serial resonance method using an AKTAKOM AM-3026 RLC meter in the frequency range $f = 20 \text{ Hz} - 5 \text{ MHz}$ with an accuracy of 0.1%. We investigated the change of the inductance L using constant magnetic H and electric E fields. A radial electric field in a PE ring with a strength of $E = 0-18 \text{ kV/cm}$ was created by applying a voltage $U = 0-18 \text{ kV}$ to the ring electrodes from a Stanford Research Systems PS350 high-voltage source. Magnetic field $H = 0-200 \text{ Oe}$ was created using Helmholtz coils 15 cm in diameter. Two cases were considered: (1) the field is applied along the axis of the ring structure (shown in Fig. 1) and (2) the field is applied in the plane of the structure. Also, the

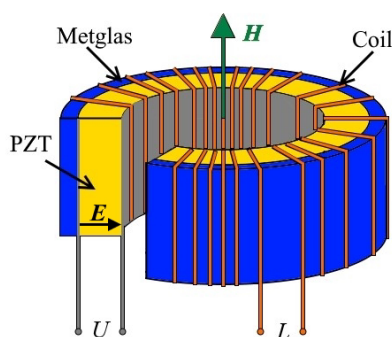


Fig. 1. Schematic of the magnetoelectric inductor. Arrows indicate the direction of the electric field E in the PE ring and the direction of the magnetic field H .

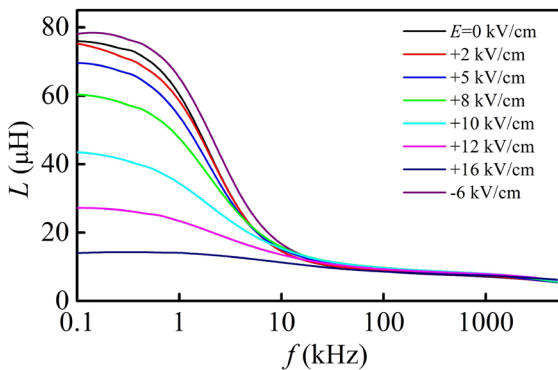


Fig. 2. Dependences of the inductance L of the ME inductor on the frequency f when at different electric fields E .

change of L was investigated using a circular field H created by a direct current $I = 0\text{--}200$ mA flowing through an additional toroidal coil wound on a structure.

3.2. INDUCTANCE SHIFT BY THE ELECTRIC FIELD

The tuning of the device inductance by an electric field E was done by applying a DC voltage of up to $U = 1800$ V to the electrodes on the PZT layer. **Fig. 2** shows the dependences of L on the frequency f for different values of E . The applied field polarity $E > 0$ corresponds to the stretching of the PZT ring due to converse piezoelectric effect. It can be seen, that for all E , L decreases monotonically with increasing f and at the constant f , L decreases with increasing E . In this case, the maximum and minimum L reached $L_{\max} \approx 80$ μH and $L_{\min} = 5.5$ μH , respectively. The tuning of L by E was observed in the frequency range up to ~ 10 kHz. The tuning coefficient of the inductor by the electric field reached ≈ 412 % (where L_0 is the induction in the absence of magnetic field).

Fig. 3 shows the dependences of L on the field at a frequency of 300 Hz when the field E changes in a closed cycle with large amplitude or smaller limits. Without the field ($E = 0$) at a starting point "A" the inductance was $L_0 = 76$ μH . One can see from Fig. 3a that with increasing E in the positive direction ($E > 0$), L first slowly increases monotonically to 82 μH , then sharply drops at a field $E \approx E_c$ and after that continues to decrease slowly to $L \approx 15$ μH as the field increases to 18 kV/cm. During the subsequent decreasing E to zero, the inductance monotonically increases to a value of $L \approx 70$ μH . After the change in the field polarity ($E < 0$) and a subsequent increase in the field, the inductance behaves similarly: at first, it increases monotonically, and then at $E \approx -E_c$ it drops abruptly and continues to decrease to $L \approx 15$ μH at 18 kV/cm. In the last segment of the curve, when E increases from -18 kV/cm to zero, the inductance also monotonically increases to 70 μH . The characteristic fields $E_c \approx \pm 10$ kV/cm correspond to the polarization reversal field of the PZT ring, at which the polarization vector P in the piezoelectric reverses its direction.

It is seen, that at the field amplitudes more than E_c , the electrical tuning of the inductor is essentially nonlinear and has a large hysteresis. The hysteresis is much less when E changes within smaller limits and moves only along the lower part of the curve in Fig. 3a, where there is no repolarization of the structure. Nevertheless, even in this case, the

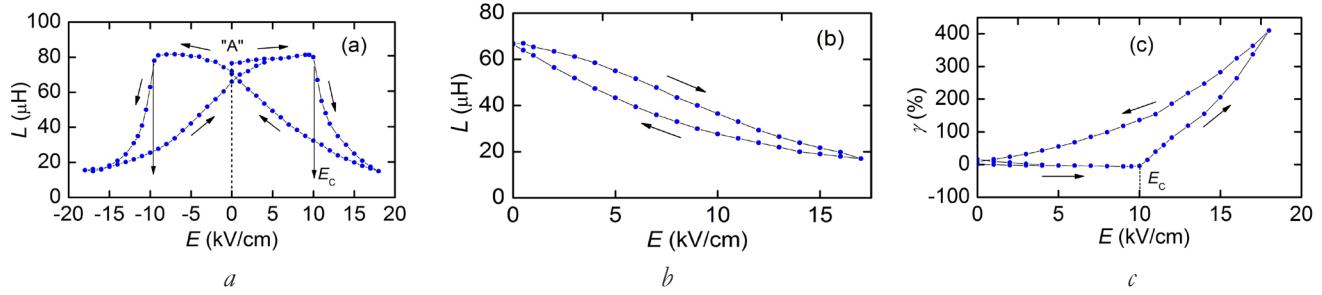


Fig. 3. Dependence of the structure's inductance L on the field E at 300 Hz (a) when the field cycles with large amplitudes and (b) when E changes within smaller limits ($E > 0$). (c) Inductance tuning coefficient γ dependence on the field E . E_c is the field of polarization reversal of the PZT ring. Arrows indicate the direction of change in field E .

dependence $L(E)$ remains nonlinear. Fig. 3c shows the dependence $\gamma(E)$, obtained using the data in Fig 3a for $E > 0$. The maximum tuning of the inductance by an electric field reached $\gamma = 413\%$ at 300 Hz.

The change in the inductance of the ME inductor under the action of an electric voltage is associated with a change in the permeability of the magnetic layer due to the converse ME effect. the structure's magnetic permeability μ depends on E as [13]

$$\mu_r = \chi + 1 = \frac{\mu_0 M_s^2}{2 |K_0 + K_\sigma|} + 1, \quad (1)$$

$$K_\sigma = \frac{3}{2} \lambda_c \sigma, \quad (2)$$

where μ_0 is the magnetic permeability of vacuum, M_s is the saturation magnetization, K_0 – is the initial anisotropy constant (including both magnetocrystalline and shape anisotropies), K_σ is the stress-induced magnetoelastic anisotropy (stress anisotropy), λ_s is the saturation magnetostriction, σ is the applied stress. Mechanical stresses applied to the magnetic layer are formed as a result of the action of the piezoelectric layer in a ME inductor. Therefore, μ_r correlates with the electric field applied to the piezoelectric layer, and relation (1) transforms into:

$$\mu_r = \frac{\mu_0 M_s^w}{2 K_0 + 3 \lambda_s Y d_{eff} E} + 1, \quad (3)$$

where d_{eff} is the effective piezoelectric strain coefficient, Y is the Young's modulus, E is the electric field, applied to the piezoelectric. Since the change in the linear dimensions of the inductors due to the piezoelectric effect and magnetostriction) is small ($< 0.5\%$), and the magnetic permeability μ_r of the magnetic material is much greater than 1, the change in inductance should be directly proportional to μ_r . In this case the induction tuning coefficient γ is related to the electric field E by the following expression [14]:

$$\gamma = \frac{L_0 - L_E}{L_E} = \frac{3}{2} \frac{\lambda_s}{K_0} Y d_{eff} E. \quad (4)$$

3.3. INDUCTANCE SHIFT BY THE MAGNETIC FIELD

Fig. 4 shows the dependences of L of ME inductor on the frequency f when it is magnetized by an external magnetic field H directed along the ring axis. One can see from figure that at any field in the range $H = 0$ -200 Oe the inductance L is approximately constant in the low-frequency region, and then decreases monotonically with increasing frequency. The frequency range, in which L is constant, expands from ~ 0.2 kHz at $H \sim 0$ to ~ 100 kHz when the field H increased from zero to 200 Oe. However, the absolute value of L decreases with H increasing. The maximum inductance value was $L_{max} = 77 \mu\text{H}$ at a frequency of 0.1 kHz. The minimum inductance value was $L_{min} = 6 \mu\text{H}$ in the high-frequency region ~ 5 MHz for all fields. Dependences similar in shape were obtained for two other orientations of the magnetic field: in the plane of the structure and using a circular field. The main difference lies in the range of the applied magnetic field, which for these cases was $H = 0$ -20 Oe.

Fig. 5 shows the dependences of the inductance L of the ME inductor and the inductance tuning coefficient γ on the magnetic field and on the control current (for the case of a circular magnetic field). The measurements were

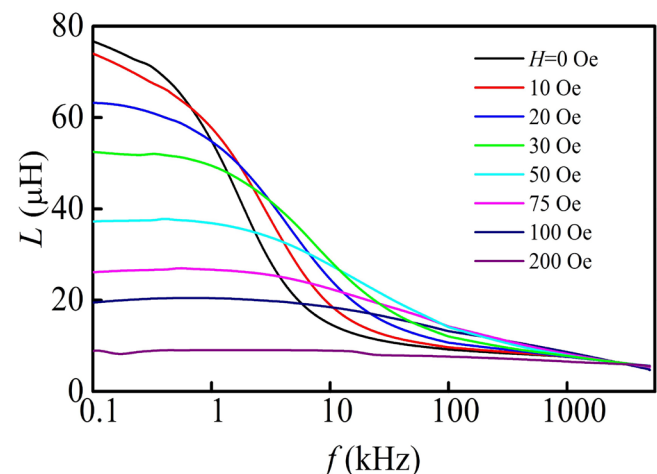


Fig. 4. Dependences of the inductance L on the frequency f when magnetized by the field H along the axis of the structure.

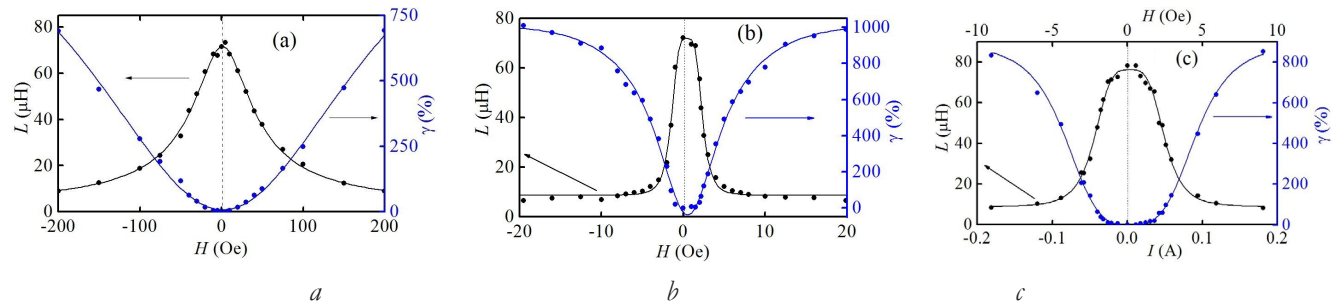


Fig. 5. Dependence of the L and the tuning inductance coefficient γ on the field H (current I) when the field is: (a) directed along the axis; (b) directed in the plane; (c) directed along the generatrix of the structure. The measurements were carried out at a frequency of 300 Hz.

carried out at a frequency of 300 Hz. The values $H < 0$ correspond to the field with reversed direction. It can be seen for all three magnetic field directions, that L does not depend on the direction of the field and decreases monotonically with increasing H .

The inductance decreases by a factor of ~ 8 at a frequency of 300 Hz under the influence of magnetic field in case of the field orientation along the structure axis (Fig. 5a). As follows from Fig. 4, the tuning range of L under the action of the field decreases with increasing frequency. in the low-frequency region, the tuning coefficient of the device inductance in a magnetic field directed parallel to the axis of the structure was $\gamma \approx 690\%$ with a control field up to $H = 200$ Oe.

In the case of the field orientation in the plane of the structure (Fig. 5b), the inductance L drops to a minimum value in a field $H \sim 20$ Oe, which is ~ 10 times less than in the previous case. At the frequency of 300 Hz, L decreases by ~ 11 times under the influence of a magnetic field. The maximum value of γ reaches $\approx 1000\%$ at the control field $H \approx 20$ Oe when the structure is magnetized in the plane.

Fig. 5c shows dependences of the inductance L of the ME inductor on the control current when it is magnetized by a circular magnetic field H . For a comparison with the previous cases, the upper axis in Fig. 5c indicates the calculated value of H created by the current through the coil at the location of the FM layer. The drop rate of the inductance with increasing H is higher than

in the previous cases. The maximum tuning coefficient of the inductance when the structure is magnetized by the field of the toroidal coil reached $\gamma \approx 850\%$ at a value of the control current $I = 0.18$ A ($H = 9$ Oe).

The inductance of the ME inductor L changes due to a change in the magnetic permeability of the FM layer. The relative changes in the dimensions of the structure due to magnetostriction are no more than 10^{-4} and can be ignored.

Additional measurements were carried out in order to explain the mechanism of the restructuring of the inductor by the magnetic field. **Fig. 6** shows the measured magnetization curve $B(H)$ for a test sample made of a Metglas 2605SA1 ribbon with dimensions 15 mm \times 5 mm \times 23 μm , magnetized along the long axis. In the same figure, we've also plotted field

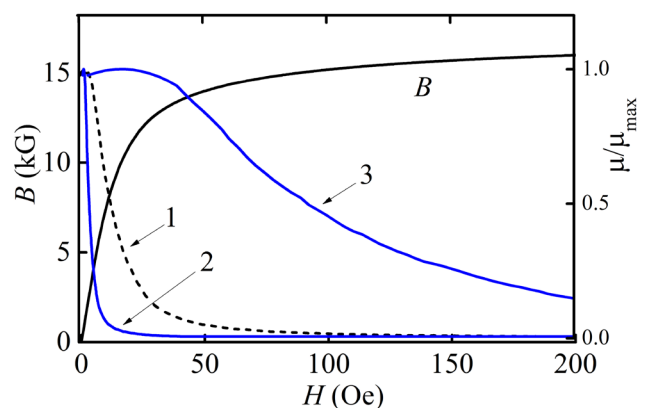


Fig. 6. Field dependences of the magnetic induction B for the Metglas test sample and the normalized permeability μ/μ_{\max} for: 1 – test sample; 2 – the ring structure magnetized with a circular field; 3 – the ring structure magnetized along the axis.

dependence of the real part of the normalized magnetic permeability $\mu'(H)/\mu_{max}$, obtained by numerical differentiation of the $B(H)$ curve. One can see that in the low field region the permeability is approximately constant and then gradually drops to zero with increasing H . This dependence $\mu(H)$ that makes it possible to change the inductance using the magnetic field H . For a qualitative explanation of the cases considered above, let us take into account the demagnetization effects.

It is known that in an FM sample of finite dimensions, due to demagnetization, the average field H_{in} inside the ferromagnetic is less than the external field H and is related to it by the relation [15]

$$H_{in} \approx \frac{H}{1+N\chi}, \quad (5)$$

where N is the demagnetizing factor of the sample along the direction of the field, and $\chi(H=0)$ is the initial magnetic susceptibility. For Metglas $\chi \gg 1$, so we can take $\chi = \mu(0)$. Thus, demagnetization leads to a scaling of the external magnetic field by the factor of $1+N\mu(0)$. By measuring the field dependence $\mu(H)$ for an FM sample with known N and knowing N for another sample, it is possible to construct a field dependence $\mu(H)$ for the second sample. The demagnetizing factors for the FM sample in the form of a rectangular prism were calculated in [16]. The field dependences $\mu(H)$ calculated using the measured curve $B(H)$ for the test sample and equation (4) for the FM strip magnetized along the length and along the width are also shown in Fig. 6. We assume that for an FM ring magnetized with a circular magnetic field, the dependences $\mu(H)$ have a similar form.

Then it follows from Fig. 6 that when the ring structure is magnetized with a circular magnetic field along the generatrix, μ decreases, for example, by a factor of 5, in a magnetic field $H \approx 4$ Oe. That is consistent with a 5 times decrease in the inductance L of the inductor as it is shown in Fig. 5c when the field changes by approximately

4.5 Oe. Magnetic permeability μ decreases much more slowly due to the strong demagnetization when the ring structure is magnetized along the axis. Magnetic permeability on curve 3 in Fig. 6 decreases 5 times when the field changes by 150 Oe, which is in a good agreement with a 5 times decrease of L in Fig. 5c when the field changes by ~ 135 Oe.

The magnetic hysteresis of the structures FM layer upon cycle tuning of the inductor by a magnetic field leads to an uncertainty in the set value of L . The coercive force for the amorphous alloy Metglas 2605SA1 was $H_c \approx 0.2$ Oe. The maximum inductance setting error was $\Delta L/L \approx 0.3\%$ when the structure was magnetized along the axis and $\Delta L/L \approx 12\%$ when the structure was magnetized with a circular magnetic field created by additional coil.

Fig. 7 demonstrates the possibility of tuning the inductor simultaneously by the current I through the control coil (i.e. by the magnetic field H) and the electric field E applied to the PZT-ring. In the absence of current at $E=0$, the inductance was $L \approx 75 \mu\text{H}$. The inductance decreases monotonically with increasing current I and electric field E . Therefore, with an increase in the field E , the tuning range of the inductance by the current narrows.

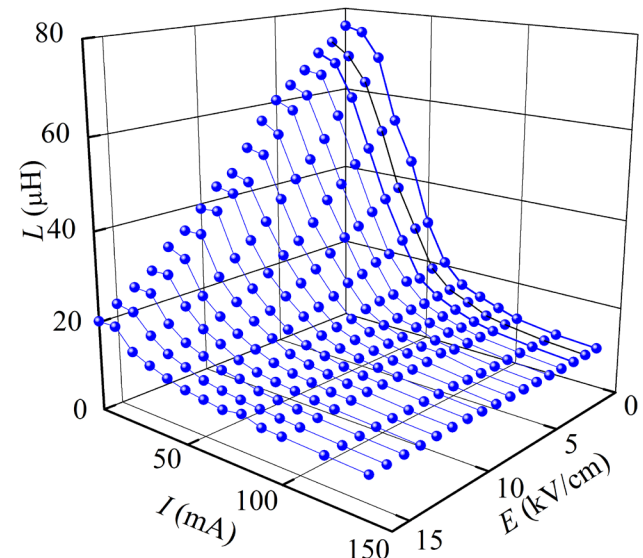


Fig. 7. Dependencies of inductance L on the current I through the control coil at different values of electric fields E .

4. MAGNETOELECTRIC TRANSFORMER

To date, several different designs of ME transformers have been proposed. Models of both step-up [17-19] (operating on the direct ME effect) and step-down transformers [20-22] (operating on the converse ME effect) based on heterostructures with layers of various FM and PE materials have been created and investigated. The possibilities of controlling the voltage transformation ratio using a constant magnetic field [18,23] or a constant electric field [24] applied to the structure have been demonstrated. Methods for calculating the characteristics of ME transformers of various designs are proposed [25].

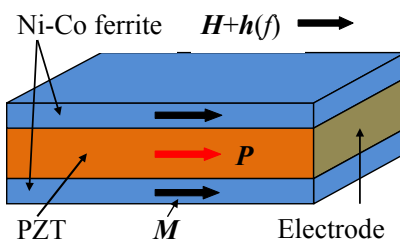
4.1. CONSTRUCTION OF THE TRANSFORMER

The composite heterostructure and the design of the ME transformer are schematically shown in Fig. 8a and 8b, respectively. The main element of the transformer is a three-layer heterostructure containing a PE layer sandwiched between two FM layers [26]. The PE layer with dimensions of 20 mm×10 mm and a thickness $a_p = 2$ mm is made of transformer piezoceramics $\text{Pb}(\text{Zr},\text{Ti})\text{O}_3$ (PZT-47 type, manufactured by the JSC Research Institute "Elpa", Russia). The pie-zoceramics has a piezoelectric modulus $d_{33} = 290 \text{ pC/N}$, high electromechanical quality factor $Q = 900$, an electromechanical coupling coefficient $k_p = 0.56$, a dielectric loss tangent $\tan\delta < 0.6$, and the Curie temperature $T_c = 270^\circ\text{C}$. Ag-electrodes were deposited on the end faces of the PE layer and it was poled in the direction of the long axis. The capacitance between the electrodes

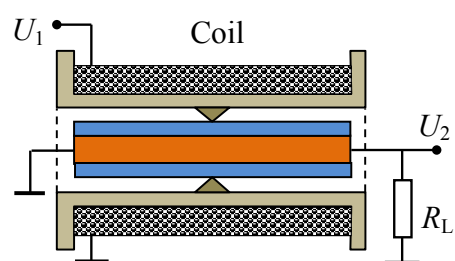
of the PE cell was $C_2 = 66.3 \text{ pF}$. Ferromagnetic layers, 20 mm×10 mm in size and $a_m = 0.5$ mm thick each, are made of magnetostrictive nickel ferrite of composition $\text{Ni}_{0.99}\text{Co}_{0.01}\text{F}_2\text{O}_3$. The layers had a saturation induction $B_s = 0.33 \text{ T}$, a saturation magnetostriction $\lambda_s = 26 \cdot 10^{-6}$, initial magnetic permeability $\mu = 51$, a magnetomechanical coupling coefficient $k_m = 0.2$, and Curie temperature $T_c = 500^\circ\text{C}$. The layers of piezoceramics and ferrite were coupled under pressure using a cyanoacrylate adhesive.

The structure was placed inside a 20 mm long electromagnetic coil, containing 120 turns of a wire with a thickness of 0.2 mm. The coil generated an alternating magnetic field h with the variable frequency f . The structure was rigidly fixed in its central transversal plane for the most efficient excitation of the fundamental mode of longitudinal acoustic vibrations. The resistance and inductance of the coil with the structure inside were $R_i = 2.3\Omega$ and $L = 168 \mu\text{H}$, respectively. A control magnetic field $H = 0\text{-}200 \text{ Oe}$ was applied parallel to the long axis of the structure and the axis of the coil using an electromagnet.

During the measurements, the voltage $U_1 \cos(2\pi f t)$ from a generator (Agilent 33210A), with an amplitude U_1 up to 8 V and a variable frequency $f = 0\text{-}200 \text{ kHz}$, was applied to the input coil of the transformer. The output voltage of the transformer U_2 was measured at the load resistance R_L . Both input and output voltages were measured using a voltmeter (AKIP 2401) with an input impedance of more than 10 MΩ. The voltage transformation ratio of the



a



b

Fig. 8. Schematic view of (a) the Ni-Co-ferrite-PZT heterostructure and (b) the transformer. The arrows denote directions of magnetic field H , magnetization M , and polarization P .

transformer was determined as $K = U_2/U_1$. To measure the input power P_1 of the transformer, a shunt resistor was connected in series with the coil to determine the current I_1 . The input active power was calculated by the formula $P_1 = U_1 I_1 \cos(\varphi)$, where φ is the phase shift between voltage and current. The active power in the output circuit was calculated as $P_2 = U_2^2 / R_L$. The transformer characteristics were recorded for the cases when the frequency f and the amplitude U_1 of the input voltage, the control magnetic field H and the load resistance R_L were varied.

4.2. CONTROL BY THE MAGNETIC FIELD

Fig. 9 shows a typical measured amplitude-frequency response of a transformer with an input voltage $U_1 = 1$ V and a constant magnetic field of $H = 80$ Oe for the open-circuit condition (at $R_L = \infty$). One resonance peak around the frequency $f_0 \approx 99$ kHz was observed in the frequency response. The resonance quality factor was estimated from the width of the resonance curve δf at a height of 0.7: $Q = f_0/\delta f \approx 143$. The voltage transformation ratio at the resonance frequency is $K = U_2/U_1 = 14.1$. The calculated value of the resonance frequency of the structure was $f_0 \approx 100.4$ kHz, which is in good agreement with the measured value.

The most important feature of the ME transformer, in comparison with electromagnetic and piezoelectric transformers, is the ability to control the voltage transformation ratio using an external magnetic field. **Fig. 10** shows the measured dependences of the voltage transformation ratio K on the frequency f of the input voltage with amplitude 1 V in the absence

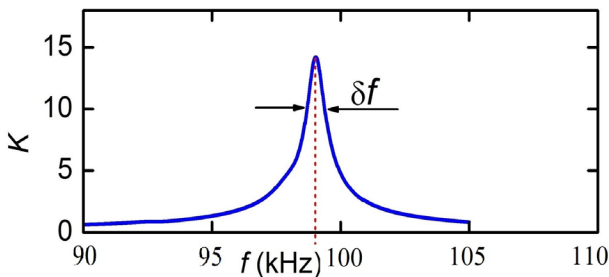


Fig. 9. Dependences of the output voltage U_2 on the voltage frequency f at $U_1 = 1$ V.

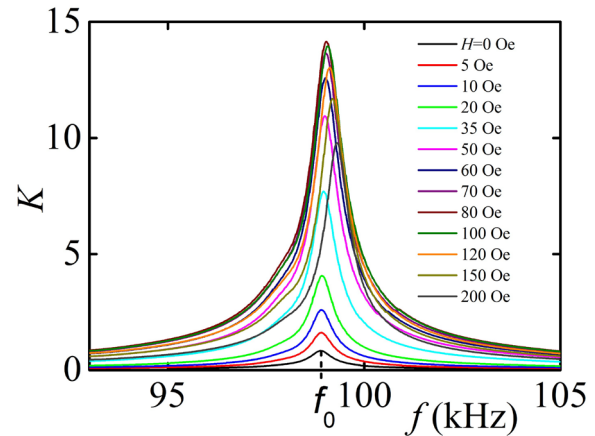


Fig. 10. Dependences of the voltage transformation ratio K on the frequency f for different control fields H (0 - 200 Oe) under open-circuit condition.

of a load resistance. It is seen that an increase in the field H leads to a strong change in the transformation ratio K and a small shift in the resonance frequency f_0 .

Fig. 11 demonstrates the dependences of the transformation ratio K , the resonance frequency f_0 , and the quality factor of resonance Q on the control magnetic field H , derived from the data in Fig. 10. It can be seen that with increasing field, the transformation ratio K increases approximately linearly from zero to a maximum value of $K = 14.1$ in the field $H_m \approx 80$ Oe, and then monotonously declines with a further increase in the field. The resonance frequency f_0 grows almost linearly by 0.4% with the increasing magnetic field. The resonance

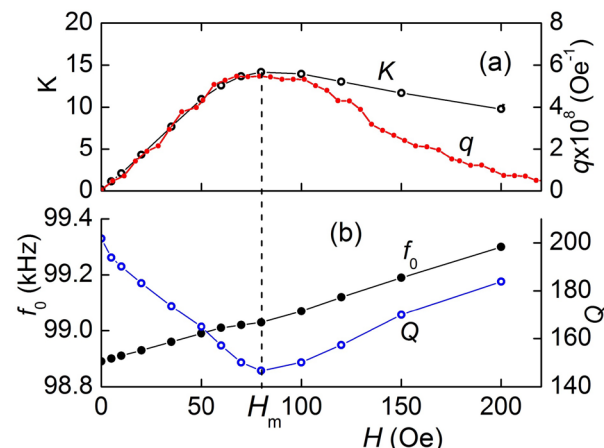


Fig. 11. Field dependences of (a) the transformation ratio K and the piezomagnetic coefficient q , and (b) the resonance frequency f_0 as well as the quality factor Q under open-circuit condition.

quality factor decreases from $\mathcal{Q} \approx 200$ in the absence of a field to a minimum value of $\mathcal{Q} \approx 143$ in the same field $H_m \approx 80$ Oe, and then rises again to $\mathcal{Q} \approx 189$ at $H = 200$ Oe.

The capability to control the voltage transformation ratio is caused by the dependence of the magnitude of the direct ME effect in composite structures on a constant field. To confirm this conclusion, the field dependence of magnetostriction $\lambda(H)$ was measured by a strain gauge glued to the surface of the ferrite layer. Then, using the numerical differentiation, the field dependence of the piezomagnetic coefficient $q(H)$ was found. The obtained dependence $q(H)$ is shown in Fig. 11a. For convenience of comparison, the scale along the vertical axis for q is chosen so, that the maxima of the dependences $K(H)$ and $q(H)$ visually coincide. It can be seen that the pie-zomagnetic coefficient q initially linearly increases with increasing field H , reaches a maximum at the same characteristic field $H_m \approx 80$ Oe, and then decreases as the ferrite layer is saturated. The shapes of the field dependences $K(H)$ and $q(H)$ agree qualitatively well. The discrepancy between the curves in the region of large fields can be due to the influence of the Poisson's effect and the inhomogeneity of the magnetic field inside the FM plates due to the demagnetizing fields, which were not taken into account in the calculations. The dependence of the resonance frequency f_0 and the quality factor Q of the structure on the field H (Fig. 11b) is caused by the dependence of the Young's modulus and the mechanical losses of the ferrite layer on the magnetic field H .

Next, the characteristics of the transformer were measured in dependence on the load resistance in the range $R_L = 0-220$ kOhm at optimal bias magnetic field $H_m = 80$ Oe and amplitude of the input voltage $U_1 = 1$ V. Fig. 12 presents the dependences of the transformation ratio K , output power P_2 , frequency f_0 , and Q -factor of resonance on the load resistance R_L . It can be seen that the transformation ratio increases monotonically from zero to 14.1 with

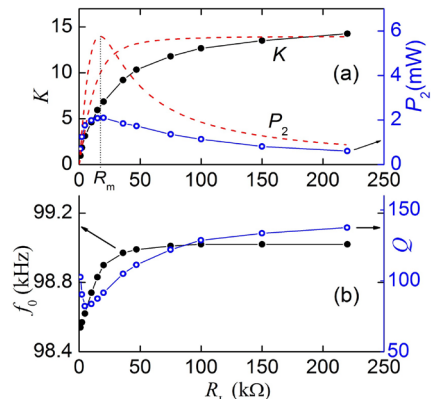


Fig. 12. Dependences of (a) the voltage transformation ratio K and the output power P_2 on the load resistance R_L and (b) the resonance frequency f_0 and the quality factor Q on the load resistance R_L at $H = 80$ Oe. The dashed lines in (a) are the calculated dependences.

the load resistance increasing up to $R_L = 220$ kΩ. In this case, the output power P_2 varies non-monotonically: first it increases from zero and reaches a maximum $P_m \approx 1.18$ mW with a load resistance of $R_m \approx 18-20$ kΩ, and then monotonously decreases to $P_2 \approx 0.9$ mW with a further increase in resistance to $R_L = 220$ kΩ. With an output voltage $U_2 = 50$ V, it was 125 mW.

The resonance frequency f_0 monotonously increases by less than 0.5%, from 98.54 kHz to 99.02 kHz with the increasing load. The resonance quality factor Q first steeply decreases with the increasing load resistance from $Q \approx 100$ to $Q \approx 80$ at $R_L \approx 5$ kΩ, and then again increases to $Q \approx 142$ at high load resistances (see Fig. 11b).

Fig. 13 shows the dependence of the ME transformer output voltage on its input voltage at different load resistances. It can be seen that in the investigated input voltage range of 0-8 V the dependences are linear and the range of the output voltages of the transformer reaches hundreds of volts.

4.3. CALCULATION OF THE TRANSFORMER CHARACTERISTICS

To explain the dependencies shown in Fig. 12a, we write the equation for the current in the output circuit of the transformer

$$I_2 = \frac{U_{ME}}{\sqrt{\frac{R_2^2(1/\omega C)^2}{R_2^2 + (1/\omega C)^2} + R_L^2}}, \quad (6)$$

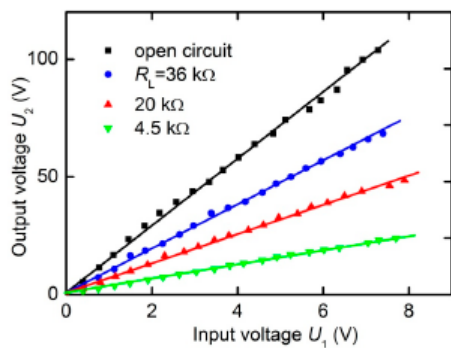


Fig. 13. Dependences of the output voltage U_2 on the input voltage U_1 at the resonance frequency f_0 and $H_m = 80$ Oe for different load resistances R_L ($4.5 \text{ k}\Omega$, $20 \text{ k}\Omega$, $36 \text{ k}\Omega$) and under open-circuit conditions.

where U_{ME} is the amplitude of the voltage in the output circuit induced by the ME effect. At the resonance frequency the measured active resistance and capacity of the PZT layer were $R_2 \approx 17 \text{ k}\Omega$ and $C \approx 66.3 \text{ pF}$, i.e. the condition $R_2 \ll 1/(\omega C)$ fulfilled, where $\omega = 2\pi f$. Then for the output voltage we get

$$U_2 = I_2 R_L \approx \frac{U_{ME} R_L}{\sqrt{R_2^2 + R_L^2}}. \quad (7)$$

The dependence $K(R_L) = U_2(R_L)/U_1$ calculated using (6) for the amplitude of the ME voltage $U_{ME} = 15 \text{ V}$ is shown in Fig. 12a with a dashed line. It can be seen that the theory describes the dependence of the transformation ratio on the load resistance qualitatively well. For the output power P_2 , using formula (2) and mention ($R_2^2 \ll 1/(\omega C)$), we obtain the expression

$$P_2 = I_2^2 R_L = \frac{U_{ME}^2 R_L}{R_2^2 + R_L^2}. \quad (8)$$

The power at the transformer output, reaches its maximum value at $R_L \approx R_2 \approx 17.7 \text{ k}\Omega$. The dependence $P_2(R_L)$ calculated using (7) with the parameter values $U_{ME} = 15 \text{ V}$ and $R_2 = 15 \text{ k}\Omega$ is also shown in Fig. 12a with a dashed line. Thus, the theory qualitatively well describes the dependence of the output power on the load resistance.

6. CONCLUSION

Thus, in this work, an ME inductor with a variable inductance tuning coefficient and an

ME transformer with a controlled voltage transformation ratio of new designs were manufactured and investigated.

A unique property of an ME inductor is the ability to tune its inductance using external electric and magnetic fields. The inductance L of the device is tuned within $\sim 65 \mu\text{H}$ by electric and magnetic fields. The control magnetic field is minimal ~ 10 Oe when the ring structure is magnetized in the plane or along the generatrix and increases to ~ 200 Oe when the structure is magnetized along the axis due to demagnetization effects. The inductance tuning coefficient was $\sim 400\%$ for electrical and $\sim 1000\%$ for magnetic tuning. The power consumption for magnetic and electrical tuning of the inductor is approximately comparable in magnitude and amounts to $\sim 1-10 \text{ mW}$. However, electrical tuning does not require additional power to maintain a given inductance.

A unique property of the ME transformer is the change of the voltage transformation ratio by an external magnetic field. The transformer operates in the input voltage range of 0-8 V, the voltage transformation ratio reaches $K = 14.1$ and is shifted from zero to the maximum value when the magnetic field H changes from zero to 80 Oe. The amplitude of the output voltage is linearly dependent on the input voltage in the input voltage range from zero to 8 V. With an optimal load resistance of $20 \text{ k}\Omega$, the maximum power at the transformer output reached 125 mW, while the maximum power transfer coefficient was $\sim 30.5\%$.

REFERENCES

1. Hurley WG, Wolfe WH. *Transformers and Inductors for Power Electronics: Theory, Design and Applications* (1st ed.). WILEY, 2013, 370 pages.
2. Mathuna CO, Wang N, Kulkami S and Roy S. Review of integrated magnetics for power supply on chip (PwrSoC), *IEEE Tran. On Power Electronics*, 2012, 27(11):4799-4816.
3. Harlow JH. *Electric Power Transformer Engineering* (3rd ed.). CRC Press, Taylor and Francis Group: Boca Raton, FL, USA, 2017.
4. Carazo AV. *Piezoelectric Transformers: An*

- Historical Review. *Actuators*, 2016, 5:12.
5. Пятаков АП, Звездин АК. Магнитоэлектрические материалы и мультиферроики. УФН, 2012, 182(6):593-620.
 6. Cho K-H, Priya S. Direct and converse effect in magnetoelectric laminate composites. *Appl. Phys. Lett.*, 2011, 98(23):232904.
 7. Nan C-W, Bichurin MI, Dong S, Viehland D, Srinivasan G. Multiferroic magnetoelectric composites: Historical perspective, status, and future directions. *J. Appl. Phys.*, 2008, 103(3):031101.
 8. Geng LD, Yan Y, Priya S, Wang YU. Computational study of cobalt-modified nickel-ferrite/PZT magnetoelectric composites for voltage tunable inductor applications. *Acta Materialia*, 2019, 166:493-502.
 9. Lou J, Reed D, Liu M and Sun NX. Electrostatically tunable magnetoelectric inductors with large inductance tunability. *Appl. Phys. Lett.*, 2009, 94:112508.
 10. Yan Y, Geng LD, Tan Y, Ma J, Zhang L, Sanghadasa M, Nga K, Ghost AW, Wang YU, Priya S. Colossal tunability in high frequency magnetoelectric voltage tunable inductors. *Nature comm.*, 2018, 9:4998.
 11. Yan Y, Geng LD, Zhang L, Tu C, Sriramdas R, Liu H, Li X, Sanghadasa M, Ngo K, Wang YU, Priya S. High power magnetoelectric voltage tunable inductors. *IEEE Trans on Industrial Electronics*, 2020, 1-1.
 12. Zhang J, Chen D, Filippov DA, Li K, Zhang Q, Jiang L, Zhu W, Cao L and Srinivasan G. Bidirectional tunable ferrite-piezoelectric trilayer magnetoelectric inductors. *Appl. Phys. Lett.*, 2018, 113:113502.
 13. Spano ML, Hathaway KB & Savage HT. Magnetostriction and magnetic-anisotropy of annealed Metglas 2605 alloys via DC M-H loop measurements under stress. *J. Appl. Phys.*, 1982, 53:2667-2669.
 14. Yan Y, Geng LD, Zhang L, Gao X, Gollapudi S, Song HC, Dong S, Sanghadasa M, Ngo K, Wang YU, Priya S. Correlation between tenability and anisotropy in magnetoelectric voltage tunable inductor (VTI) *Scientific Rep.*, 2017, 7:16008.
 15. Osborn JA. Demagnetizing factors of general ellipsoid. *Phys. Rev.*, 1945, 67:1351-1357.
 16. Chen DX, Pardo E, Sanchez A. Demagnetizing factors for rectangular prisms. *IEEE Trans. Magnetics*, 2006, 41:2077-2088.
 17. Dong S, Li JF, Viehland D, Cross LE. A strong magnetoelectric voltage gain effect in magnetostrictive-piezoelectric composite. *Appl. Phys. Lett.*, 2004, 85:3534-3536.
 18. Dong S, Li JF, Viehland D. Voltage gain effect in a ring-type magnetoelectric laminate. *Appl. Phys. Lett.*, 2004, 84:4188-4190.
 19. Dong S, Zhai J, Priya S, Li J-F, Viehland D. Tunable features of magnetoelectric transformers. *IEEE Trans on Ultrasonics, Ferroelectrics and Freq. Control*, 2009, 56:1124-1127.
 20. Leung CM, Or SW, Wang F, Ho SL. Dual resonance converse magnetoelectric and voltage step-up effects in laminated composite of long-type PMN piezoelectric single-crystal transformer and Terfenol magnetostrictive alloy bars. *J. Appl. Phys.*, 2011, 109:104103.
 21. Filippov DA, Galkina TA, Laletin VM, Srinivasan G. Voltage transformer based on inverse magnetoelectric effect. *Tech. Phys. Lett.*, 2012, 38:93-95.
 22. Wang H, Qu L, Qiao W. Adjustable-voltage-ratio magneto-electric transformer. *IEEE Magnetic Letters*, 2015, 6:6000104.
 23. Liu YH, Wan JG, Liu J-M, Nan CW. Effect of magnetic bias field on magnetoelectric coupling in magnetoelectric composites. *J. Appl. Phys.*, 2003, 94:5118-5122.
 24. Fetisov YK, Fetisov LY, Srinivasan G. Influence of bias electric field on magnetoelectric interactions in ferromagnetic-piezoelectric layered structures. *Appl. Phys. Lett.*, 2009, 94:132507.
 25. Leung CM, Zhuang X, Xu J, Li J, Srinivasan G, Viehland D. Importance of composite parameters in enhanced power conversion efficiency of Terfenol D/PZT magnetoelectric gyrators. *Appl. Phys. Lett.*, 2017, 110:112904.
 26. Saveliev D, Chashin D, Fetisov L, Shamonin M, Fetisov Y. Ceramic-heterostructure-based magnetoelectric voltage transformer with an adjustable transformation ratio. *Materials*, 2020, 13(18):3981.

DOI: 10.17725/rensit.2021.13.039

Synthesis and study of composite based on porous anodic alumina modified by silver nanowires

Mikhail Yu. Vasilkov, Ilya N. Mikhailov, Alexander E. Isaev, Igor D. Kosobudskii, Nikolai M. Ushakov

Kotelnikov IRE RAS, Saratov Branch, <http://www.cplire.ru/rus/sfire/>
Saratov 410019, Russian Federation

E-mail: vasilkov@mail.ru, mikhailov@mail.ru, isaev@mail.ru, kosobudsky@mail.ru, mmmu@bk.ru

David Z. Safoshkin

Yu.A. Gagarin Saratov State Technical University, <http://www.sstu.ru/>
Saratov 410054, Russian Federation

E-mail: safoshkin@mail.ru

Received February 20, 2021, peer-reviewed February 26, 2021, accepted February 28, 2021

Abstract: The paper presents the results of an experimental study of the deposition of modified silver into the pores of ceramic Ag&Al₂O₃ membranes, laboratory samples of thin nanocomposite membranes were obtained based on the developed technological methods of silver deposition, and their composition and surface morphology were studied.

Keywords: nanopores, aluminium oxide, silver, electrochemical synthesis

UDC 544.66

Acknowledgments: The work was performed within the framework of the state assignment "Sensor".

For citation: Mikhail Yu., Ilya N. Mikhailov, Alexander E. Isaev, David Z. Safoshkin, Igor D. Kosobudskii, Nikolai M. Ushakov. Synthesis and study of composite based on porous anodic alumina modified by silver nanowires. *RENSIT*, 2021, 13(1)39-44. DOI: 10.17725/rensit.2021.13.039.

CONTENTS

- 1. INTRODUCTION (39)
- 2. MATERIALS AND METHODS (40)
- 3. RESULTS AND DISCUSSION (42)
- 4. CONCLUSION (43)
- REFERENCES (43)

1. INTRODUCTION

To identify active sites and surface intermediates in catalytic reactions [1,2], many methods are used, such as signal enhancement Raman spectroscopy on the surface of samples (SERS) [3], X-ray photoelectron spectroscopy (XPS) [4], infrared (IR) spectroscopy [5,6]. Among them, SERS, which uses optically excited coherent oscillations of conduction electrons on a developed (rough or porous) metal surface to dramatically amplify the Raman signals of absorbed molecules, is a unique spectroscopic detection method that offers information on both surface-sensitive and chemical bonding,

and it is ideal for direct detection of surface chemical intermediates. For direct detection of intermediate products of surface reactions during photocatalysis, nanocrystalline SERS substrates with a large area with a uniform and strong amplification of the electromagnetic field are required. In [7], it was demonstrated that using the Langmuir-Blodgett method, it is possible to collect faceted Ag nanocrystals with sharp corners into a close-packed substrate of a large area with gaps between particles less than a nanometer in size, which have a gain of up to 10⁸ and are optically homogeneous for performing quantitative ultrasensitive determination arsenic with a detection limit of ~ 1 ppb. In [8], it is reported that membranes with a surface cubic morphology of silver, in which silver nanocubes with sharp edges and corners serve as "hot spots", made it possible to increase the sensitivity of the spectral method by amplifying the signal by 5 orders of magnitude.

To obtain optically transparent membranes with a developed metallized surface, the method of electrochemical anodic oxidation of metal surfaces is known as one of the simple and effective technological methods. The manufacture of porous membranes based on anodic alumina (PAOA) is based on simple and inexpensive electrochemical anodization, combined with the self-ordering process of nanopores that does not require lithography or templates, with the ability to control the process of obtaining ideally ordered and size-controlled nanopores with the required geometry [9].

The electronic structure of aluminum oxide (Al_2O_3) is of increasing interest due to its various applications in optical, electronic, and structural devices. Thus, thin optically transparent ceramic metallized membranes based on porous anodic alumina can serve as a platform for various optical and electronic applications.

The aim of this work was to experimentally study the process of modified deposition of silver into the nanopores of ceramic membranes, to manufacture thin nanocomposite membranes based on the developed technological methods

for silver deposition, and to study their composition and surface morphology.

2. MATERIALS AND METHODS

The technological scheme for obtaining a composite material based on a matrix of porous anodic aluminum oxide (PAOA) filled with silver nanowires is shown in Fig. 1. The starting material for obtaining the composite was Al (99.9%) in the form of a foil $\sim 100 \mu\text{m}$ thick. To prepare the metal and structure its surface for the further formation of an ordered system of porous channels, the primary anodic oxidation of aluminum was carried out. The process was carried out in a 0.3 M solution of $\text{H}_2\text{C}_2\text{O}_4$ in an electrochemical cell made of an inert material at a temperature of 2-4°C in a two-electrode mode. A working sample made of aluminum was connected to the positive pole of the current source (anode), and a steel perforated electrode of equal area was connected to the negative pole (cathode). A constant voltage in the range of 40 ± 1 V was applied to the electrodes, the distance between which was 10-15 mm, and held for 15-20 hours. The thin layer of Al_2O_3 obtained after primary anodizing on the metal surface had a disordered porous structure ("sacrificial

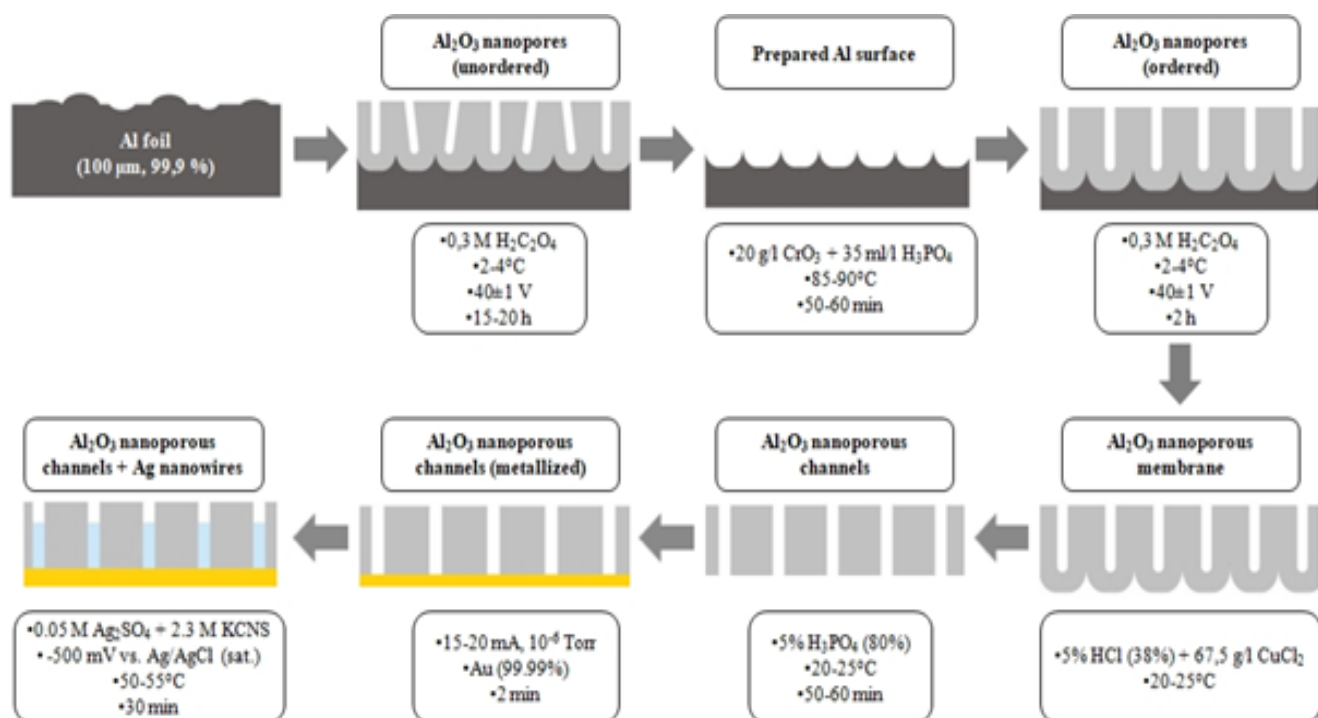


Fig. 1. Technological scheme for obtaining a composite based on a matrix of PAOA filled with Ag nanowires.

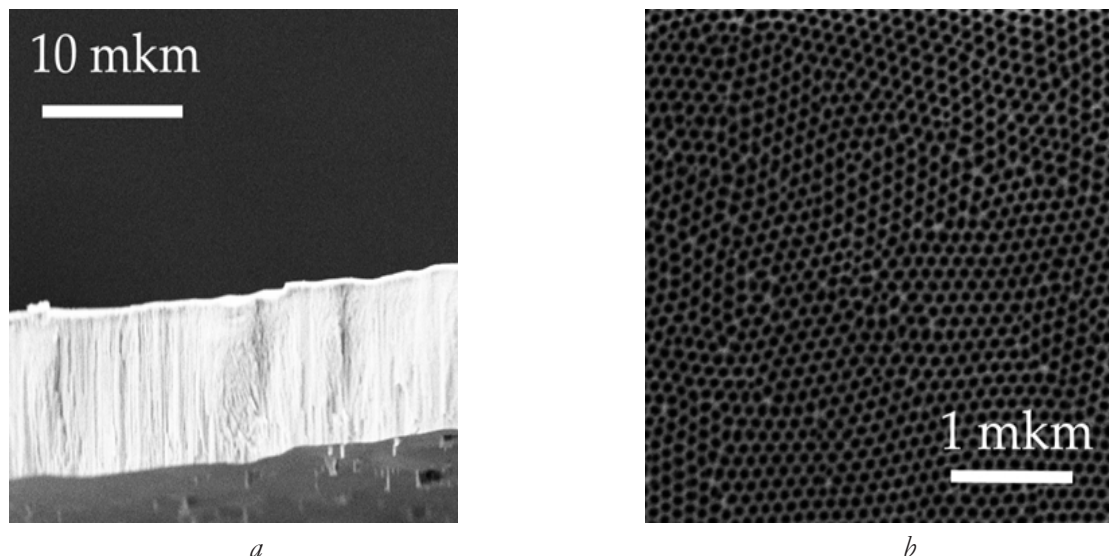


Fig. 2. Micrographs of scanning electron microscopy of the PAOA membrane: a) - side view (inset - external view of the working sample), b) - top view (porous layer).

layer") and was removed at 85–90°C by chemical etching in a solution of CrO_3 and H_3PO_4 (80%) with a concentration of 20 g/L and 35 ml/L, respectively. The metal thus prepared underwent a second anodization for 2 h under conditions similar to the primary anodic oxidation, as a result of which an ordered porous structure of Al_2O_3 was formed on the Al surface.

To make the PAOA sample optical transparency, the metal sublayer at room temperature was dissolved in a mixture of 5 wt% HCl (38%) with the addition of 67.5 g/L CuCl_2 . The result was thin PAOA membranes (**Fig. 2a**), one side of which was covered with a continuous layer of Al_2O_3 (barrier layer), while the other had an "open" porous structure (porous layer, **Fig. 2b**). To form a matrix of hollow channels, a continuous oxide layer was dissolved in 5% H_3PO_4 (80%), after which a thin Au layer with a thickness of less than 10 nm was deposited on one side of the membrane by plasma spraying, which served as a conductive contact at the bottom of the pores. At the final stage of the technological scheme, the PAOA membrane was functionalized with silver by electrochemical deposition. Ag electrodeposition was carried out at $50 \pm 5^\circ\text{C}$ in a potentiostatic mode at a potential of -450 mV (rel. Ag/AgCl (sat.)) (With a graphite auxiliary

electrode, $S \sim 5 \text{ cm}^2$) from a mixture of 0.05M Ag_2SO_4 + 2.3M KCNS for different times. Upon completion of the technological scheme, the obtained samples were washed with distilled water and dried in air at room temperature. Ag electrodeposition was carried out at $50 \pm 5^\circ\text{C}$ in a potentiostatic mode at a potential of -450 mV with a graphite auxiliary electrode, $S \sim 5 \text{ cm}^2$ from a mixture of 0.05M Ag_2SO_4 + 2.3M KCNS for different times. Upon completion of the technological scheme, the obtained samples were washed with distilled water and dried in air at room temperature.

3. RESULTS AND DISCUSSION

The surface morphology and structure of the obtained composites based on porous anodic Al_2O_3 modified with Ag were studied by scanning electron microscopy (SEM) at the AURIGA Crossbeam 350 workstation (Carl Zeiss Gr., Germany). As mentioned above, the surface of PAOA membranes had a highly ordered two-dimensional structure in the form of hexagonally located pores with a diameter of (52.9 ± 2.7) nm (**Fig. 2b**), a height of $\sim 10 \mu\text{m}$ with a packing density of $1.1 \cdot 10^{10} \text{ cm}^{-2}$. There were practically no artifacts and defective areas on the surface. The porous channels were oriented mutually parallel in a direction perpendicular to the original substrate (**Fig. 2a**).

After the deposition of silver on the surface of the composite, there was observed the appearance of spherical agglomerates ranging in size from 0.1 to 1.0 μm , which were "caps" of silver, obtained as a result of the release of metal from the porous channel to the surface of the membrane (**Fig. 3a**). It should be noted that the "caps" were formed rather scattered and with a low surface density. This can be explained by the high filling rate of single pores due to a kind of electrical "breakdown", which leads to the rapid deposition of silver in these channels. Most of the pores do not have metal "caps", since their filling with metal occurs evenly, and it takes a longer time to completely fill. As an example, Fig. 3a shows a cross section for a PAOA-based composite modified by Ag deposition for 30 min. It can be seen that for a given deposition time interval, the length of the Ag filaments is about half the length of the porous channel ($\sim 5 \mu\text{m}$). The filaments have a dense, continuous structure, almost equal in length and a diameter corresponding to the pore diameter. The complete filling of the nanopores occurred with the periodic removal of a compact metal Ag layer from the surface of the PAOA membrane and the process time was about 60 min.

The qualitative composition of the obtained PAOA/Ag composites was studied by X-ray phase analysis (XPA) using an ARL X'TRA X-ray diffractometer (0.154 nm, CuK α , Thermo Scientific, Switzerland). The diffraction pattern

of the composite synthesized at 30 min of Ag deposition (Fig. 3b) showed a diffraction doublet of high intensity (44.6° , 44.9°), related to the α -phase of Al_2O_3 , and a diffuse halo (43.5°) for aluminum oxide with an amorphous structure, from which it follows that the synthesized PAOA membrane had various structural modifications. The characteristic reflections at 24.7° and 38.2° were attributed to the α -phase of metallic Ag, while their low intensity indicated a low metal concentration. The average crystallite size, found according to P. Scherrer's formula ($K \approx 1$), for $\alpha\text{-Al}_2\text{O}_3$ and $\alpha\text{-Ag}$ was 15.9 nm and (11.3–23.4) nm, respectively. Thus, the synthesized composite material was an ordered porous matrix of mixed Al_2O_3 with a predominance of the crystalline α -phase, the inner cavity of which was filled with metallic $\alpha\text{-Ag}$.

When analyzing the current-time dependences of silver deposition, it was found that the deposition curves had characteristic regions corresponding to certain stages of the PAOA modification process (Fig. 3c). At the initial moment of time (0–8 min), a slight increase in the cathodic current was observed, which was associated with the occurrence of silver nucleation processes at the bottom of the pores. After the formation of Ag nuclei, the internal cavity of the nanoporous channel was gradually filled in the vertical direction, which manifested itself in the current – time dependence in an increase in the growth rate of the deposition

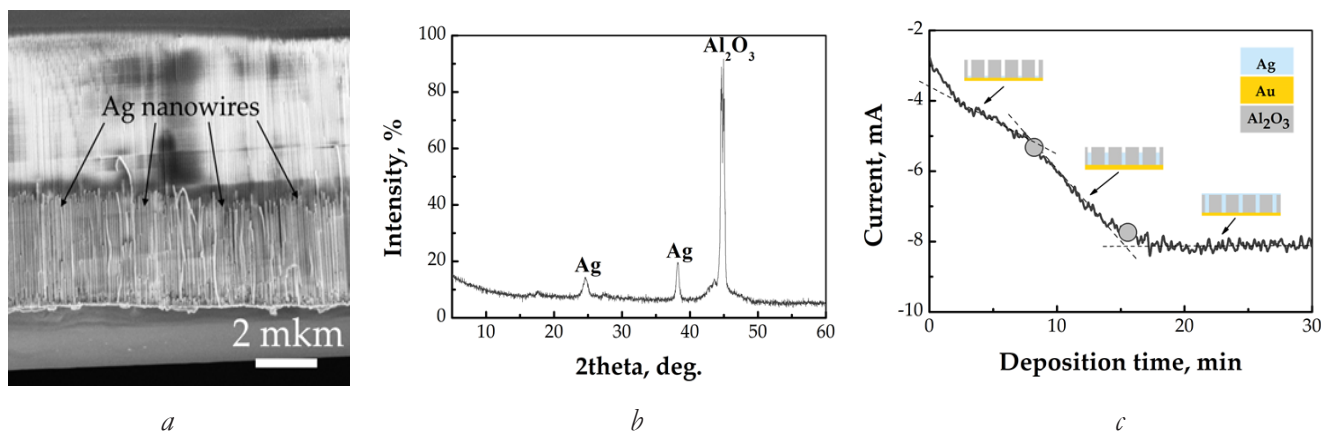


Fig. 3. Cross-sectional SEM micrograph (a) and X-ray diffractogram (b) of the composite based on Ag-modified PAOA (top view in the inset). Time dependence of the cathode current during the deposition of silver into the PAOA matrix (c).

current. After 16 min of the process, the cathodic current changed insignificantly, which indicated the formation and evolution of a continuous Ag layer on the membrane surface due to the unification of metal "caps". No further changes were recorded in the deposition curve. It can be concluded that by varying the time of the process and a qualitative analysis of the dependences of the deposition current on time, it is possible to obtain composites based on PAOA with different degrees of pore filling with metallic silver.

4. CONCLUSION

Laboratory samples of thin ceramic composite PAOA nanomembranes on the basis of the developed technological procedure for the creation of composite nanomaterials from nanoporous anodic aluminum oxide filled with silver nanowires were prepared. The surface of the PAOA membranes had a highly ordered two-dimensional structure in the form of hexagonal pores with a diameter of (52.9 ± 2.7) nm, a height of ~ 10 μm with a packing density of $1.1 \cdot 10^{10}$ cm^{-2} . At the same time, there were practically no defect areas on the surface.

It is shown that the process of modified deposition of silver into the pores of membranes has a two-stage character. At the first stage of silver deposition on the surface of the composite, the appearance of scattered spherical agglomerates with a size of 0.1 to 1.0 μm with a low surface density, obtained as a result of the exit of metal from the porous channel to the membrane surface was observed. The appearance of silver agglomerates can be explained by the high rate of filling of single pores due to a kind of electrical "breakdown", which leads to a rapid deposition of silver in these channels. At the second, final stage, there is a uniform volumetric filling of the pores with PAOA. Within 30 min, the length of the Ag filaments is about half the length of the porous channel (~ 5 μm). The filaments have a dense, continuous structure, almost equal in length and a diameter corresponding to the pore diameter.

The complete filling of the nanopores occurred with the periodic removal of a compact metal Ag layer from the surface of the PAOA membrane and the process time was about 60 min.

X-ray diffraction analysis showed that the synthesized composite material was an ordered porous matrix of mixed Al_2O_3 with a predominance of crystalline α -phase, the inner cavity of which was filled with metallic α -Ag. The average crystallite size for α - Al_2O_3 and α -Ag was 15.9 nm and (11.3-23.4) nm, respectively. It can be concluded that by varying the time of the process and a qualitative analysis of the dependences of the deposition current on time, it is possible to obtain composites based on PAOA with different degrees of pore filling with metallic silver.

The developed nanoceramic porous silver modified membranes can become the basic platform for the construction of various sensor devices.

REFERENCES

1. Wang Y, Wöll C. Chemical reactions on metal oxide surfaces investigated by vibrational spectroscopy. *Surface Science*, 2009, 603:1589-1599.
2. Fan F, Feng Z, Li C. UV Raman Spectroscopic Studies on Active Sites and Synthesis Mechanisms of Transition Metal-Containing Microporous and Mesoporous Materials. *Acc. Chem. Res.*, 2009, 43:378-387.
3. Heck KN, Janesko BG, Scuseria GE, Halas NJ, Wong MS. Observing Metal-Catalyzed Chemical Reactions in Situ Using Surface-Enhanced Raman Spectroscopy on Pd-Au Nanoshells. *J. Am. Chem. Soc.*, 2008, 130:16592-16600.
4. Grass ME, Zhang Y, Butcher DR et al. A Reactive Oxide Overlayer on Rhodium Nanoparticles during CO Oxidation and Its Size Dependence Studied by In Situ Ambient-Pressure X-ray Photoelectron Spectroscopy. *Angew. Chem. Int. Ed.*, 2008, 47:8893-8896.

5. Chen T, Feng Z, Wu G et al. Mechanistic Studies of Photocatalytic Reaction of Methanol for Hydrogen Production on Pt/TiO₂ by in situ Fourier Transform IR and Time-Resolved IR Spectroscopy. *J. Phys. Chem. C*, 2007, 111:8005-8014.
6. Brownson JRS, Tejedor-Tejedor MI, Anderson MA. FTIR Spectroscopy of Alcohol and Formate Interactions with Mesoporous TiO₂ Surfaces. *J. Phys. Chem. B*, 2006, 110:12494-12499.
7. Mulvihill M, Tao A, Benjauthrit K, Arnold J, Yang P. Surface-Enhanced Raman Spectroscopy for Trace Arsenic Detection in Contaminated Water. *Angew. Chem. Int. Ed.*, 2008, 47:6456-6460.
8. Henzie J, Andrews SC, Ling XY et al. Oriented assembly of polyhedral plasmonic nanoparticle clusters. *Proc Natl Acad Sci USA*, 2013, 110:6640-6645.
9. Jani AMMd, Losic D, Voelcker NH. Nanoporous anodic aluminium oxide: Advances in surface engineering and emerging applications. *Progress in Materials Science*, 2013, 636-704, <http://dx.doi.org/10.1016/j.pmatsci.2013.01.002>.

DOI: 10.17725/rensit.2021.13.045

LENR as a manifestation of weak nuclear interactions. New approach to creating LENR reactors

Alexander G. Parkhomov

R & D laboratory K.I.T., <https://reabiz.ru/>

Moscow 121108, Russian Federation

E-mail: alexparb@mail.ru

Roman V. Karabanov

Research center SYNTHESTECH, <https://synthesit.ru/>

Sochi 354002, Russian Federation

E-mail: info@synthetech.com

Received February 06, 2021, peer-reviewed February 19, 2021, accepted February 26, 2021

Abstract: Hypothesis is suggested about the generation of neutrino-antineutrino pairs in collisions of particles of matter at temperatures of several thousand degrees. Particularly intense generation should occur in metals and dense plasma. Resulting neutrinos and antineutrinos can excite exothermic nuclear reactions in the surrounding matter. A number of experiments were carried out that confirmed the energy release predicted by the hypothesis in a substance near a metal heated to a high temperature. The source of the neutrino-antineutrino (hot metal or dense plasma) can be separated from the "fuel" - the substance where nuclear transformations occur. This opens up the possibility for designing highly efficient LENR reactors. Several reactors based on this approach have been tested. In all reactors, at a sufficiently high temperature of the metal core, heat was detected in excess of the electricity consumed. A number of experiments indicate that the participation of hydrogen in nuclear transmutations is optional.

Keywords: hot metals, dense plasma, neutrino, collisions, nuclear transmutations, LENR, incandescent lamps, LED, calorimetry

UDC 53.043

Fot citation: Alexander G. Parkhomov, Roman V. Karabanov. LENR as a manifestation of weak nuclear interactions.. New approach to creating LENR reactors. *RENSIT*, 2021, 13(1):45-58. DOI: 10.17725/rensit.2021.13.045.

CONTENTS

1. INTRODUCTION (46)
2. INTERACTION OF LOW-ENERGY NEUTRINOS WITH COLLECTIVES OF ATOMS. VARIETY OF POSSIBLE TRANSFORMATIONS (46)
3. EXPERIMENTS SUPPORTING THE HYPOTHESIS OF THE ROLE OF NEUTRINOS IN COLD NUCLEAR TRANSMUTATIONS (49)
 - 3.1. EXPERIMENTS 1. MEASUREMENT OF HEAT OUTPUT POWER USING AN AIR FLOW CALORIMETER (50)
 - 3.2. EXPERIMENTS 2. MEASUREMENT OF HEAT GENERATION POWER BY THE RATE OF TEMPERATURE INCREASE IN WATER (50)

4. INVESTIGATION OF ELEMENTAL AND ISOTOPIC CHANGES IN MATTER NEAR INCANDESCENT LAMPS (51)
 - 4.1. EXPERIMENT 3. A HALOGEN INCANDESCENT LAMP AND A CIRCULATING SOLUTION (52)
 - 4.2. EXPERIMENT 4. HALOGEN INCANDESCENT LAMP AND TIN-LEAD ALLOY (53)
 - 4.3. EXPERIMENT 5. HALOGEN INCANDESCENT LAMP AND BOILING SOLUTION (54)
 - 4.4. EXPERIMENTS 6. HOT METAL OR LIGHT? (55)
5. NEW APPROACH TO CREATING LENR REACTORS (56)
6. CONCLUSION (57)
- REFERENCES (57)

1. INTRODUCTION

Researches in the field called LENR (low-energy nuclear reactions, cold nuclear transmutations, cold nuclear fusion) have shown the diversity of this phenomenon. These are processes in metals with hydrogen dissolved in them [1,2]. These are processes in plasma [3,4], in gas discharge [5], in electrolysis [6], and even in biological systems [7,8]. In addition to energy release, which far exceeds the capabilities of chemical reactions, LENR is characterized by a large variety of emerging chemical elements. For example, after water treatment in the Energoniva reactor [3], Li, Be, B, C, Mg, Si, P, Ca, Ti, V, Cr, Mn, Fe, Ni, Cu, Sn, Se, Pb, Bi were detected. In the nickel-hydrogen LENR reactor, which worked for 7 months [2], Ca, V, Ti, Mn, Fe, Co, Cu, Zn, Ga, Ba, Sr, Yb, and Hf were found. Initially, the content of these elements in the "fuel" and structural materials was negligible. An overview of elemental and isotopic changes in nickel-hydrogen LENR reactors is provided in the article [1].

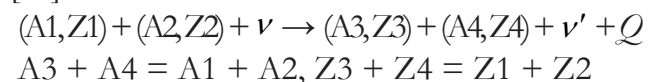
Huge variety of chemical elements can be explained by nuclear transformations in nuclide collectives initiated by low-energy neutrinos (antineutrinos) [9,10].

2. INTERACTION OF LOW-ENERGY NEUTRINOS WITH COLLECTIVES OF ATOMS. VARIETY OF POSSIBLE TRANSFORMATIONS

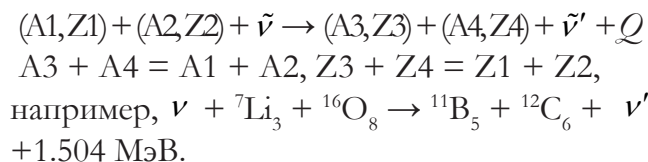
De Broglie wavelength $\lambda = h/p$ (h is Planck's constant, p is the momentum) characterizes the size of the interaction region. Neutrinos (antineutrinos) with an energy of about 1 MeV, which occur in nuclear reactions, have $\lambda \sim 10^{-12}$ m. Distance between the atoms in a liquid or solid substance is $\sim 10^{-10}$ m, i.e. the possibility of nuclear transformations under the action of such neutrinos does not go beyond one atom. At a sufficiently low energy, value λ exceeds the distance between the atoms, and the interaction can cover many atoms. For example, a neutrino with a mass of 0.28 eV with a kinetic energy of

0.2 eV (average energy of thermal motion at a temperature of about 2000°C) is $\sim 3.2 \cdot 10^{-6}$ m, i.e., much larger than the interatomic distance. Nuclear transformations become possible, in which two or more atoms are transformed into two or more other atoms, and electrons can be included in these transformations. In this case, the laws of conservation of the baryon charge (i.e., the number of nucleons), electric and lepton charges must be fulfilled. Since neutrinos at low energies cannot make a significant contribution to the energy of the reaction, only transformations with a positive energy balance can occur. Law of conservation of momentum defines the distribution of reaction products by the velocities and angles of expansion.

Transformations without participation of electrons can be written in the form of equations [11]:



или



Neutrino (antineutrino) on the left side of the equations must have a sufficiently low energy so that the de Broglie wavelength (the interaction region) is greater than the distance between the reacting atoms. Neutrino (antineutrino) in the right part acquires a significant part of the energy Q and freely carries it away, reducing the amount of energy given by the emerging nuclei to the environment.

For transformations involving two nuclei involving electrons, the following processes are possible [12]:

- *Rearrangement of nucleons*

$$(A_1, Z_1) + (A_2, Z_2) + e + \tilde{\nu} \rightarrow (A_3, Z_3) + (A_4, Z_4) + Q \\ A_3 + A_4 = A_1 + A_2, Z_3 + Z_4 = Z_1 + Z_2 - 1,$$
 for example, ${}^{60}\text{Ni}_{28} + {}^1\text{H}_1 + e^- + \tilde{\nu} \rightarrow {}^4\text{He}_2 + {}^{57}\text{Fe}_{26} + 0.569 \text{ MeV.}$
- *Rearrangement of nucleons with the release of electrons*

$(A_1, Z_1) + (A_2, Z_2) + \nu \rightarrow (A_3, Z_3) + (A_4, Z_4) + e^- + Q$
 $A_3 + A_4 = A_1 + A_2, Z_3 + Z_4 = Z_1 + Z_2 + 1,$
 for example, $^{61}\text{Ni}_{28} + ^{64}\text{Ni}_{28} + \nu \rightarrow ^{63}\text{Cu}_{29} + ^{62}\text{Ni}_{28} + e^- + 0.995 \text{ MeV}$.

Computer calculation of possible transformations of two stable nuclides into two other stable nuclides without and with the participation of electrons is made [11,12]. The abundance of such transformations is striking. More than a million variants have been identified. The results obtained can be taken from the author of this article in the form of an EXCEL file.

It suggests that the abundance of emerging chemical elements in LENR processes is of the same nature. But everyone knows about the extremely weak intensity of the interaction of neutrinos with matter. Therefore, for the appearance of tangible effects, neutrino fluxes of enormous magnitude are needed. Where can they come from in a LENR reactor? From Outer Space? According to [13, 14], the density of the galactic neutrino flux is about $10^7 \text{ cm}^{-2}\text{s}^{-1}$. This is clearly not enough to initiate the kilowatt power processes achieved in a number of LENR reactors.

To find a possible source of intense neutron fluxes, we pay attention to one characteristic feature of LENR processes: they have quite a noticeable energy threshold. This is especially clearly seen in the case of nickel-hydrogen reactors, where excessive heat release is detected only at temperatures above 1200°C [1,2], i.e. when average energy of the matter particles during thermal motion exceeds 0.1 eV. In electroplasma reactors [3,4], temperature reaches several thousand degrees (tenths of eV). In installations with a glow gas discharge plasma [5], electron energy is of the order of 1 eV. At first glance, the processes in which LENR features are detected at room temperature (electrolysis [6], biology [7,8]) are an exception to this rule. But in fact, for acts of energy exchange, both in electrochemistry and in the processes of cellular

metabolism, it is the energy of the order of 1 eV that is characteristic.

Neutrino has a very small mass (currently it is believed that the mass of the electron neutrino and antineutrino does not exceed 0.28 eV [15]), so they can be formed as a result of inelastic collisions of matter particles (electrons, ions, neutral atoms) during their thermal motion. Since there are no exact data on the mass of neutrinos, we will assume that the minimum energy for the formation of a neutrino-antineutrino pair is 0.5 eV. Average energy of 0.5 eV has particles in a body heated to 3200°C . Recall that average energy of thermal motion $\bar{\varepsilon} = 1.5kT$ ($k = 1.38 \cdot 10^{-23} \text{ J/K}$ is the Boltzmann constant, T is the absolute temperature). Some particles have the same and higher energy at a lower temperature. Using the particle energy distribution function in thermal motion [16]

$$f(\varepsilon) = \frac{2\sqrt{\varepsilon}}{\sqrt{\pi(kT)^3}} \exp\left(-\frac{\varepsilon}{kT}\right),$$

it is possible to find the dependence on the temperature of the fraction of particles having an energy higher than the specified one. For an energy of 0.5 eV, this dependence is shown in **Fig. 1**. At room temperature, the fraction of such particles is 10^{-8} . A noticeable fraction of particles with an energy higher than 0.5 eV appears only at a temperature of about 1000°C . At a temperature of 1600°C , such particles are already 10%, and at a temperature of 4500°C , 50%. Therefore, when you made assumptions threshold thermal generation of neutrino-antineutrino pairs of about 1000°C .

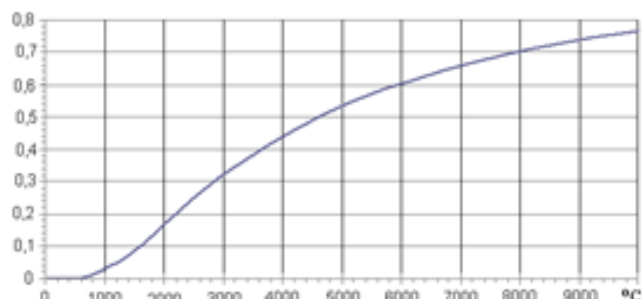


Fig. 1. Fraction of particles having an energy above 0.5 eV, depending on the temperature.

At present, the level of knowledge about the properties of neutrinos is insufficient to reliably determine the probability of the formation of neutrinos and antineutrinos in thermal collisions of matter particles. It is only clear that the probability of this is small. A small probability is compensated by a large number of collisions. Let's estimate the number of collisions per second during thermal motion in metals. Most often in metals, electrons collide with atoms. The length of the run between collisions is about 10^{-8} m. The velocity of the electrons at a temperature of 2000K is about $2 \cdot 10^5$ m/s [17, p.117]. Consequently, the electron under its thermal motion experiences $2 \cdot 10^{13}$ collisions per second. Given that the number of free electrons in 1 cm^3 of metal is about 10^{23} [17, p.115], we find the number of collisions per second in 1 cm^3 of metal: $2 \cdot 10^{36}$.

Such a huge number of collisions suggests that neutrinos and antineutrinos arise in hot metals with an intensity sufficient to initiate nuclear transformations that give significant energy release even with very small probabilities of processes associated with neutrinos. Let's assume that only one of the 10^{10} collisions generates a neutrino-antineutrino pair, and only one of the 10^{10} neutrinos or antineutrinos causes a nuclear transformation. Even with such huge losses, 1cm^3 of hot metal produces $2 \cdot 10^{16}$ nuclear transformations per second. In each act of such transformations, about 1MeV is allocated. Since 1 J is equivalent to $6.25 \cdot 10^{12}$ MeV, the power of the released energy is approximately 2 kW.

We will make a similar estimate for a gas heated to a temperature sufficient for thermal generation of neutrinos (several thousands °C). In a gas, even at such temperatures, there are significantly fewer electrons and ions than neutral atoms (molecules), so it is mainly atoms (molecules) that collide. The speed of their movement is about 10^3 m/s, and the length of the run before the collision at atmospheric pressure is about 10^{-7} m [18]. Hence, an atom (molecule) experiences about 10^{10} collisions per

second. 1 cm^3 of hot gas at atmospheric pressure contains about 10^{19} atoms (molecules). It has about 10^{29} collisions per second, which is 7 orders of magnitude less than in metals. Thus, in a gas heated to a temperature of several thousands degrees, the thermal generation of neutrinos and antineutrinos, although possible, occurs with an intensity many orders of magnitude lower than in metals.

For intensive generation of neutrinos and antineutrinos, a hot, dense medium with a high content of free electrons is needed. In addition to metals, such a medium is high-density plasma, which occurs briefly, for example, during explosions of metal conductors or with a sufficiently strong pulsed energy release in liquids.

Thus, the assumption of the possibility of nuclear transmutations under the action of low-energy neutrinos arising in hot metals or dense plasma allows us to explain two empirically discovered properties of LENR: the variety of chemical elements that arise and the temperature threshold of the order of 1000°C. One can also understand the absence of hard nuclear radiation. In the proposed mechanism, rearrangement of nucleons occurs without introducing energy that could cause the excitation of nuclear levels, which could lead to the emission of gamma quanta. Lack of energy input leads to the fact that out of all possible variants of transformations, those are realized in which the most stable nuclides are formed, which are not prone to either alpha or beta radioactivity, or to emission of neutrons. Released energy is realized in the form of the kinetic energy of the resulting nuclides. Despite the fact that they can have an energy of up to several MeV, when they are decelerated, hard radiation does not occur, since massive charged particles, even at high energies, lose their energy mainly as a result of ionization and excitation of the atoms of the medium in which they move [19]. At the same time, electromagnetic radiation is emitted, but "soft", with the energy of quanta up to several

keV. In addition, the radiation of "soft" quanta occurs when the deformed electron shells of the resulting nuclides are normalized. This allows us to explain the appearance of soft X-rays near the operating LENR installations.

Note that in weak nuclear interactions (beta processes) involving neutrinos (antineutrinos), there is no "Coulomb barrier problem", which for a long time was the justification for the "impossibility" of cold nuclear transmutations.

3. EXPERIMENTS SUPPORTING THE HYPOTHESIS OF THE ROLE OF NEUTRINOS IN COLD NUCLEAR TRANSMUTATIONS

Above hypothesis predicts that a metal heated to a temperature of about 1000°C or higher emits neutrinos and antineutrinos, which cause the appearance of initially absent chemical elements in the surrounding matter. This is accompanied by release of heat. Let us consider several confirmatory experiments reported at the 26th Russian Conference on Cold Nuclei Transmutations and Ball Lightning [20].

In the experiments described below, tungsten filament was used as hot metal in incandescent lamps, in particular, in halogen lamps with a tubular quartz shell with a nominal power of 150 or 300 W (**Fig. 2**), as well as in a conventional incandescent lamp with a power of 40 W. To reduce the power consumption, at which a sufficiently high temperature of the filament is achieved, you can use a reflective coating of the lamp cylinder. Such a coating of aluminum foil had a lamp with a power of 40 watts.

Dependence of the specific resistance of tungsten on temperature is well known [21].



Fig. 2. Halogen incandescent lamp and 40W incandescent lamp wrapped in aluminum foil.

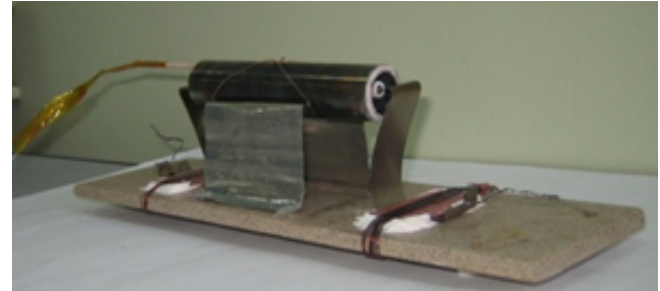


Fig. 3. Halogen incandescent lamp inside a cylindrical container.

Therefore, the temperature of the tungsten filament is easy to determine by measuring its resistance at room temperature R_{20} , as well as the voltage U and current I in the operating mode. Knowing the voltage and current, we determine the resistance $R = U/I$, and then the temperature by the formula $t(^{\circ}\text{C}) = 197.6(R/R_{20}) - 1.57(R/R_{20})^2 - 176$. It should be noted that the described method of determining the temperature gives an average value, since the filament has colder (at the ends and near the supports) and hotter areas.

Using the same data, you can determine the power consumed by the lamp $P = U \cdot I$.

3.1. EXPERIMENTS 1. MEASUREMENT OF HEAT OUTPUT POWER USING AN AIR FLOW CALORIMETER

The halogen incandescent lamp is placed inside a cylindrical stainless steel container with two walls, the space between which can be filled with various substances (**Fig. 3**). To measure heat output power, air flow calorimeter is used (**Fig. 4**). Heat output power is determined by increasing the temperature of the air washing the object under study, located in a thermally insulated cylinder with a diameter of 20 cm and



Fig. 4. Air flow calorimeter.

a length of 100 cm. The temperature difference between the outlet and inlet air is measured by a differential thermocouple. To create a stable air flow, a fan connected to a stable power source is used. Calibration measurements showed that the measurement error of this calorimeter at a heat output power of 100 to 2000 W does not exceed 3%.

Fig. 5 shows the dependence of the thermal coefficient COP (the ratio of the heat output power to the electrical power consumed) the temperature of the filament in the halogen lamp. The measurements were made with an empty container and with a container filled with lithium tetraborate $\text{Li}_2\text{B}_4\text{O}_7$ (10 g). Excessive heat generation at temperatures above 2200°C is observed even in the case of an empty container, but a container filled with lithium tetraborate gives a stronger effect. With an electrical power consumption of 292 W, the average temperature of the tungsten filament reached 2390°C. Heat output power measured by a flow-through air calorimeter, 428W. Thus, the release of energy in excess of the spent on heating the thread is 136 watts. Further temperature rise leads to an increase in excess power, however, as can be seen from Fig. 5, the thermal coefficient decreases. This is due to the fact that at high temperatures, the power required for heating grows much faster ($\sim T^4$) than the excess heat release, the growth of which is similar to the dependence shown in Fig. 1.

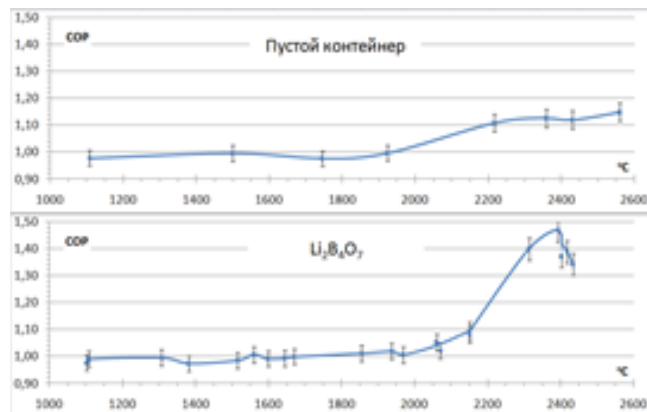


Fig. 5. Thermal coefficient as a function of the filament temperature in halogen lamp, measured with an empty container and a container filled with lithium tetraborate.

Note that this reactor does not contain hydrogen, and, nevertheless, reliably gives excessive heat generation. This indicates the need to reconsider the established view that hydrogen is necessary for the LENR to flow. This conclusion is confirmed by the nuclear transmutations found in the lead-tin alloy that does not contain hydrogen (see the section "Experiment 4. Halogen incandescent lamp and tin-lead alloy").

3.2. EXPERIMENTS 2. MEASUREMENT OF HEAT GENERATION POWER BY THE RATE OF TEMPERATURE INCREASE IN WATER

In these experiments, incandescent lamps were immersed in water (450 ml) poured into a glass Dewar vessel (**Fig. 6**). The heat output was determined by the rate of increase in the water temperature. Calibration experiments have shown that by varying the measurement time, this calorimeter can measure the heat output power in the range of 10-500 W with an error of no more than 1%. To speed up the establishment of thermal equilibrium, a manual stirrer was used.

Several different types of incandescent lamps have been tested. In all experiments, excess heat was detected when the average temperature of the filament exceeded 2200°C. **Fig. 7** shows



Fig. 6. Experimental installation with a water calorimeter. 1 - a Dewar vessel with water in which an incandescent lamp is immersed, 2 - thermometer, 3 - meter of current, voltage and power consumption, 4 - stopwatch, 5 - stirrer.

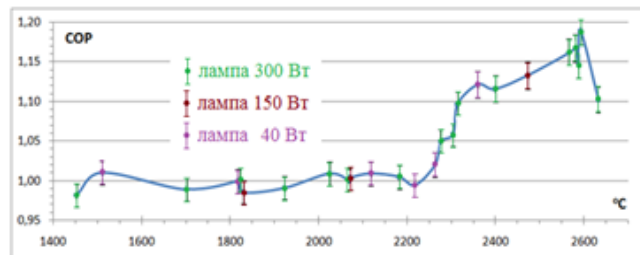
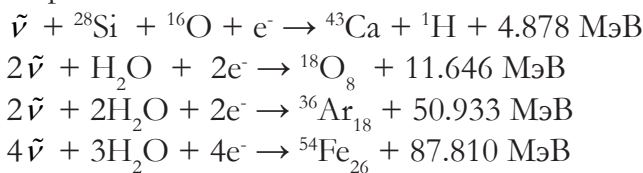


Fig. 7. Dependence of the thermal coefficient COP on the filament temperature. Set of data obtained in different experiments.

a set of data obtained in experiments with an incandescent lamp with a nominal power of 40 W and halogen lamps of a tubular design (Fig. 2) with nominal power of 150 and 300 W. Due to the stronger cooling of the lamp shells with water compared to air, 60-70% higher than the rated power is required to achieve a sufficiently high filament temperature.

Fig. 7 shows that for all the tested lamps, which are very different in power and design, a noticeable increase in the thermal coefficient is observed at temperatures above 2200°C. At a thread temperature of about 2500°C, the thermal coefficient reaches a value of 1.18, but at a higher temperature it decreases. This is due to the fact that at high temperatures, the power required for heating grows much faster than excess heat generation. This effect was also observed in type 1 experiments (see Fig. 5).

Excessive heat generation can occur in lamp cylinders containing SiO₂ and in water. For example, the following nuclear transformations are possible:



To make sure that new chemical elements actually appear in the substance near the incandescent lamps, special rather long-term experiments were carried out, which convincingly confirmed the appearance of nuclides that were initially absent.

4. INVESTIGATION OF ELEMENTAL AND ISOTOPIC CHANGES IN MATTER NEAR INCANDESCENT LAMPS

To confirm above hypothesis about the generation of neutrino-antineutrino pairs in the collision of particles of matter at temperatures of several thousand degrees, it is important to make sure not only that a lot of heat is released in the substance surrounding a hot metal, but also that new chemical elements appear in accordance with nuclear reactions that can be produced by low-energy neutrinos [11,12]. The experiments described above showed the presence of excessive heat release at a sufficiently high metal temperature, but they were not long enough to accumulate a noticeable amount of new elements. This problem is solved in further experiments.

4.1. EXPERIMENT 3. A HALOGEN INCANDESCENT LAMP AND A CIRCULATING SOLUTION

The halogen incandescent lamp (220V, 300 W) was located in a quartz tube, through which a 10% aqueous solution of KNO₃ seeped (Fig. 8). The circulating solution was cooled by passing through heat exchanger. The reactor operated for 20 hours at power consumption of 450 W. Heat output power, determined by the heating rate of the solution, is about 500 W. Average



Fig. 8. Experimental setup with a circulating KNO₃ solution and a halogen incandescent lamp.

temperature of the tungsten filament is about 2400°C.

Samples of the solution taken before and after the experiment, after evaporation, were transferred for analysis of the elemental composition to the SYNTHESTECH Research Center. Two methods were used: X-ray fluorescence (XRF) and mass spectral (ICP MS). The results of the analyses are presented in **Table 1**.

It can be seen that the content of many elements after treatment of the solution increased by tens or even hundreds of times. Using the tables of possible transformations of nuclides [11,12], it is possible to detect many possible nuclear transformations, which result in the chemical elements indicated in Table 1. The starting elements can be potassium, nitrogen, oxygen, and hydrogen. Below are some of the possible nuclear transformations that result in the detected lithium, boron, magnesium, aluminum, calcium, and iron:

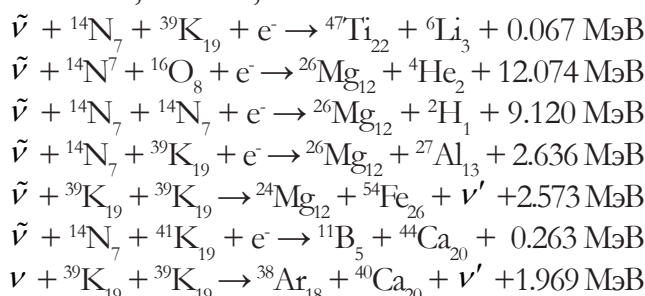


Table 1.
Results of analysis of KNO_3 samples by RFA and ICP MS methods before and after treatment in an incandescent lamp unit in KNO_3 solution (mass %).

	Before		After	
	XRF	ICP MS	XRF	ICP MS
Li		0.007		0.12
Be		0.017		0.08
Mg		0.050		0.55
Al		0.010		3.30
K	99.01		86.04	
Ca	<0.01		10.2	
Fe	<0.01		0.66	
Cu	0.018		2.04	
Cu		0.010		1.10
Zn	<0.01		0.58	
Zn		0.010		0.13
Ni	<0.01		0.048	

The calcium content increased the most (the appearance of calcium is also typical for many other LENR experiments [1,2]). The last of the written equations are just two of the many possible ways in which calcium can appear. In this regard, we can recall the research of Louis Kervran, who found that chickens continue to lay eggs, the shell of which contains a lot of calcium, even if it is completely deprived of its sources of calcium, replacing calcium with potassium [7]. He suggested that calcium occurs as a result of the nuclear reaction ${}^{39}\text{K}_{19} + {}^1\text{H}_1 \rightarrow {}^{40}\text{Ca}_{20} + 8.337 \text{ MeV}$, which caused the ridicule of physicists: potassium and hydrogen cannot combine because of the "Coulomb barrier", and if this somehow happened, the huge energy release of the chicken would incinerate. However, if this happens as a result of weak interactions $\nu + {}^{39}\text{K}_{19} + {}^1\text{H}_1 \rightarrow {}^{40}\text{Ca}_{20} + \nu' + 8.337 \text{ M}\ddot{\text{e}}\text{B}$, both the problem of the "Coulomb barrier" and the problem of huge energy release are removed. According to the laws of conservation of energy and momentum, if energy is released in a system of two particles, it is distributed inversely to the masses. Since the mass of the neutrino is much less than the mass of the calcium nucleus, almost all of the released energy is carried away by neutrino. Where do the neutrinos that initiate the nuclear reaction come from? As already noted, cellular metabolism is characterized by energies of the order of 1 eV, which is sufficient for the formation of neutrinos and antineutrinos.

4.2. EXPERIMENT 4. HALOGEN INCANDESCENT LAMP AND TIN-LEAD ALLOY

The 300-watt halogen incandescent light bulb was wrapped in lead-tin alloy tape and placed in a container of water. To avoid overheating and boiling, the water was cooled by pumping through a fan-cooled coil (**Fig. 9**). The lamp power consumption is 480 W. Heat output power of about 550 W was determined by the water heating rate. Temperature of the tungsten filament is 2400-2450°C. Working time is 40 hours.



Fig. 9. Halogen incandescent lamp wrapped with a tin-lead alloy tape in a vessel with water. The water is pumped through a fan-cooled coil.

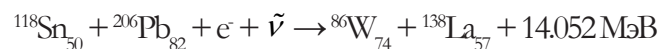
Samples of the lead-tin alloy before and after processing in the described installation were transferred for analysis of the elemental composition by XRF and ICP MS methods to the SYNTHESTECH Research Center. The results of the analyses are presented in **Table 2**.

Table 2.
Content of some elements in the lead-tin alloy before
and after processing (mass %)

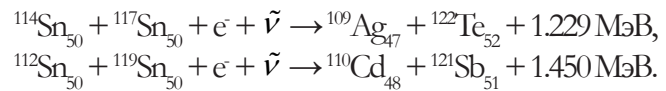
	Before		After	
	XRF	ICP MS	XRF	ICP MS
Li		0.0001		0.0063
B		0.0012		0.012
Na		0.13		1.16
Al		0.001		0.024
K		0.056		0.75
Ca		0.018		0.34
Fe	<0.01		0.27	
Fe		0.014		0.13
Co		0.0002		0.014
Ni	<0.01		0.073	
Ni		0.0006		0.018
Cu		0.012		0.041
Zn		0.0038		0.040
Pd		0.0002		0.0005
Ag		0.006		0.024
Cd		0.0005		0.0011
Sn	45.7	43.6	40.3	46.0
W	<0.01		1.51	
W		0.00003		0.105
Pb	54.2	44.5	57.9	31.4
Bi		0.0005		0.057

It can be seen that the content of many elements after processing has increased many times. Especially strongly increased the content of lithium, sodium, aluminum, potassium, calcium, iron, cobalt, silver, cadmium, tungsten, bismuth.

The alloy of tin and lead is favorable for the appearance of tungsten: tin has 12 isotopes, lead has 4 isotopes. Combinations of these isotopes open up 32 channels for converting tin and lead to tungsten [12]. We show one of the variants of such transformations:



Rearrangements between tin isotopes can give rise to the formation of silver in 8 channels and cadmium in 9 channels, for example:



Using the tables of possible transformations of nuclides [11,12], it is possible to detect many possible nuclear transformations, which result in the chemical elements indicated in Table 2.

Note that the XRF analysis provides information about the elemental composition in the thin surface layer of the test sample. Therefore, it is quite possible to participate in transmutations in this layer of hydrogen, which is part of the water that washes the sample during the experiment. In contrast to XRF, ICP MS analysis provides thickness-averaged information. Hydrogen cannot penetrate deep into the lead-tin alloy. Therefore, if the participation of hydrogen in transmutations is necessary, the analysis of the composition of the samples during the ICP MS study would reveal significantly smaller changes than changes in the surface layer by the XRF method. However, strong changes were detected by both methods, which confirms that the participation of hydrogen in nuclear transmutations is optional. This is also indicated the calorimetric experiment with an incandescent lamp and lithium tetraborate, described above.



Fig. 10. Halogen incandescent lamp in boiling water with NaBiO_3 suspension.

4.3. EXPERIMENT 5. HALOGEN INCANDESCENT LAMP AND BOILING SOLUTION

In a glass vessel with 900 ml of water and 14 g of sodium bismuthate (NaBiO_3), a halogen incandescent lamp with a rated power of 150 W is immersed (Fig. 10). The duration of the experiment is 20 hours with a power consumption of 270 W. The temperature of the tungsten filament is 2200-2300°C. Excess heat generation with a power of about 25 W was determined by the evaporation rate of water. Since sodium bismuthate is insoluble in water, it was suspended during the operation of the setup.

After the end of the experiment, XRF analyses of the precipitate and the evaporated solution, as well as the initial NaBiO_3 powder, were performed at the SYNTHESTECH Research Center. The results are presented in Table 3.

In the starting material, except for bismuth, only platinum was found. The presence of a number of other elements was revealed in the formed sediment and in the solution. In particular, as in experiment 4, a lot of tungsten appeared. This can happen, for example, in the following ways:

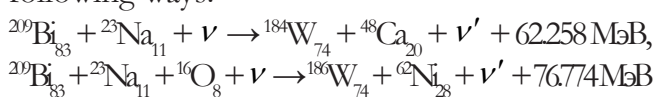


Table 3.
Results of the analysis of the content of chemical elements before and after the experiment (mass %).

	Starting powder	Treated	
		Sediment	Solution
S	<0.01	<0.01	6.167
Ca	<0.01	0.231	<0.01
Fe	<0.01	0.092	<0.01
Cu	<0.01	<0.01	0.396
Dy	<0.01	<0.01	0.451
Ta	<0.01	0.246	<0.01
W	<0.01	0.289	88.371
Pt	0.562	0.496	<0.01
Bi	99.498	99.646	4.615

4.4. EXPERIMENTS 6. HOT METAL OR LIGHT?

In 2013, at the Kurchatov Institute, Yu.N.Bazhutov and his colleagues realized a series of experiments with solutions of LiOH , NaOH , and Na_2CO_3 illuminated by a laser or LED with a wavelength of 625-650 nm [24,25]. It was found that a tritium appears in the solutions (1 tritium atom per 10^{13} - 10^{14} radiated photons). No noticeable excess heat generation was detected.

Ubaldo Mastromatteo discovered the appearance of C, O, Na, Si, Al, Mg, S, Cl, K, Ca, and Cu in the atmosphere of hydrogen and deuterium as a result of two weeks of laser irradiation with 633 and 405 nm wavelengths of palladium film [26]. This experiment was recently reproduced by Jean-Paul Biberian [27]. After three months of irradiation in the atmosphere of hydrogen or deuterium of a palladium film with a 5 mW semiconductor laser with a wavelength of 650 nm, initially absent N, O, Na, S, Al, Ca, Fe, Ni, Zn, Mo were detected. The presence of excessive heat release was not controlled.

Thus, light exposure causes nuclear transmutations. Our experiments described in this article are accompanied by very intense light radiation. Perhaps it is due to the action of light that the appearance of new elements and excessive heat generation is associated? Photons with a wavelength of 650 nm have an energy of about 2 eV, which is more than enough to produce a

pair of neutrinos-antineutrinos that cause nuclear transmutations. Such energy is also sufficient to generate a monopole-antimonopoly pair with masses of 0.048 eV, which, as it is assumed, can also cause nuclear transmutations [28].

To test this possibility, a calorimetric experiment was conducted with a chain of 15 LEDs extracted from a household LED lamp (**Fig. 11**). The same calorimeter with water in the Dewar vessel was used, which was used in experiments with incandescent lamps (see Fig. 6).

The measurements showed that the LEDs immersed in water do not give a noticeable excess heat release ($COP = 1.00 \pm 0.01$). The LED block, surrounded by aluminum foil or quartz, also gave no noticeable excess heat generation.

It can be concluded that, although light causes nuclear transmutations, they can only be noticed when very long-term illumination with powerful light. The efficiency of the reactors described in this article is related precisely to the presence of hot metal.

5. NEW APPROACH TO CREATING LENR REACTORS

In structures that have already become traditional, the zone with a high temperature (metal saturated with hydrogen, plasma) is surrounded by a layer of a substance that performs the contradictory tasks of thermal insulation and heat removal. This does not allow us to create powerful reactors with a high ratio of released and consumed energy.

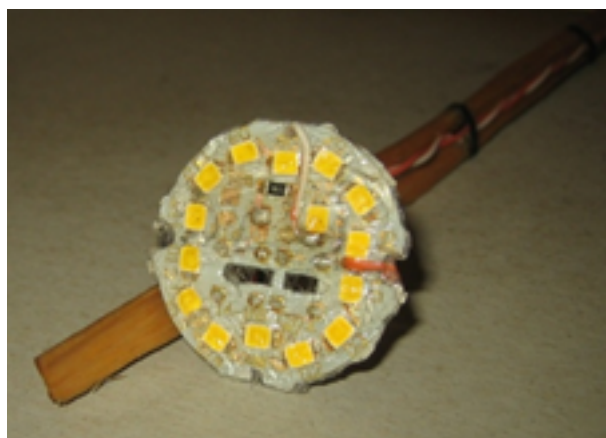


Fig. 11. LEDs used in the calorimetric experiment.

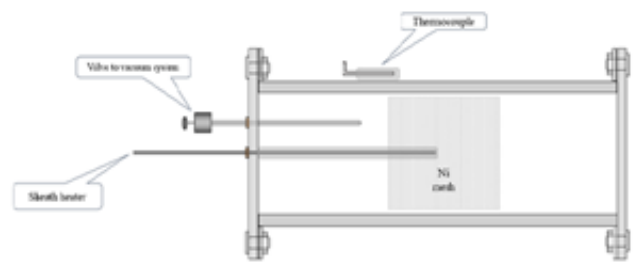


Fig. 12. Diagram of the Mizuno reactor.

The presented hypothesis allows a new approach to the design of LENR reactors. The source of the agent that causes nuclear transmutation (hot metal or dense plasma) can be placed inside the thermal insulation. This allows you to reach a high temperature using a low-power heater. Fuel (a substance where processes with a large heat release occur) can be located on the periphery, which allows you to efficiently remove the heat generated.

This is the configuration of the reactor created by Tadahiko Mizuno [22] (**Fig. 12**), which, consuming 300 watts of electrical power, produced 2-3 kW of heat. In this reactor, the high-temperature heater is located inside a thermal insulation - rarefied deuterium gas. The fuel (nickel mesh with a thin layer of palladium deposited on it, in which deuterium is dissolved) is located at the periphery in thermal contact with the outer wall of stainless steel.

In the C3 reactor (**Fig. 13**), an iron cylinder weighing 60 g was heated by a tungsten spiral

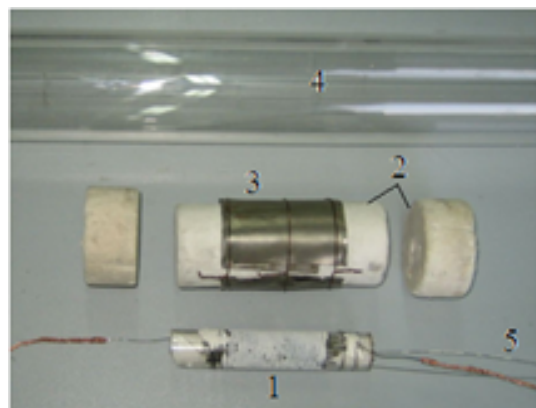


Fig. 13. Details of the C3 reactor. 1 - iron cylinder in a sapphire tube, on which a tungsten heater is wound; 2-thermal insulation; 3-nickel mesh; 4-quartz tube; 5- thermocouple W-Re.

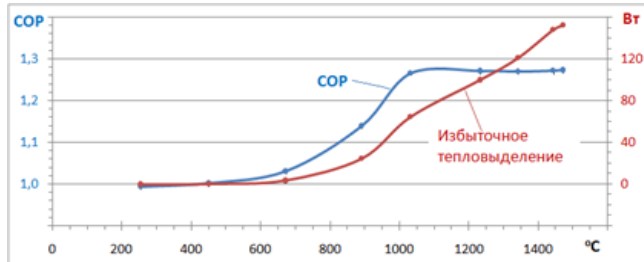


Fig. 14. The excess heat output power and the thermal coefficient of the C3 reactor as a function of temperature.

wound on a sapphire tube. The "hot zone" is surrounded by thermal insulation made of porous quartz, wrapped in nickel nets. Between the grids there was 15 g of nickel powder saturated with hydrogen. The outer shell is a quartz tube filled with a mixture of hydrogen and argon. To measure the heat output power, a flow-through air calorimeter was used (see Fig. 4).

Fig. 14 shows the dependence of the excess heat output power and the thermal coefficient of the C3 reactor on the temperature. A noticeable excess heat release is observed already at the iron core temperature of 800°C and continuously increases with increasing temperature. The thermal coefficient at a temperature of about 1000°C reaches a value of about 1.3. An increase in temperature does not lead to an increase in COP due to the rapid increase in the power consumed by the electric heater.

The W1 reactor uses a tubular silicon carbide heater and a tungsten core, which allows for a higher temperature than the C3 reactor, which has an iron core. Design of the reactor is shown in **Fig. 15**. Inside the silicon carbide heater there is a tungsten powder weighing 3.1 g. The heater is surrounded by thermal insulation made of porous ceramics. Between the thermal insulation and the outer quartz pipe is hydrogen-rich nickel

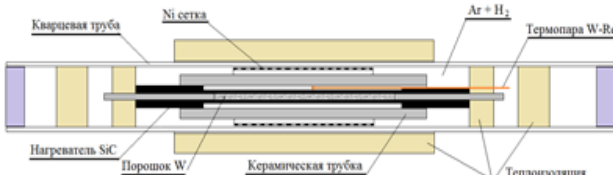


Fig. 15. Design of the W1 reactor.

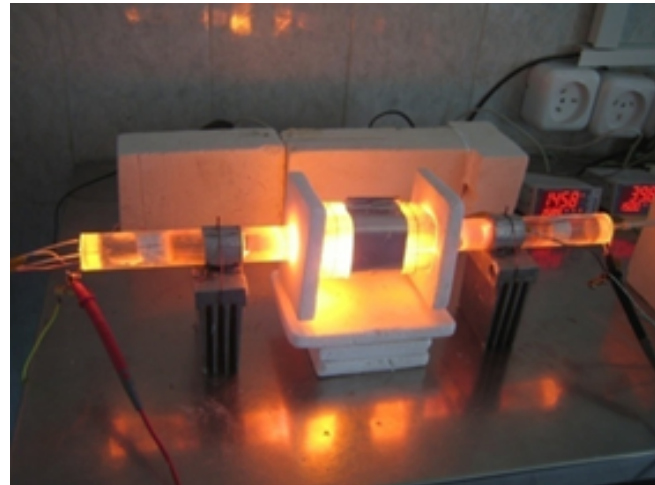


Fig. 16. Reactor W1 and the process of operation.

mesh ("fuel"). A view of the reactor in operation is shown in **Fig. 16**.

Fig. 17 shows the dependence of the excess heat output power and the thermal coefficient of the C3 reactor on the temperature. This reactor produced up to 1.000 W of excess power. A noticeable excess heat generation appears at a temperature of 1100°C and increases with increasing temperature. The thermal coefficient also increases, reaching a value of 2.2 at a temperature of about 1600°C . At higher temperatures, growth slows down.

CONCLUSION

A number of experiments have been carried out to confirm the hypothesis that low-energy neutrinos, which occur as a result of collisions of matter particles during their thermal motion, can cause nuclear transformations. The energy release predicted by the hypothesis in a substance near a metal heated to a high temperature is confirmed. Analysis of changes in the elemental composition in the substance

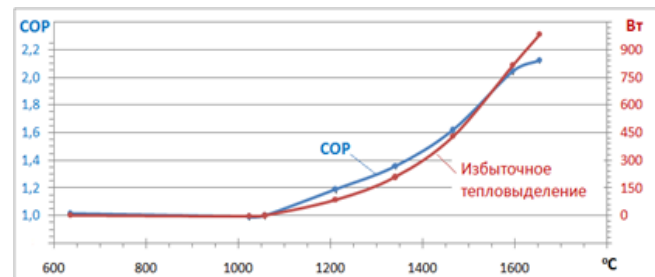


Fig. 17. Excess heat output power and thermal coefficient of the reactor W1 as a function of temperature.

around incandescent lamps showed a significant increase in the content of a number of chemical elements.

The presence of such changes, along with the detected excess heat release, proves that, indeed, the hot metals emit an agent that initiates nuclear transformations in the surrounding matter. The correspondence of the detected transformations to possible nuclear reactions initiated by neutrinos (antineutrinos) indicates that these agents are neutrinos and antineutrinos.

This allows a new approach to design of LENR reactors. Source of the agent that causes nuclear transmutation (hot metal or dense plasma) can be placed inside of thermal insulation, which allows you to achieve a high temperature with low energy consumption. Fuel (a substance where processes with a large heat release occur) can be located on the periphery, which allows you to efficiently remove the heat generated. Several reactors manufactured according to this scheme have been tested. One of them managed to achieve an excess heat output of 1 kW (COP = 2.2).

REFERENCES

1. Parkhomov AG, Alabin KA, Andreev SN et al. Nickel-hydrogen reactors: heat release, isotopic and elemental composition of fuel. *RENSIT*, 2017, 9(1):74-93.
2. Parkhomov AG, Zhigalov VA, Zabavin SN et al. Nikel-vodorodnyiy teplogenerator, nepreryivno prorabotavshiy 7 mesyatsev [Nickel-hydrogen heat generator, continuously worked for 7 months]. *JFNN*, 2019, 23-24(7):57-63 (in Russ.), <http://www.unconv-science.org/pdf/23/parkhomov2.pdf>.
3. Vachaev AV, Ivanov NI, Ivanov AN, Pavlova GA. Sposob polucheniya elementov i ustroystvo dlya ego osuschestvleniya [Method of obtaining elements and device for its implementation]. Patent of the Russian Federation No. 2096846, MKI G 21 G 1/00, H 05 H 1/24. Application 31.05.94. Izobreteniya, 1997, No.32:369 (in Russ.).
4. Bazhutov YuN, Gerasimova AI, Koretsky VP, Parkhomov AG. Osobennosti potrebleniya elektroenergii, vydeleniya tepla i izlucheniya v protsesse plazmennogo elektroliza. [Features of electricity consumption, heat release and radiation in the process of plasma electrolysis]. *Proc. of the 21st Russian Conf. on Cold Nuclear Transmutations and Ball Lightning*. Sochi, 2015:122-131 (in Russ.).
5. Savvatimova IB. Transmutation of Elements in Low-energy Glow Discharge and the Associated Processes. *J. Condensed Matter Nucl*, 2011, 8:1-19.
6. Fleischmann M, Pons S. Electrochemically induced nuclear fusion of deuterium. *Journal of Electroanalytical Chemistry and Interfacial Electrochemistry*, 1989, 261(2A):301-308.
7. Kervran L. *Biological Transmutations*. Happiness Press, USA, Magalia, California, 1998.
8. Kornilova AA, Vysotsky VI. Synthesis and transmutation of stable and radioactive isotopes in biological systems. *RENSIT*, 2017, 9(1):52-64.
9. Parkhomov AG. LENR kak proyavlenie slabiyih yadernyih vzaimodeystviy [LENR as a manifestation of weak nuclear interactions]. *JFNN*, 2019, 23-24(7):6-8 (in Russ.), <http://www.unconv-science.org/pdf/23/parkhomov1.pdf>.
10. Parkhomov AG. Weak Interactions as Essence of LENR. *International Journal of Unconventional Science*, 2019, E4:3-5, <http://www.unconv-science.org/pdf/23/parkhomov1-en.pdf>.
11. Parkhomov AG. Mnogoobrazie nuklidov, voznikayushchih v protsesse holodnyih yadernyih transmutatsiy [Diversity of nuclides arising in the process of cold nuclear transmutations]. *JFNN*, 2017, 17-18: 99-101 (in Russ.) Table of possible nuclear transformations can be obtained in EXCEL format from A.G.Parkhomov: alexparh@mail.ru.
12. Parkhomov AG. Multeity of Nuclides Arising in the Process of Cold Nuclear Transmutations Involving Electrons. *International Journal of Unconventional Science*.

- 2018, E3:32-33, <http://www.unconsciencce.org/pdf/e3/parkhomov-en.pdf>. Table of possible nuclear transformations can be obtained in EXCEL format from A.G.Parkhomov: alexparh@mail.ru.
13. Parkhomov AG. Ritmicheskie i sporadicheskie izmeneniya skorosti beta raspadov. Vozmojnyie prichiny [Rhythmic and sporadic changes in the beta decay rate. Possible reasons]. *JFNN*, 2018, 21-22(6):86-96 (in Russ.).
14. Parkhomov AG. Rhythmic and Sporadic Changes in the Rate of Beta Decays Possible Reasons. *Journal of Modern Physics*, 2018, 09(08):1617-1632.
15. Thomas SA, Abdalla FB and Lahav O. Upper Bound of 0.28 eV on Neutrino Masses from the Largest Photometric Redshift Survey. *Phys. Rev. Lett.*, 2010, 105(3):031301.
16. Landau LD, Lifshits EM. Statisticheskaya fizika [Statistical Physics]. Moscow: Nauka Publ., 1964, p. 108.
17. Prokhorov AM (ed) Fizicheskaya entsiklopediya [Physical encyclopedia]. Vol. 3. Moscow, Bolshaya Rossiyskaya enciklopediya Publ., 1992.
18. Kaganov IL. *Ionye priboryi* [Ion devices]. Moscow, Energiya Publ., 1972, 528 p.
19. Mukhin KN. *Vvedenie v yadernuyu fiziku* [Introduction to nuclear physics]. Moscow, Atomizdat Publ., 1965, pp. 203-212.
20. Parhomov AG. Novyj podhod k sozdaniyu LENR reaktorov [New approach to the creation of LENR reactors]. Parhomov A.G. Karabanov R.V. Issledovanie ehlementnyh i izotopnyh izmenenij v veshchestve okolo lamp nakalivaniya [Investigation of elemental and isotopic changes in matter near incandescent lamps]. *Proc. of the 26th Russian Conf. on cold nuclear transmutations and ball lightning*. Moscow, 2020, p. 43-63 (in Russ.)
21. Grigoriev IS, Meilikov EZ (ed) *Fizicheskie velichiny* [Physical quantity]. Moscow, Energoatomizdat Publ., 1991. p. 438.
22. Mizuno T and Rothwell J. Increased Excess Heat from Palladium Deposited on Nickel (Preprint). *Proc. of 22nd International Conference for Condensed Matter Nuclear Science (ICCF-22)*, 2019, Assisi, Italy, <http://lenr-canr.org/acrobat/MizunoTincreasede.pdf>.
23. Parkhomov AG. Neytrino malyih energiy kak prichina anomalii v beta raspadah i holodnyih yadernyih transmutatsiy [Low-energy neutrinos as the cause of anomalies in beta decays and cold nuclear transmutations]. *Metaphizika*, 2020, 4(38):49-66 (in Russ.).
24. Bazhutov YuN, Gerasimova AI, Koretsky VP, Evmenenko VV, Parkhomov AG, Sapozhnikov YuA. Kalorimetricheskaya i neytronnaya diagnostika vodnyih rastvorov pri intensivnom svetovom obлучenii [Calorimetric and neutron diagnostics of aqueous solutions under intense light irradiation]. *Proc. of 20th Russian Conf. on cold Nuclear transmutations and ball lightning*. Loo, Sochi, September 29-October 6, 2013, pp. 55-64 (in Russ.)
25. Bazhutov YuN, Gerasimova AI, Evmenenko VV, Koretskiy VP, Parkhomov AG and Sapozhnikov YuA. Calorimetric and Radiation Diagnostics of Water Solutions Under Intense Light Radiation. *J. Condensed Matter Nucl. Sci.*, 2016, 19:10-17.
26. Mastromatteo U. LENR Anomalies in Pd-H₂ Systems Submitted to Laser Stimulation. *J. Condensed Matter Nucl. Sci.* 2016, 19:173-182
27. Biberian J-P. Transmutation induced by laser irradiation. *Le colloque RNBE*, 2020.
28. Kovacs A. Magnetic monopole mass and charge radius calculation from experimental data analysis. *Proc. of the 26th Russian Conf. on cold nuclear transmutations and ball lightning*. Moscow, 2020, p. 205-219.

DOI: 10.17725/rensit.2021.13.059

Hot laser fusion or low temperature nuclear reactions? Analysis and current prospects of the first experiments on laser fusion

Vladimir I. Vysotskii, Mykhaylo V. Vysotskyy

Taras Shevchenko National University of Kyiv, Faculty of Radiophysics, Electronics and Computer Systems,
<http://www.univ.kiev.ua/>
Kyiv 01033, Ukraine

E-mail: vivysotskii@gmail.com, mihas1984@gmail.com

Alla A. Kornilova

Lomonosov Moscow State University, Faculty of Physics, <http://www.phys.msu.ru/>
Moscow 119991, Russian Federation

E-mail: prfnart@mail.ru

Received March 12, 2021, peer-reviewed March 18, 2021, accepted March 20, 2021

Abstract: The paper considers the features and quantitative characteristics of the first successful laser experiments on the formation of a thermonuclear plasma and registration of neutrons in nuclear fusion reactions under pulsed irradiation of a LiD crystal. Quantitative analysis shows that the production of neutrons recorded in these experiments is not associated with thermonuclear reactions in hot laser plasma. The most probable mechanism of neutron generation is associated with nuclear reactions at low energies and is due to the formation of coherent correlated states (CCS) of deuterons. In this experiment, such states can be formed in two different processes: due to the effect of a shock wave in the undisturbed part of the target lattice on the vibrational state of deuterium nuclei or when deuterium nuclei with an energy of about 500 eV move in the lattice. This part of the deuterium nuclei corresponds to the high-energy "tail" of the Maxwellian distribution of the total flux of particles entering from the laser plasma into the interplanar channel. In this second case, the process of the formation of the CCS is associated with the longitudinal periodicity of the interplanar crystal channel, which is equivalent to a nonstationary oscillator in the own coordinate system of moving particle. The expediency of repeating these experiments is shown, in which, in addition to neutrons, one should expect a more efficient generation of other nuclear fusion products due to low-energy reactions involving lithium isotopes from the target composition.

Keywords: laser and thermonuclear fusion, nuclear reactions at low energy, coherent correlated states, tunneling effect

PACS: 03.65.Xp; 25.60.Pj; 25.70.-z; 25.85.Ge; 28.52.-s

For citation: Vladimir I. Vysotskii, Alla A. Kornilova, Mykhaylo V. Vysotskyy. Hot laser fusion or low temperature nuclear reactions? Analysis and current prospects of the first experiments on laser fusion. RENSIT, 2021, 13(1):59-70. DOI: 10.17725/rensit.2021.13.059.

CONTENTS

1. INTRODUCTION (60)
2. ANALYSIS OF THE FIRST EXPERIMENTS ON LASER SYNTHESIS (60)
3. AN ALTERNATIVE MECHANISM FOR THE GENERATION OF NEUTRONS AND OTHER PARTICLES UNDER THE ACTION OF A LASER PULSE ON A LiD TARGET (62)
 - 3.1. FEATURES OF NUCLEAR REACTIONS AT LOW ENERGY IN NONSTATIONARY

MICROCRACKS STIMULATED BY THE ACTION

OF A LASER PULSE ON A TARGET (62)

- 3.2. THE MECHANISM OF NUCLEAR FUSION AT LOW ENERGY ASSOCIATED WITH THE MOVEMENT OF IONS IN THE CRYSTAL LATTICE OF THE TARGET (65)

4. CONCLUSION (66)

REFERENCES (68)

1. INTRODUCTION

The question of realizing of energy-efficient controlled nuclear fusion is undoubtedly one of the most actual and widely discussed problems. Special interest to this problem is due to the fact that the potential and effectiveness of such reactions does not need to be proved, since all life on Earth is due to the Sun, where such processes have been continuously going on for 5 billion years. Real study of this problem began in the mid-50s after the implementation of uncontrolled fusion in the form of a hydrogen bomb, when most of the scientists who had previously dealt with purely explosive topics (including such outstanding physicists as A.D. Sakharov, L.A. Artsimovich, I.E. Tamm, I.V. Kurchatov), quickly came to a consensus on the basic idea: the implementation of a controlled thermonuclear fusion based on high-temperature plasma with magnetic confinement in systems of the TOKAMAK type. The initially unrecognized exceptional complexity of the task of confining high-temperature plasma in such a system turned out to be a tough nut to crack. Despite huge financial investments, it did not allow for the next 60 years to create a successful and energy-efficient prototype of such a device. An alternative model of inertial confinement of short-lived dense hot plasma eliminated the problem of magnetic confinement and was directly associated (on a smaller scale) with uncontrolled fusion in a hydrogen bomb, but required corresponding high-speed efficient drivers. The successes of the synchronously developing laser physics were the impetus that led to the idea of laser inertial fusion. It is quite natural that those outstanding scientists (primarily N.G. Basov) who very successfully creating high-power pulsed lasers, quickly came up with the idea of using such lasers to implement inertial thermonuclear fusion. The idea of using powerful lasers to implement controlled thermo-nuclear synthesis was first

expressed in 1960 by A.D. Sakharov on the basis of a modernized explosive thermonuclear fusion scheme (a hollow mirror ellipsoid, in the foci of which there is a compressible fuel and a laser radiation source). A more realistic scheme for heating and compressing a target by laser radiation was proposed in 1961 by N.G. Basov and O.N. Krokhin.

2. ANALYSIS OF THE FIRST EXPERIMENTS ON LASER SYNTHESIS

The first experiments on the realization of nuclear fusion stimulated by laser action on a target were carried out in the late 1960s [1-3] according to the simplified scheme shown in **Fig. 1** and does not imply target compression.

It was assumed that intense one-sided localized heating of a small part of the target surface using short ($\sim 10^{-11}$ s) single laser optical pulses with an energy of about 10 J, generated by a high-power neodymium laser with a wavelength of 1.06 μm , during the action of each pulse on the LiD surface target would allow to realize such a short-term hot plasma, within which thermonuclear fusion will be possible until the moment of expansion. To increase the radiation intensity, a long-focus lens was additionally used, which made it

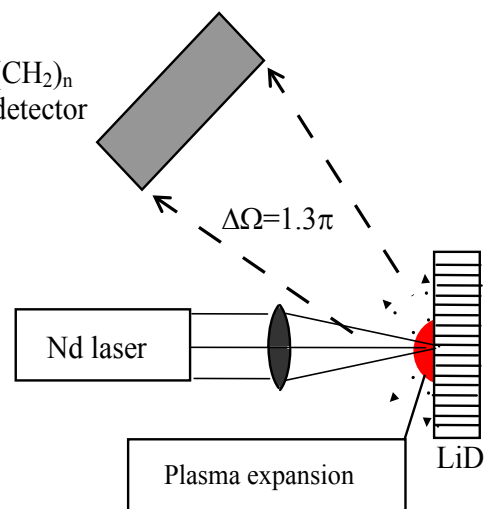


Fig. 1. General scheme of experiments on laser synthesis of neutrons in a LiD target.

possible to achieve a record intensity of $J \approx 10^{16}$ W/cm². It should be noted that even 50 years after these experiments, such an intensity is quite adequate for such studies, and even today these parameters significantly exceed only the pulses generated by modern picosecond or femtosecond lasers.

The authors of the experiments expected that in the hot plasma formed near the target surface, synthesis based on one of the d - d synthesis channels would be possible



implementing due to collision of deuterons into the hot plasma.

To confirm the implementation of such a synthesis, a scintillation detector based on a polystyrene (CH₂)_n crystal was used. According to the authors' estimates, the neutron detection efficiency, taking into account the geometric parameters of the detector, the solid angle of registration $\Delta\Omega = 1.3\pi$ and the probability of the formation of optical quanta during the interaction of neutrons with hydrogen nuclei, corresponded to $\eta \approx 10\%$.

From the results of experiments [1,2] it follows that under such a pulsed action, on average $N_{neutron} \approx 1$ neutron was recorded for each laser pulse, which corresponded to generation

$$N_{neutron}^0 \approx N_{neutron} / \eta \approx 10 \text{ neutrons/pulse} \quad (2)$$

These data were interpreted by authors as the first demonstration of the inertial laser thermonuclear (hot) synthesis. It should be noted that in [1-3] a very detailed analysis of the process of formation of hot plasma using specific laser pulses was carried out, but the quantitative features of nuclear fusion were almost not considered and the results of experiments were not compared with the calculated parameters of the expected hot fusion.

Such an analysis can be easily carried out on the basis of a technique that is now widely used both for the analysis of similar problems in laboratory and industrial nuclear fusion, as well

as in the analysis of astrophysical processes in stars.

According to the authors of [1-3], during the action of each of the laser pulses on the LiD target, plasma with the following parameters was formed:

- deuterium ion concentration - $n_d \approx 10^{21}$ cm⁻³;
- average thickness of the plasma region near the laser focus - $x_0 \approx 10^{-2}$ cm;
- the temperature of the ion component of the plasma - $kT_{max} \approx 120$ eV corresponded to the close-to-spherical geometry of its expansion (see. [3], Fig. 10);
- the lifetime of a plasma with such a temperature - $\tau \approx 5 \cdot 10^{-10}$ s;
- rms velocity of deuterium ions in plasma at maximum temperature - $\langle v \rangle \approx \sqrt{3kT/M} \approx 10^7$ cm/s.

If we assume that the area of transverse expansion of the plasma (taking into account the initial cross section of the focused laser pulse $S_0 = \pi R_0^2 \approx 3 \cdot 10^{-4}$ cm²) during its existence was equal $S_\tau \approx \pi(\langle v \rangle \tau + R_0)^2 \approx 6 \cdot 10^{-4}$ cm², then in the volume of plasma there were $N_d = n_d S_\tau x_0 \approx 6 \cdot 10^{15}$ deuterium nuclei.

Based on these data, taking into account the cross section of the reaction $\sigma(v)$ and the speed of the particles participating in it, it is possible to calculate the total number (*d-d*) of reactions and, accordingly, the total number of generated neutrons,

$$N_{neutron}^0 \approx V n_0^2 \langle \sigma(v) v \rangle \tau / 2, \quad (3)$$

in the volume of the laser plasma during its existence τ .

The standard expression for the reaction rate $\sigma(v)v$ averaged over the Maxwellian distribution of ions in the plasma is determined by the well-known formula (eg, [4], Chapter 2)

$$\langle \sigma(v)v \rangle_{dd} \approx 1.3 \cdot 10^{-14} \frac{1}{(kT)^{2/3}} \exp\left(-\frac{18.8}{(kT)^{1/3}}\right) [\text{cm}^3/\text{s}] \quad (4)$$

Here kT corresponds to the plasma temperature in units of keV.

Substituting the above parameters, we can find $\langle \sigma(v)v \rangle_{dd} \approx 5 \cdot 10^{-30} \text{ cm}^3/\text{s}$.

When this quantity is taken into account, from (3) it follows an estimate of the average number of neutrons generated in experiments [1,2] when a single laser pulse is exposed to a LiD target

$$N_{\text{neutron}}^0 \approx 0.007 \text{ neutrons/pulse.} \quad (5)$$

This value is 1500 times less than the estimate (2), which was made by the authors of the experiments on the basis of the neutron registration process under experimental conditions [1,2].

It is obvious from these estimates that the considered thermonuclear mechanism can provide only 0.07% of the total number of neutrons generated in the experiments performed.

We have no doubt about the very high qualifications of the authors of works [1-3] and the correctness of their measurements, but the question immediately arises about the mechanism and substantiation of those processes that led to the generation of neutrons under the one-sided action of single laser pulses on the LiD target.

3. AN ALTERNATIVE MECHANISM FOR THE GENERATION OF NEUTRONS AND OTHER PARTICLES UNDER THE ACTION OF A LASER PULSE ON A LID TARGET

The subsequent analysis shows that the neutrons recorded in the experiments under consideration were generated in the process of low-energy nuclear reactions (LENR), which were stimulated by effects that are not directly related to an increase in the temperature of deuterium nuclei under the action of laser pulses on the target surface and are realized even at relatively low energy and temperature.

Two basic mechanisms that are based on the same physical process and lead to efficient nuclear fusion can be noted.

3.1. FEATURES OF NUCLEAR REACTIONS AT LOW ENERGY IN NONSTATIONARY MICROCRACKS STIMULATED BY THE ACTION OF A LASER PULSE ON THE TARGET

It is well known that when a laser pulse acts on a target, an ablation process always takes place due to intense pulsed evaporation of fast ions from that part of the target surface on which the laser pulse acts. This evaporation is accompanied by the transfer of momentum to the target, which leads to the formation of an intense shock wave moving deeper into the target perpendicular to its surface. Such a mechanism for generating shock waves is well known (eg, [5-9]).

The shock pressure on the remaining (non-evaporated) part of the target surface with this ablation mechanism is $P \approx 4 \cdot 10^6 \text{ atm}$ at a laser pulse intensity $J = 10^{13} \text{ W/cm}^2$ [5]. With an increase in the laser pulse intensity, the pressure sharply increases $P \sim J^{7/9}$ [8,9], reaching gigantic values $P \approx 10^8 \dots 10^9 \text{ atm}$ at an intensity $J \approx 10^{16} \text{ W/cm}^2$ corresponding to this experiment.

The speed of the front of the shock wave with the above parameters of the laser pulse can reach or exceed 4...8 km/s. When this shock wave moves inside any material bodies, a very sharp narrowing of its leading front occurs to a size limited by several free path lengths of the accelerated ions. In the case of a solid target, the minimum value of the leading edge corresponds to several nm. This "steepening" of the shock front is due to the fact that the more intense (increasing) part of the shock front, due to the nonlinearity of the interaction process, moves faster than the less intense front part of the front and "catches up" with it.

The passage of this shock wave through a target containing deuterium and lithium leads to a very fast ($\sim 10^{-11} \dots 10^{-13} \text{ s}$) shock compression, and then rapid expansion and subsequent slower relaxation of the local environment of

each of the deuterium and lithium atoms in the target. From the point of view of crystal lattice dynamics, these processes correspond to very fast pulsed reversible modulation of parameters and vibration frequency of a nonstationary harmonic oscillator characterizing the vibrational state of each of the deuterium nuclei in the lattice (including optical phonon modes at frequencies of 10...15 THz).

Such very fast process of nonstationary modulation leads to phase synchronization (otherwise, constructive interference) of optical phonon modes of the same particle and to the formation of a coherent correlated state (CCS) of these particles (nuclei). It leads to the generation of giant fluctuations of the momentum and energy of the corresponding nuclei accompanying these states [10-23]. Obviously, this mechanism of pulsed modulation of the parameters of the local oscillator is much more effective in the region adjacent to the target surface, near which the laser plasma is formed. In this region, even before the arrival of the shock wave, numerous nanocracks arise, which are formed due to the entry of fast ions, escaping from the volume of the near-surface plasma. This process is similar to the cracking procedure for metal hydrides of the TiD or TiH type upon their rapid saturation with hydrogen isotopes. The relatively large width of these nanocracks filled with deuterium sharply (several times) increases the amplitude of the possible modulation of the frequency of deuteron oscillations upon the subsequent action of a shock wave on this nanocrack. Another important result of the action of the shock wave is the accelerated "opening" of those nanocracks that had not yet formed, but were in a very stressed state due to the internal pressure of deuterons trapped in the interstice of the target lattice. This process is possible anywhere in the target.

It was shown in [10-17] that at such a very fast pulse modulation of the parameters of a nonstationary oscillator, the amplitude of

particle momentum fluctuations increases sharply, as a result of which fluctuations of the kinetic energy of a particle (in particular of a proton) can reach $\delta E_{\text{corr}} \geq 10 \dots 30 \text{ keV}$ even in the case of a crystal lattice at room temperature. An important fact is that during the generation of such gigantic fluctuations of momentum and energy, the average kinetic energy of these nuclei can remain invariably small and differ little from the thermal energy of the condensed target!

Another very important circumstance is the very long (compared to the case of uncorrelated states) lifetime of these giant fluctuations δt_{corr} , which is many orders of magnitude longer than the duration of possible uncorrelated fluctuations δt_{uncorr} , if it is estimated on the basis of the "usual" Heisenberg uncertainty relation $\delta t_{\text{uncorr}} \approx \hbar / 2\delta E$.

The possibility of the existence of such coherent correlated states was described in the most general form (for different pairs of arbitrary dynamical variables A and B) in 1930 independently by Schrödinger and Robertson [18,19] on the basis of the general rules of quantum mechanics. In the general case, these relations are characterized by generalized uncertainty relations for the variances of these variables

$$\sigma_A \sigma_B \equiv (\delta A)^2 (\delta B)^2 \geq \frac{|\langle [\hat{A}\hat{B}] \rangle|^2}{4(1 - r_{AB}^2)}, \quad \sigma_C = \langle (\hat{C} - \langle C \rangle)^2 \rangle, \\ r_{AB} = \frac{\sigma_{AB}}{\sqrt{\sigma_A \sigma_B}}, \quad \sigma_{AB} = \frac{\langle \hat{A}\hat{B} + \hat{B}\hat{A} \rangle - \langle A \rangle \langle B \rangle}{2}, \quad |r_{AB}| \leq 1. \quad (6)$$

In particular, for pairs of variables "coordinate-momentum" or "energy-time" these states are characterized by the Schrödinger-Robertson relations, which are fundamentally different from the Heisenberg uncertainty relations

$$\delta p \delta x \geq \hbar / 2\sqrt{1 - r_{px}^2} \equiv \hbar G_{px} / 2, \\ \delta E \delta t \geq \hbar / 2\sqrt{1 - r_{Et}^2} \equiv \hbar G_{Et} / 2, \quad (7)$$

where $0 \leq |r| < 1$ and $1 \leq G < \infty$ are, respectively, the correlation coefficient and the

correlation efficiency coefficient for specific variables. These coefficients characterize the degree of inphase and mutual correlation of different eigenstates of a particle in a superposition quantum state (in particular, inphase of optical phonon modes of a deuteron in the space between neighboring lithium atoms in the lattice). It was shown in [20] that the coefficients r_{px} , r_{Et} and G_{px} , G_{Et} for each specific state are very close to each other.

For uncorrelated states $r = 0$ and $G = 1$, and for maximally correlated $|r| \rightarrow 1$ and $G \gg 1$. The characteristics of these states and the possibility of their application have been studied in many works (in particular, in articles [11-17,20-22]).

Particles in a coherent correlated state can "use" a large fluctuation of virtual kinetic energy $\delta E = (\delta p)^2/2M$ to pass through a potential barrier and then stimulate nuclear or chemical reactions if these processes correspond to exoenergetic reactions.

Such processes have been implemented many times in successful experiments on low-temperature nuclear fusion. Some of these experiments are described in [11-13,23].

The same mechanism, realized by the pulse modulation of the parameters of local equivalent harmonic oscillators when exposed to a shock wave, successfully substantiates the results of experiments on the generation of alpha particles under the action of low-amplitude high-frequency temperature waves, generated during cavitation of water jets, on the TiD targets [24-26]. The general scheme of these experiments and the corresponding results on the registration of generated alpha particles are presented in **Fig. 2**.

These experiments, if we consider them as a kind of realization of systems with shock action, are in some way similar to experiments with pulsed laser action. The mechanism of such an effect in such a system is associated

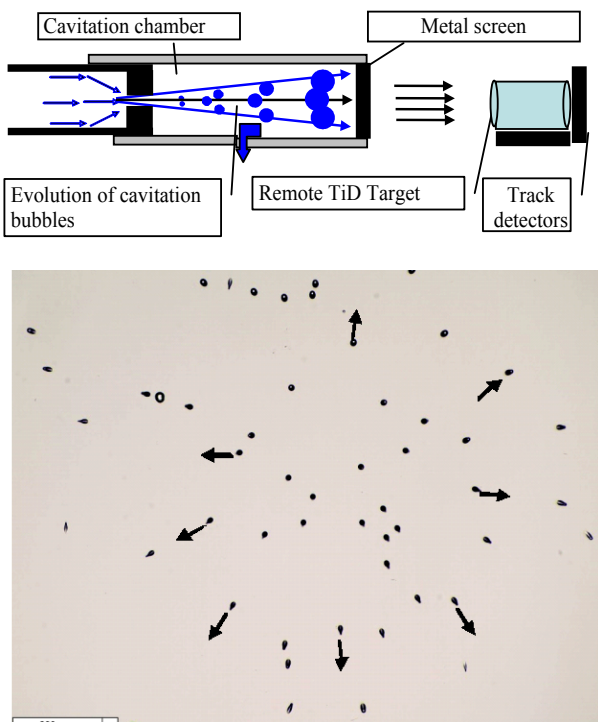


Fig. 2. Above is a diagram of experiments on the excitation of continuous temperature waves and the implementation of nuclear fusion using them. Below is a fragment of a track detector with tracks of alpha particles generated when such temperature waves act to a distant TiD target.

with the dynamics of the development of rapid cavitation of microbubbles in the volume of a water jet expanding after compression. The interaction of the jet in the state of cavitation with the metal wall of the chamber leads to the excitation of primary shock waves in the volume of this wall. Internal reflection of these waves from the outer wall leads to periodic excitation of surface atoms and, as a result, to the subsequent generation of both periodic pulses of soft (~ 1.5 keV) X-ray radiation and pulsed heating of the adjacent air. These processes are considered in details in [24-26].

If the duration of these heat pulses is less than the thermal relaxation time τ in air, then at such a pulsed heating continuous temperature waves will be generated and propagated in air. Their frequency corresponds to the expression

$$\omega_n = \pi(n + 1/2)/\tau, n = 0, 1, 2, \dots \quad (8)$$

The minimum frequency of such a wave at normal pressure and room temperature is $\omega_{min} \approx 75$ MHz.

The substantiation of the possibility of the existence of these waves and the results of their detailed theoretical and experimental study are considered in our works [24-26].

Such waves can propagate without significant attenuation over a long distance (up to many meters from the place of excitation). When these waves interact with a distant TiD target, secondary shock waves are excited in this target, which cause nuclear reactions with the participation of deuterons. Fig. 2 shows a view of the track detector, which was located near the rear wall of the TiD target obtained with preliminary enrichment ($\sim 150\%$) of the titanium sample with deuterium. The axial symmetry of the directions of motion of the registered alpha particles on this detector corresponded to the cylindrical shape of the TiD target. According to our estimates, the third possible channel of the d-d reaction was realized in these experiments

$$d + d = He^4 + 23.8 \text{ MeV}, \quad (9)$$

the probability of which for "standard" hot fusion is very small. In contrast, this channel is more likely to be implemented in the same systems based on LENR processes.

A more detailed description of these experiments is given in [15,24-26].

3.2. THE MECHANISM OF NUCLEAR FUSION AT LOW ENERGY, WHICH IS CONNECTED WITH THE MOVEMENT OF IONS IN THE CRYSTAL LATTICE OF THE TARGET

Another mechanism for the realization of reaction (1) is associated with an alternative method for the formation of CCS taking into account the interaction of moving ions with lattice atoms. It is due to the fact that in experiments [1,2] a great number of fast deuterium ions, which are formed during the formation of a laser plasma, move deep into

the unbroken crystal lattice of LiD in the channeling mode. It was shown in [16,17] that during a similar motion of relatively slow protons in the periodic field of the lattice of a lithium crystal, a similar CCS of a moving particle with a correlation coefficient $1 - |r| \leq 10^{-8}$ are formed very quickly (in an interval equal to 3 ... 4 lattice periods). It corresponds to the correlation efficiency coefficient $G \geq 10^4$ and to the increase of the energy of fluctuations in the transverse (with respect to longitudinal motion) direction to the value

$$\delta E \approx (\delta p)^2 / 2M \geq G^2 \hbar^2 / 8M(\delta x)^2 \approx G^2 \hbar^2 / 2Ma_x^2 \geq 40 \text{ keV}, \quad (10)$$

which is many orders of magnitude higher than the energy of longitudinal translational motion.

Here M is the proton mass, $a_x \approx 2\delta x \approx 2\text{\AA}$ is the interplanar distance in the lattice.

This mechanism of self-similar formation of CCS is fulfilled for those ions that move in the periodic field of the lattice with velocities close to the value $v_{opt} \approx 2a_z \langle \omega \rangle$, which provides synchronization of the eigenstates of the transverse quantized motion of the particle in the channel [16]. Here $\langle \omega \rangle$ is the average frequency of ion oscillations between planes during channeling in the averaged potential of the channel walls.

It was shown in [16] that a very large value of the coefficient G corresponds to particles with velocities in the range of approximately 10% of the optimal velocity v_{opt} for a given crystallographic direction. There are a lot of such particles with energies of several hundred eV on the "tail" of the Maxwellian distribution of laser plasma ions in experiments [1,2].

The spatial dynamics of the formation of CCS and the dependency of the correlation efficiency coefficient on the particle velocity in the lithium crystal lattice [16] is shown in **Fig. 3**.

The same dynamic mechanism of the CCS formation during the motion of an ion in a

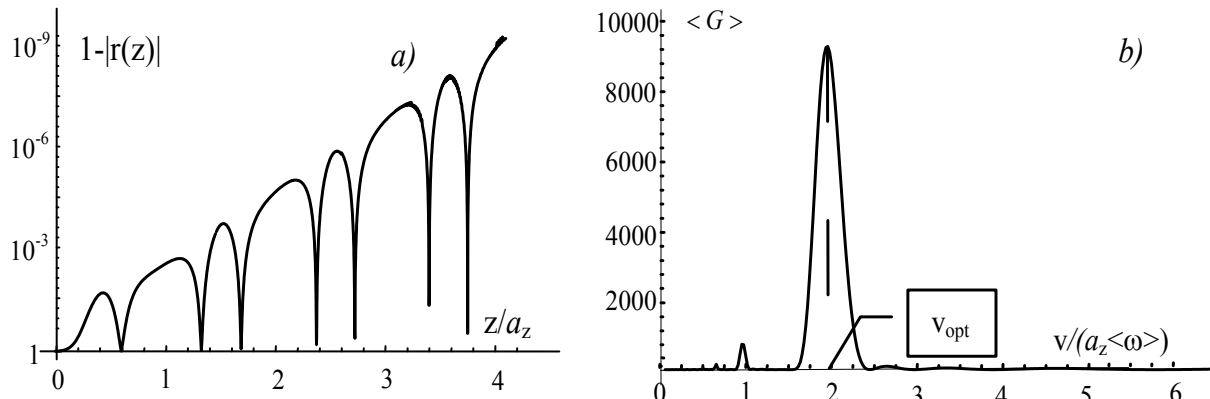


Fig. 3. a) spatial dynamics of the process of formation of a coherent correlated state during the motion of protons with an optimal energy of 450 ... 500 eV in a lithium crystal in the mode of in-plane channeling in the direction $o\bar{z}$ (a_z is the longitudinal lattice period of lithium); b) the dependence of the averaged correlation efficiency coefficient on the proton velocity at the end of the third lithium lattice period [16].

periodic field of a lattice or in the field of a cluster of several atoms explains well the results of numerous experiments carried out in several US laboratories (Louisiana Accelerator Center (Lafayette), Physical Dept. of North Texas Univ (Deuton) and NASA MFES Center in Huntsville). In these experiments a beam of accelerated protons with tunable energy $E \leq 500$ eV and two types of targets: a solid-state target in the form of a thin foil (~ 1 mm) of lithium and a target in the form of saturated vapors of the same lithium were used, as a result leading to efficient nuclear fusion (for details see [16,17]).

4. CONCLUSION

Both considered above mechanisms fully correspond to the definition of "nuclear reactions at low energy" or LENR, since they do not require heating or real (not virtual due to fluctuations) acceleration of particles to a typical thermonuclear energy of 10-15 keV and do not require the implementation of other conditions of hot thermonuclear fusion. It is very important that these types of reactions well substantiate the complete prohibition [14,20] on the realization of those channels of nuclear reactions that, after the fusion of the initial

particles, lead to the formation of radioactive compound nuclei. Such an extremely important result is differs greatly from typical reactions at high energies and, most importantly, is observed in all successful experiments at low energies without exception. A brief substantiation of such a feature of LENR reactions using the energy of giant fluctuations δE formed during the formation of coherent correlated states is due to the fact that a sufficiently long, but finite time of existence of these fluctuations δt_{corr} makes it possible to realize only those reaction channels in which a rapid return of the fluctuation energy δE , which was used to increase the transparency of the potential barrier, is realized. It is quite obvious that in any radioactive daughter nucleus such a return of energy occurs over a long time, which is many orders of magnitude greater than the value δt_{corr} and so such reactions are absolutely forbidden! In contrast, in reactions with really accelerated particles (including in systems of high-temperature nuclear fusion), there is no such a critical requirement, and in most reactions channels with the formation of both stable and radioactive nuclei are realized. These extremely important for practical applications

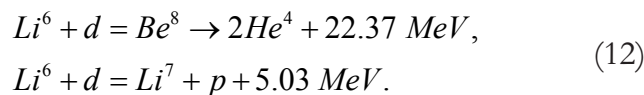
features of reactions with the use of CCS are considered in details in [20,23].

In addition to this, it should be noted that the analysis of experiments [1, 2] with the use of the CCS ideology also makes it possible to explain the relatively weak ($N_{neutron}^0 \approx 10$ neutron/pulse) efficiency of neutron generation, which was observed in these experiments. This is due to the fact that the neutron channel (dd) of the reaction $d + d = He^3 + n$, if we associate it with the formation of such CCS, turns out to be many orders of magnitude less probable [11,13] than the alternative and faster "proton" channel

$$d + d = T + p + 4.03 \text{ MeV}. \quad (11)$$

This is due to both the specificity (duration) of reactions stimulated by virtual energy fluctuations and the possible realization of the Oppenheimer-Phillips effect [27], which is connected with the mutual spatial reorientation of deuterons before their interaction, that leads to the capture reaction (4) without the formation of a compound nucleus He^4 .

It is also important to point out that if a LiD target is used in the analyzed earlier laser experiments, other reactions with the participation of lithium isotopes, in which alpha particles and protons are formed, are also possible.



Unfortunately, the authors of the first laser experiments [1,2] did not carry out control measurements of other potentially possible daughter products of these reactions, and these features remained unexplored and unnoticed.

Based on this analysis, it can be concluded that the most probable mechanism of neutron generation in the first laser experiments was associated not with the implementation of thermonuclear fusion, but with the implementation of nuclear reactions at low

energy due to the formation of coherent correlated states in the target volume under the action of a shock wave or during the motion of the formed ions in the undisturbed part of the target lattice [28].

The fact that such an analysis was not done 50 years ago is quite reasonable for a number of reasons. First of all, at that time some important circumstances, which relate to the peculiarities of nuclear reactions at high and low energies, were not understood and taken into account. Until recently, it was considered a priori that the region of low energies is completely unpromising from the point of view of nuclear energy based on charged particles. On the other hand, it is logically difficult to understand and accept the fact of completely ignoring of the influence of the effects of coherence and correlation on nuclear interaction, although the basic ideas of such effects were described back in 1930 in the works of Schrödinger and Robertson. In particular, as a completely inexplicable fact, it can be pointed out that none of the classical textbooks on quantum mechanics, on which all generations of physicists of the world were brought up in the 20th century, does not mention a word about such processes. In particular, nothing is written about the full ratio of the Schrödinger-Robertson uncertainties (6)-(7), from which, as a special case of an uncorrelated state, the famous Heisenberg uncertainty relation is obtained, which is well known and is used by everyone.

It should also be noted that the results obtained substantiate the possibility of alternative reactions in laser simulation of thermonuclear fusion. They show the advisability of a more detailed study and repetition of this and similar experiments in order to search for other possible nuclear fusion products using the same technique [1,2] at the action of unidirectional single or repetitive laser pulses. It is very important that such studies can be carried out in small laboratories and they do not require very complex, unique and expensive

equipment, which currently exists only in some world centers dealing with the solution of global problems of inertial thermonuclear fusion with mandatory all-round target compression by the time synchronized exposure to laser pulses generated by dozens of super-powerful lasers. Successful experiments on the implementation of nuclear fusion [24-26], carried out using temperature waves generated in a simple and extremely inexpensive cavitation setup based on a water jet, confirm the effectiveness of such studies.

Another conclusion concerns the need for a certain revaluation of the role and efficiency of nuclear reactions at low energy in order to solve modern problems of nuclear technologies [29-31]. Obviously, in order to solve successfully such problems, it is necessary to take into account not only the specific interaction between a pair of particles under consideration, as is the case in high-energy nuclear physics, but also to fully analyze the influence of the environment on the efficiency of these processes. The world turned out to be more complex and a simplified analysis based on the separated from the environment pair interaction works well at high energy, but turns out to be quite far from reality at low energy.

REFERENCES

- Basov NG, Zaharov SD, Kriukov PG, Senatskii YuV, Chekalin SV. Experiments on the observation of neutrons under the influence of powerful laser radiation focused on the surface of lithium deuteride. FIAN, Preprint №63 (1968) (in Russ.).
- Basov NG, Zaharov SD, Kriukov PG, Senatskii YuV, Chekalin SV. Experiments on the observation of neutrons by focusing high-power laser radiation on the surface of lithium deuteride. *JETP Letters*, 1968, 8(1):26 (in Russ.).
- Basov NG, Zaharov SD, Krokhan ON, Kriukov PG, Senatskii YuV, Tiurin EL, Fedosimov AI, Chekalin SV, Shchelev MY. Studies of plasma formed by ultrashort laser pulses. *Quantum electronics*, 1971, 1:4-28 (in Russ.).
- Basko MM. *Physical foundations of inertial thermonuclear fusion*. Moscow, ITEF Publ., 2008, 148 p.
- Burdonsky IN, Golsov AYu, Leonov AG, Makarov KN, Timofeev IS, Yufa VN. Shock wave generation in the high-power laser interaction with polycrystalline targets. *Problems of Atomic Science and Technology. Ser. Thermonuclear fusion*, 2013, 36(2):8-19 (in Russ.).
- Anisimov SI, Prokhorov AM, Fortov VE. The use of powerful lasers to study matter at ultrahigh pressures. *UFN*, 1984, 142(3):395-434.
- Fortov V. *High Energy Density Physics* (Section 4.3. Laser shock waves). Moscow, Fizmatlit Publ., 2013, 712 p.
- Mulser P, Bauer D. *High Power Laser-Matter Interaction*. Berlin Heidelberg, Springer, 2010.
- Mora P. Theoretical model of absorption of laser light by a plasma. *Phys. Fluids*, 1982, 25:1051-1056.
- Vysotskii VI, Adamenko SV. Correlated states of interacting particles and problems of the Coulomb barrier transparency at low energies in nonstationary systems. *Journ. of Tech. Physics*, 2010, 55(5):613-621.
- Vysotskii VI, Vysotskyy MV. Coherent correlated states and low-energy nuclear reactions in non stationary systems. *European Phys. Journ.*, 2013, A49(8):1-12.
- Vysotskii VI, Adamenko SV, Vysotskyy MV. Acceleration of low energy nuclear reactions by formation of correlated states of interacting particles in dynamical systems. *Annals of Nuclear energy*, 2013, 62:618-625.

13. Vysotskii VI, Vysotskyy MV. Coherent correlated states of interacting particles – the possible key to paradoxes and features of LENR. *Current Science*, 2015, 108(4):524.
14. Vysotskii VI, Vysotskyy MV. The formation of correlated states and tunneling at low energy at controlled pulse action on particles. *Journal of Experimental and Theoretical Physics*, 2017, 125(2):195-209.
15. Vysotskii VI, Vysotskyy MV. Universal mechanism of realization of nuclear reactions at low energy. *RENSIT*, 2017, 9(1)21-36. DOI: 10.17725/rensit.2017.9.021.
16. Vysotskii VI, Vysotskyy MV, Bartalucci S. Features of the formation of correlated coherent states and nuclear fusion induced by the interaction of slow particles with crystals and free molecules. *Journal of Experimental and Theoretical Physics*, 2018, 127:479-490.
17. Bartalucci Sergio, Vysotskii VI, Vysotskyy MV. Correlated states and nuclear reactions: An experimental test with low energy beams. *Phys. Rev. Accel. and Beams*, 2019, 22(5):054503.
18. Schrödinger E. Heisenbergschen Unschärfeprinzip. *Ber. Kgl. Akad. Wiss.*, 1939, 24:296.
19. Robertson HP. A general formulation of the uncertainty principle and its classical interpretation. *Phys. Rev. A*, 1930, 35:667.
20. Vysotskii VI, Vysotskyy MV. Features of correlated states and a mechanism of self-similar selection of nuclear reaction channels involving low-energy charged particles. *Journal of Experimental and Theoretical Physics*, 2019, 128(6):856-864.
21. Dodonov VV, Manko VI. Invariants and correlated states of nonstationary systems, in: Invariants and the Evolution of Nonstationary Quantum Systems. *Proceed. of the Lebedev Physical Institute*, 1987, 183:71-181 (in Russ.). [English translation: *Nova Science*, Commack, New York, v.183 (1988) 103–261].
22. Dodonov VV, Klimov AB, Manko VI. Physical effects in correlated quantum states, in: Squeezed and Correlated States of Quantum Systems. Proceed. of the Lebedev Physical Institute, 1991, 200:56-105 (in Russ.) [English translation: *Nova Science*, Commack, New York, 295 (1993) 61-107].
23. Vysotskii VI, Vysotskyy MV. Universal mechanism of LENR in physical and biological systems on the base of coherent correlated states of interacting particles. *Cold Fusion. Advances in Condensed Matter Nuclear Science*, Edited by Jean-Paul Biberian. Elsevier, 2020. Chapter 17, pp. 333-370.
24. Kornilova AA, Vysotskii VI, Sapochnikov YuA, Vlasova IE, Gaydamaka SN, Novakova AA, Avdukhina VM, Levin IS, VysotskyyMV, Khait EI, Volkova MH. The problem and implementation of stable generation of alpha particles by deuterated titanium in the field of a heat wave. *Engineering Physics*, 2018, 5:13-22 (in Russ.).
25. Kornilova AA, Vysotskii VI, Krit T, Vysotskyy MV, Gaydamaka SN. *Journal of Surface Investigation: X-ray, Synchrotron and Neutron Techniques*, 2020, 14(1)117-123.
26. Vysotskii VI, Vysotskyy MV, Kornilova AA, Krit TB, Gaydamaka SN, Hagelstein PL. Distant behind-screen action of undamped temperature waves. *Journal Condensed Matter Nucl. Science*, 2020, 33:296-304.
27. Vysotskii VI. The problem of creation a universal theory of LENR. *Infinite Energy*, 2013, 108(18):30-35.
28. Vysotskii VI, Kornilova AA, Vysotskyy MV. Features and mechanisms of the generation of neutrons and other particles in first laser fusion experiments. *Journal of*

Experimental and Theoretical Physics, 2020,
131:566-571.

29. Vysotskii VI, Adamenko SV, Vysotskyy MV. The formation of correlated states and the increase in barrier transparency at a low particle energy in nonstationary systems with damping and fluctuations. *Journal of Experimental and Theoretical Physics*, 2012, 115(4):551-556.
30. Vysotskii VI, Vysotskyy MV. Formation of correlated states and optimization of nuclear reactions for low-energy particles at nonresonant low-frequency modulation of a potential well. *Journal of Experimental and Theoretical Physics*, 2015, 120(2):246-256.
31. Kornilova AA, Vysotskii VI, Sysoev NN, Litvin NK, Tomak VI, Barzov AA. Intense X-ray generated at the output of fast water jets from the metal channel into the atmosphere. *Journal of Surface Investigation: X-ray, Synchrotron and Neutron Techniques*, 2010, 12:53-63 (in Russ.).

DOI: 10.17725/rensit.2021.13.071

The study of dynamical processes in problems of mesofracture layers exploration seismology by methods of mathematical and physical simulation

Maxim V. Muratov, Polina V. Stognii, Igor B. Petrov, Alexey A. Anisimov, Nazim A. Karaev

Moscow Institute of Physics and Technology, <https://mipt.ru/>

Dolgoprudny 141701, Moscow region, Russian Federation

E-mail: max.muratov@gmail.com, stognii@phystech.edu, petrov@mipt.ru, nazim_karaev@mail.ru

Received December 19, 2020, peer-reviewed December 24, 2020, accepted December 29, 2020

Abstract. The article is devoted to the study of the propagation of elastic waves in a fractured seismic medium by methods of mathematical modeling. The results obtained during it are compared with the results of physical modeling on similar models. For mathematical modeling, the grid-characteristic method with hybrid schemes of 1-3 orders with approximation on structural rectangular grids is used. The ability to specify inhomogeneities (fractures) of various complex shapes and spatial orientations has been implemented. The description of the developed mathematical models of fractures, which can be used for the numerical solution of exploration seismology problems, is given. The developed models are based on the concept of an infinitely thin fracture, the size of the opening of which does not affect the wave processes in the fracture area. In this model, fractures are represented by boundaries and contact boundaries with different conditions on their surfaces. This approach significantly reduces the need for computational resources by eliminating the need to define a mesh inside the fracture. On the other hand, it allows you to specify in detail the shape of fractures in the integration domain, therefore, using the considered approach, one can observe qualitatively new effects, such as the formation of diffracted waves and a multiphase wavefront due to multiple reflections between the surfaces, which are inaccessible for observation when using effective fracture models actively used in computational seismic. The obtained results of mathematical modeling were verified by physical modeling methods, and a good agreement was obtained.

Keywords: mathematical modeling, grid-characteristic method, physical modeling, elastic waves, exploration seismology, fractured media, mesofractures

UDC 004.94

Acknowledgments: This work was supported by the Russian Foundation for Basic Research, Grant No. 19-01-00432.

For citation: Maxim V. Muratov, Polina V. Stogniy, Igor B. Petrov, Alexey A. Anisimov, Nazim A. Karaev. The study of dynamical processes in problems of mesofracture layers exploration seismology by methods of mathematical and physical simulation. *RENSIT*, 2021, 13(1):71-78. DOI: 10.17725/rensit.2021.13.071.

CONTENTS

1. INTRODUCTION (72)	c) GLUED FRACTURE (74)
2. MATERIALS AND METHODS (72)	d) PARTIALLY-GLUED FRACTURE (74)
2.1. MATHEMATICAL MODEL AND NUMERICAL METHOD (72)	2.3. INSTALLATION FOR PHYSICAL MODELING (74)
2.2. MATHEMATICAL MODELS OF FRACTURES (73)	2.4. FRACTURED LAYER PHYSICAL MODELING TECHNOLOGY (74)
a) GAS-SATURATED FRACTURE (73)	2.5. METHODOLOGY FOR COMPARING THE RESULTS OF MATHEMATICAL AND PHYSICAL MODELING (75)
b) FLUID-FILLED FRACTURE (73)	

3. RESULTS (75)

3.1. FORMULATION OF THE PROBLEM (75)

3.2. RESULTS OF MATHEMATICAL AND PHYSICAL SIMULATION (75)

4. CONCLUSION (77)

REFERENCES (77)

1. INTRODUCTION

The problem of searching for fractured hydrocarbon reservoirs is one of the primary problems of geophysics, to the solution of which exploration seismology is involved [1,2]. The widespread use of traditional seismic technologies without sufficient justification for their application to unconventional seismic objects in many cases leads to ambiguous geological interpretation of seismic data, false ideas about the geological structure of the target object. The combined use of mathematical and physical modeling can improve the quality of seismic data interpretation.

Papers [3-6] are devoted to different approaches to fracture modeling. According to [7], several types of fractures are distinguished, depending on their size: microfractures, the opening of which is about tens of microns, and the length is several centimeters; mesofractures with an opening of the order of hundreds of microns, with a length of up to several meters, and macrofractures, the opening of which reaches the order of several millimeters or more, and the length – from tens to hundreds of meters.

For modeling microfracturing, the most optimal will be the use of effective models [8,9]. Meso- and macro-fracturing can be considered in more detail with discrete assignment of fractures in the integration domain. Papers [10,11] are devoted to the study of the formation of responses on macrofractures using this approach. This article will consider studies using mathematical and physical modeling of the formation of responses in mesofractures.

2. MATERIALS AND METHODS

2.1. MATHEMATICAL MODEL AND NUMERICAL METHOD

For mathematical modeling, a linear elastic medium model is used. The computation uses a grid-characteristic method with a hybrid scheme of the 2nd order.

Wave processes in an elastic geological medium are described on the basis of the governing equations of the theory of a linearly elastic medium [12]. The state of an infinitely small volume of a medium, according to this model, obeys a system of two equations: a local equation of motion and a rheological relationship connecting stresses and deformations in the medium. They can be reduced to the form:

$$\rho \frac{\partial V_i}{\partial t} = \frac{\partial T_{ji}}{\partial x_j},$$

$$\frac{\partial T_{ij}}{\partial t} = \lambda \left(\sum_k \frac{\partial V_k}{\partial x_k} \right) I_{ij} + \mu \left(\frac{\partial V_i}{\partial x_j} + \frac{\partial V_j}{\partial x_i} \right). \quad (1)$$

where V_i – velocity components, T_{ji} – components of elastic tensor, ρ – medium density, λ and μ – Lame coefficients, I_{ij} – components of unit vector. Introducing the vector of variables $u = \{V_x, V_y, T_{xx}, T_{yy}, T_{xy}\}$, (1) can be reduced to:

$$\frac{\partial \vec{u}}{\partial t} + \sum_{i=1,2} A_i \frac{\partial \vec{u}}{\partial \xi_i} = 0. \quad (2)$$

The numerical solution (2) is found using the grid-characteristic method [13]. We carry out the coordinate-wise splitting and change the variables to reduce the system to a system of independent scalar transport equations in Riemann invariants.

$$\frac{\partial \vec{w}}{\partial t} + \Omega_i \frac{\partial \vec{w}}{\partial \xi'_i} = 0, \quad i = 1, 2. \quad (3)$$

For each transfer equation (3), all nodes of the computational mesh are traversed, and for each node the characteristics are omitted. From the time layer n , the corresponding component

of the vector \vec{w} is transferred to the time layer $n+1$ by the formula

$$w_k^{n+1}(\xi_i) = w_k^n(\xi_i - \omega_k \tau),$$

where τ is time step.

After all the values have been transferred, there is a reverse transition to the vector of the desired values \vec{u} .

The grid-characteristic method makes it possible to apply the most correct algorithms at the boundaries and contact boundaries of the integration domain [14,15].

The boundary condition can be written in general form as:

$$D\vec{u}(\xi_1, \xi_2, t+\tau) = \vec{d},$$

where D – some matrix of size 9×3 in $3D$ -case (5×2 in $2D$ -case), \vec{d} – some vector, u $\vec{u}(\xi_1, \xi_2, t+\tau)$ – the value of the sought values of the velocity and the stress tensor components at the boundary point at the next time step.

2.2. MATHEMATICAL MODELS OF FRACTURES

In real problems of exploration seismology, one has to deal with the inhomogeneity of the nature of the interaction of elastic waves with the surface of the fracture when passing through it. A fracture is a complex heterogeneous structure [7,16]. In some places, the flaps of the fractures are located at some distance and are separated by a saturating fluid or void [7], in some places adhesion is observed, when, under the action of pressure forces, the walls are close to each other [17]. In addition, fractures can be classified according to the nature of saturation: fluid or gas [7,17].

In the problem under consideration, discrete fracture models were used based on the concept of an infinitely thin fracture. The fracture was specified as a boundary or a contact boundary with a specific boundary condition.

a) GAS-SATURATED FRACTURE

The gas-saturated fracture model well simulates the behavior of fractures filled with air or gas

at shallow depths up to 100-150 m [17]. At great depths, under the influence of pressure, fractures with air are closed, and the gas acquires the properties of a liquid.

The fracture is specified as the boundary condition of free reflection on the fracture flaps:

$$\mathbf{T}\vec{n} = 0.$$

This model is applicable to the described situation. The speed of propagation of longitudinal elastic waves in the geological environment (1500 – 7000 m/s) is much higher than the sound speed in air (330 m/s) or natural gas (430 m/s) at low pressures. The speed of propagation of transverse waves in air is zero. Similarly, with densities (1000-3000 kg/m³ versus 1.2 kg/m³). Therefore, the reflection coefficient is approximately equal to unity.

Thus, a fracture filled with gas under a pressure close to normal can be considered empty and the boundary condition for a free boundary can be set, which gives a complete reflection of the incident wave.

b) FLUID-FILLED FRACTURE

In most of the problems solved in practice, the fractures are filled with a fluid: water, oil, liquefied gas, etc. [7,11,17] Therefore, it was advisable to develop a model to describe such a situation.

A fluid-filled fracture is specified as a contact boundary with the condition of free sliding [11]:

$$\vec{v}_a \cdot \vec{n} = \vec{v}_b \cdot \vec{n}, \quad \vec{f}_n^a = -\vec{f}_n^b, \quad \vec{f}_\tau^a = \vec{f}_\tau^b = 0.$$

Such a contact boundary completely transmits longitudinal vibrations without reflection and completely reflects shear waves. This picture corresponds to a real situation: the values of the velocities of propagation of longitudinal waves in liquids and densities are comparable to the values of the velocities and densities of geological media; while the velocities of transverse vibrations in liquids are close to zero.

c) GLUED FRACTURE

At great depths, under the action of pressure, it happens that the flaps of the fractures touch so that the elastic waves almost completely pass through the fracture. In this case, it will be optimal to use the contact condition of complete adhesion [11]:

$$\vec{v}_a = \vec{v}_b, \quad \vec{f}_a = -\vec{f}_b.$$

where \vec{v} – the velocities of contacted points of contact boundaries, \vec{f} – the force acting to the boundary. a – first, and b – second flap of fracture.

d) PARTIALLY-GLUED FRACTURE

In real exploration seismology, there are partially stuck together fractures [11,17], in which part of the valve surface is stuck together, and part is separated by fluid or gas. Such fractures show partial transmission of the elastic wave front, which affects the amplitudes of the response waves on the seismograms.

A fracture model was developed, where gas saturation (fluid filling) and complete adhesion conditions were randomly set at different points of the valves. The number of certain points was regulated by a weighting coefficient – the gluing coefficient. Such a model made it possible to define gas-saturated and fluid-filled fractures with a percentage of glued points from 0 to 100%.

Since at some points the fracture reflects the wave front, and at others it passes, the superposition of scattered waves formed during interaction with all points is a response of a gas-saturated (fluid-filled) fracture with a lower amplitude.

2.3. INSTALLATION FOR PHYSICAL MODELING

To conduct research on physical models within the framework of this topic, an installation for ultrasonic seismic modeling (IUSM) is used. The installation is made according to a single-channel scheme and includes:

- a source of elastic vibrations from piezoceramics;
- receiver of elastic vibrations from piezoceramics;
- generator of exciting electrical impulses;

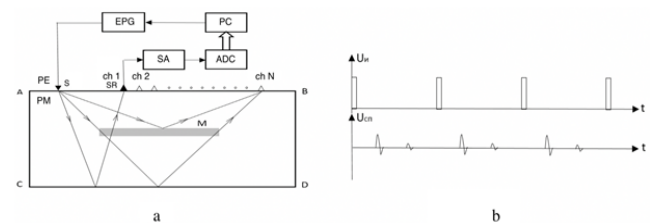


Fig. 1. Functional scheme (a) and timing diagrams (b) of the setup for ultrasonic seismic modeling of the IUSM.

- seismic amplifier;
- analog-to-digital converter;
- personal computer - a controller that controls all system nodes and stores simulation results.

The functional scheme of the IUSM is shown in **Fig. 1**.

An exciting pulse generator (EPG) generates voltage in the form of a sequence of short pulses. The source of seismic waves (S), connected to the EPG output, emits elastic vibrations - seismic waves - into the medium of the physical model (PM). Seismic waves of various types propagating in the medium are recorded by a seismic receiver (SR), which sequentially moves along the points (ch 1 - ch N) of the seismic profile. The signal from the seismic receiver (SR) output is amplified by the seismic amplifier (SA) to the required level and converted by an analog-to-digital converter (ADC) into digital form. Registration, processing of digital signals, recording in the standard seismic SEG-Y format and control of the system as a whole are performed using a personal computer (PC).

By moving the source and the seismic receiver along the given points of the seismic profile, it is possible to form a given observation system. The data is accumulated in the form of n-channel seismograms and can be processed according to the standard processing graphs used in exploration seismology.

2.4. FRACTURED LAYER PHYSICAL MODELING

TECHNOLOGY

The physical model was made from a sheet of plexiglass with dimensions of $1640 \times 800 \times 4$ mm and simulates a homogeneous environment in

which the investigated mesofractured layer of a given shape and given physical parameters is located. With the coefficient of geometric similarity $K = 4000$, it is possible to simulate a geological section with a size of 6560×3200 m. The IUSM installation uses signals with a signal frequency of the order of 40-50 kHz. Seismic waves propagate in a medium with velocities of longitudinal and shear waves $V_p = 2200-2400$ m/s и $V_s = 1200-1300$ m/s. Accordingly, seismic waves with a wavelength of $\lambda = 5-6$ cm.

In Fig. 1a, the side of the sheet AB corresponds to the surface, and the side AC corresponds to the depth. The CD side ("bottom" of the model) can be used as a very contrasting reference horizon. Taking into account the similarity coefficient $K = 4000$, the ultrasonic frequency signals are transformed into the low-frequency region with prevailing frequencies of the order of 10-12 Hz.

2.5. METHODOLOGY FOR COMPARING THE RESULTS OF MATHEMATICAL AND PHYSICAL MODELING

Both mathematical and physical simulation results are saved in the standard seismic SEG-Y format. The obtained data are processed in order to quantitatively compare the results. For a qualitative comparison of the results, visualization is performed in the form of seismograms in the SeiSee program.

3. RESULTS

3.1. FORMULATION OF THE PROBLEM

The problem of studying wave responses from a system of uniformly oriented mesofractures located at a depth of 1640 m is considered. The horizontal length of the formation is 2800 m, the vertical length is 120 m. The fractures are evenly distributed in the formation. The height of the fractures is 12 m, the distance between them is 12 m, the angle of inclination is 5 degrees. The observation scheme is shown in Fig. 2.

An excitation point is used, located on the day surface, its horizontal position coincides with

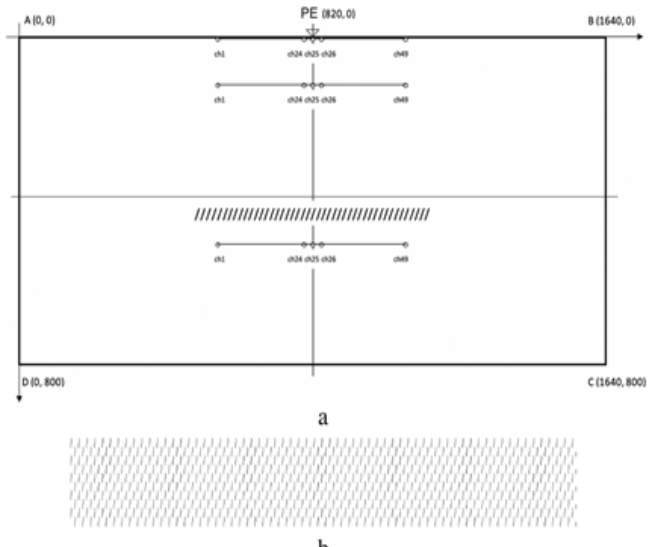


Fig. 2. Observation scheme (a), detailing the picture of the location of fractures in the reservoir (b).

the center of the fracture layer. The frequency of the excited seismic pulse is 10 Hz.

Three observation profiles are used, on which wave responses are recorded in the form of seismograms:

- 1) Reception points ch-1 – ch-49 are located on the day surface with an interval of 40 m to the right and left of the source, 24 sensors each. ch-1 – ch-49 sensors are located from left to right. ch-25 is combined with the excitation point.
- 2) Reception points ch-1 – ch-49 are located at a depth of 400 m with an interval of 40 m to the right and left of the source with 24 sensors each. ch-1 – ch-49 sensors are located from left to right. ch-25 is under the excitation point.
- 3) Reception points ch-1 – ch-49 are located at a depth of 2000 m with an interval of 40 m to the right and left of the source, 24 sensors each. ch-1 – ch-49 sensors are located from left to right. ch-25 is under the excitation point.

3.2. RESULTS OF MATHEMATICAL AND PHYSICAL SIMULATION

The solution to the problem was carried out jointly by the methods of mathematical and physical modeling. The results are shown in the figures – for mathematical modeling on the left, for physical – on the right. A fairly good agreement is seen.

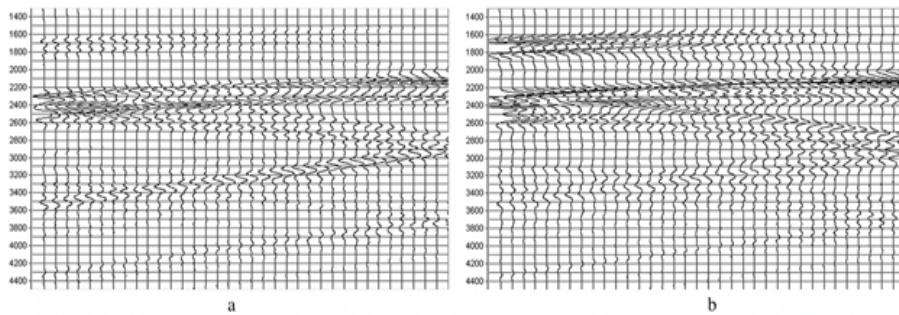


Fig. 3. Results in the form of seismograms for the horizontal component, obtained using mathematical (a) and physical (b) modeling for the profile located on the surface.

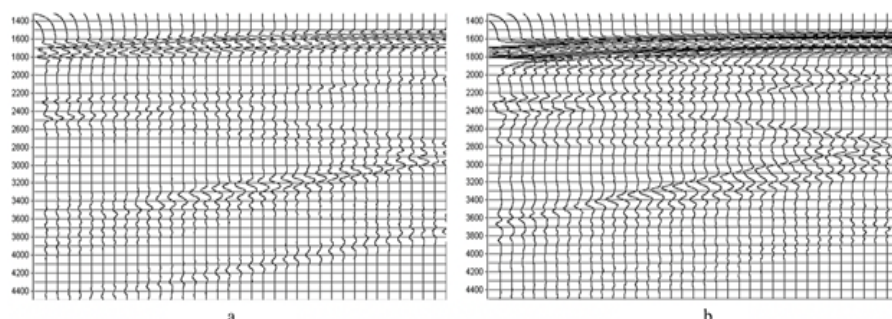


Fig. 4. Results in the form of seismograms for the vertical component, obtained using mathematical (a) and physical (b) simulations for the profile located on the surface.

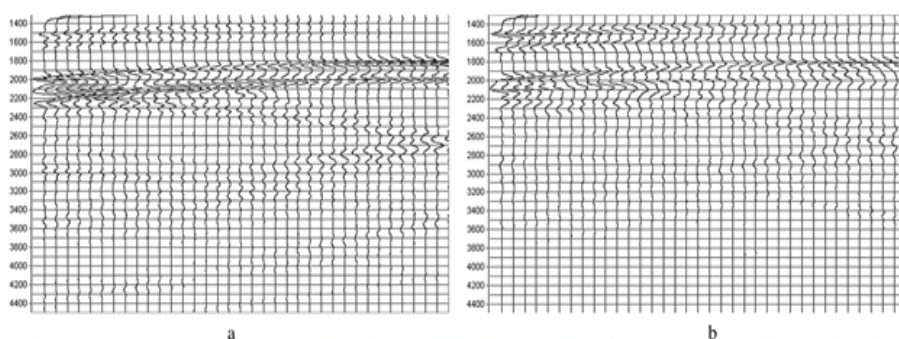


Fig. 5. Results in the form of seismograms for the horizontal component obtained using mathematical (a) and physical (b) modeling for a profile at a depth of 400 m.

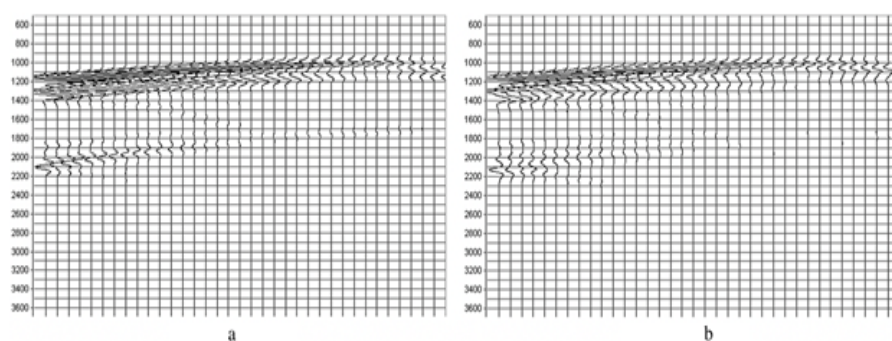


Fig. 6. Results in the form of seismograms for the vertical component obtained using mathematical (a) and physical (b) modeling for a profile at a depth of 400 m.

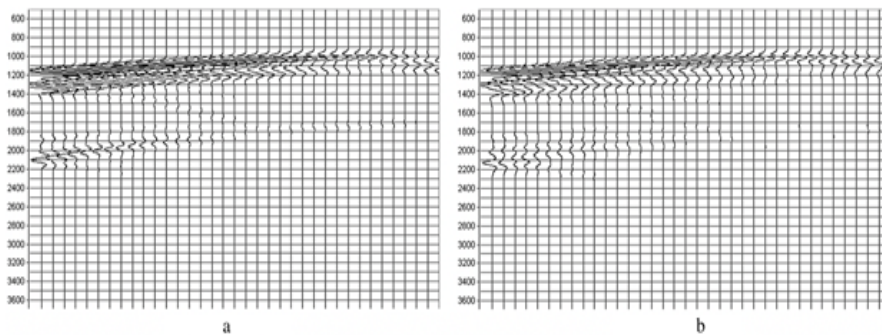


Fig. 7. Results in the form of seismograms for the horizontal component obtained using mathematical (a) and physical (b) modeling for a profile at a depth of 2000 m.

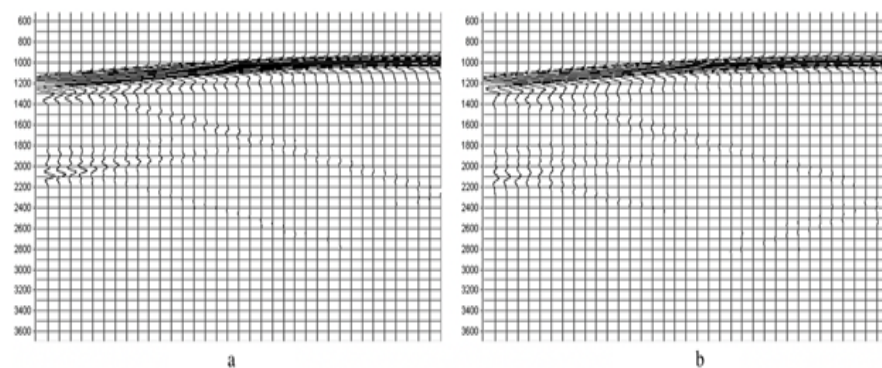


Fig. 8. Results in the form of seismograms for the vertical component obtained using mathematical (a) and physical (b) modeling for a profile at a depth of 2000 m.

4. CONCLUSION

The developed technique, based on the grid-characteristic method, makes it possible to carry out mathematical modeling for seismic exploration problems in layers of uniformly oriented mesofractures. Several fracture models based on the concept of an infinitely thin fracture have been developed to simulate heterogeneities with different types of saturation: gas-saturated, fluid-saturated, glued and partially glued gas-saturated and fluid-saturated fractures.

Numerical modeling of the problem of seismic prospecting of a layer of mesofractures in a formulation close to the real one with registration of wave responses in three receiver profiles is carried out. A similar problem was solved using physical modeling, the results of which verified the results of mathematical modeling.

REFERENCES

1. Sheriff RE, Geldart LP. *Exploration seismology*. Cambridge University Press, 1995, 592 p.
2. Braduchan YuV, Goldberg AV, Gurari FG. *Bazhenovskii gorizont Zapadnoi Sibiri* [Bazhen horizon of West Siberia]. Novosibirsk, Nauka Publ., 1986, 216 p.
3. Khokhlov N, Stognii P. Novel approach to modeling the seismic waves in the areas with complex fractured geological structures. *Minerals*, 2020, 10(2):122.
4. Nikitin IS, Burago NG, Golubev VI, Nikitin AD. Methods for Calculating the Dynamics of Layered and Block Media with Nonlinear Contact Conditions. *Smart Innovation, Systems and Technologies*, 2020, 173:171-183.
5. Cui X, Lines LR, Krebes ES. Seismic Modelling for Geological Fractures. *Geophys. Prospect.*, 2018, 66:157-168.
6. Chentsov EP, Sadovskii VM, Sadovskaya OV. Modeling of wave processes in a

- blocky medium with fluid-saturated porous interlayers. *AIP Conference Proceedings*, 2017, 1895:080002.
7. Leviant VB, Petrov IB, Kvasov IE. Chislennoe modelirovanie volnovogo otklika ot subvertikalnykh makrotreschin, veroyatnykh fluidoprovodyaschikh kanalov [Numerical modeling of seismic response from subvertical macrofractures as possible fluid conduids]. *Tekhnologii seismorazvedki*, 2011, 4:41-61 (in Russ.).
 8. Bakulin A, Grechka V, Karaev N, Anisimov A, Kozlov E. Physical modeling and theoretical studies of seismic reflections from a fault zone. *SEG*, 2004, 1674-1677.
 9. Willis ME, Burns DR, Rao R, Minsley B, Toksöz MN, Vetri L. Spatial orientation and distribution of reservoir fractures from scattered seismic energy. *Geophysics*, 2006, 71(5):43-51.
 10. Leviant VB, Petrov IB, Muratov MV. Chislennoe modelirovanie volnovikh otklikov ot sistemy (klastera) subvertikalnykh makrotreschin [Numerical simulation of wave responses from subvertical macrofractures system]. *Tekhnologii seismorazvedki*, 2012, 1:5-21 (in Russ.).
 11. Petrov IB, Muratov MV. Application of the Grid-Characteristic Method to the Solution of Direct Problems in the Seismic Exploration of Fractured Formations (Review). *Mathematical Models and Computer Simulations*, 2019, 11:924-939.
 12. Novatskii VK. *Teoriya uprugosti* [Elastic theory]. Moscow, Mir Publ., 1975, 872 p.
 13. Magomedov KM, Kholodov AS. Setochno-kharakteristicheskie chislennye metody [Grid-characteristic numerical methods]. Moscow, Nauka Publ., 1988, 288 p.
 14. Petrov IB, Tomasov AG, Kholodov AS. On the use of hybrid grid-characteristic schemes for the numerical solution of three-dimensional problems in the dynamics of a deformable solid. *USSR Computational Mathematics and Mathematical Physics*, 1990, 30(4):191-196.
 15. Favorskaya AV, Breus AV, Galitskii BV. Application of the grid-characteristic method to the seismic isolation model. *Smart Innovation. Systems and Technologies*, 2019, 133:167-181.
 16. Kozlov EA. *Modeli sredy v razvedochnoi seismologii* [Models of medium in exploration seismology]. Tver, GERS Publ., 2006, 480 p.
 17. Leviant VB, Miryakha VA, Muratov MV, Petrov IB. Otsenka vliyaniya na seismicheskii otklik raskrytosti treschiny i doli ploschadi lokalnykh kontaktov k ee poverkhnosti [Seismic responses of vertical fractures depending on their thickness]. *Tekhnologii seismorazvedki*, 2015, 3:16-30 (in Russ.).

DOI: 10.17725/rensit.2021.13.079

Mathematical modeling of temperature changes impact on artificial ice islands

Maxim V. Muratov, Vladimir A. Biryukov, Denis S. Konov, Igor B. Petrov

Moscow Institute of Physics and Technology, <https://mipt.ru/>

Dolgoprudny 141701, Moscow region, Russian Federation

E-mail: max.muratov@gmail.com, biryukov.vova@gmail.com, konov1999@gmail.com, petrov@mipt.ru

Received December 21, 2020, peer-reviewed December 26, 2020, accepted December 29, 2020

Abstract: The article is devoted to the numerical solution of the Stefan problem for thermal effects on an artificial ice island. For modern tasks of the development of the Arctic, associated with the exploration and production of minerals, it is important to create artificial ice islands in the Arctic shelf, due to the speed of their construction, economic feasibility and other factors. The most important task for the exploitation of such islands is their stability, including against melting. This paper discusses the issue of the stability of ice islands to melting. For this, the Stefan problem on the change in the phase state of matter is formulated. An enthalpy solution method is constructed, and the applicability of this method is considered. For the numerical solution, the Peasman-Reckford scheme is used, which is unconditionally spectrally stable in the two-dimensional case, which allows to freely choose the time step. In addition, the developed approach takes into account the flow of water and the flow of melted water, which is important in the task at hand. The developed computational algorithms are parallelized for use on modern multiprocessor computing systems. An approach is implemented for modeling thermal processes in the thickness of an arbitrary mass of substances, taking into account arbitrary initial conditions, environmental conditions, tidal currents of water, and solar radiation. This approach was used to calculate the temperature distribution in the thickness of the ice island, as well as to study the impact of seasonal temperature changes on the stability of the island.

Keywords: mathematical modeling, ice island, Stefan problem, enthalpy method, Peasman-Rechford scheme

UDC 004.94

Acknowledgments: The work was carried out within the framework of the project of the Russian Science Foundation No. 19-11-00023.

For citation: Maxim V. Muratov, Vladimir A. Biryukov, Denis S. Konov, Igor B. Petrov. Mathematical modeling of temperature changes impact on artificial ice islands. *RENSIT*, 2021, 13(1):79-86. DOI: [10.17725/rensit.2021.13.079](https://doi.org/10.17725/rensit.2021.13.079).

CONTENTS

- 1. INTRODUCTION (80)**
- 2. MATERIALS AND METHODS (80)**
 - 2.1. MATHEMATICAL MODEL (80)**
 - 2.2. NUMERICAL METHOD (81)**
 - 2.3. SOFTWARE IMPLEMENTATION (81)**
- 3. RESULTS (82)**
 - 3.1. PROBLEM FORMULATION (82)**
 - 3.2. THE RESULTS OF MODELING THE PROBLEM IN THE FORMULATION WITHOUT TAKING INTO ACCOUNT WATER FLOW AND SOIL FREEZING (82)**

3.3. THE RESULTS OF MODELING THE PROBLEM IN THE FORMULATION TAKING INTO ACCOUNT THE WATER FLOW AND WITHOUT SOIL FREEZING (83)

3.4. THE RESULTS OF MODELING THE PROBLEM IN THE FORMULATION TAKING INTO ACCOUNT THE FLOW OF WATER AND SOIL FREEZING (84)

- 4. CONCLUSION (84)**
- REFERENCES (85)**

1. INTRODUCTION

Modern tasks of the development of the Arctic set new requirements for the offshore infrastructure facilities. Artificial ice islands provide a low-cost and environmentally friendly alternative to conventional drilling platforms for oil and gas production in the Arctic. The approach has already been successfully implemented in Canada [1]. Ice islands and their advantages in the development of the Arctic are considered in [2]. In [3], a numerical solution of the problems of stability of ice islands to elastic impact was carried out. But during operation, in addition to mechanical stability, it is necessary to take into account resistance to thermal influences (melting of an ice island). To correctly solve the problem of stability of an ice island to static and dynamic elastic effects, it is necessary to know the temperature distribution inside the ice island. It is also important to study the island's resistance to seasonal temperature fluctuations. Approaches for taking into account climatic impacts on the ice island were considered in [4-6].

This article proposes an approach to numerical modeling of the melting of ice islands, based on solving the problem of the evolution of a system with different phase states of matter and changing the location of the boundary between these phases - Stefan's problem [7-12]. The works [13-16] are devoted to the numerical solution of problems with phase transitions. In [13,14], the method of lines was considered. The finite element method and finite difference methods are also often used in practice [15,16].

In this work, the enthalpy approach is used [17]. For this, the task is reduced to the function of heat content. The developed approach also takes into account water flow, melted water runoff, and other important phenomena. With its help, it was possible to obtain the temperature distributions in the ice island, as well as to conduct a study on resistance to seasonal temperature fluctuations.

2. MATERIALS AND METHODS

2.1. MATHEMATICAL MODEL

Consider a three-dimensional computational domain of arbitrary volume V . Let us write down the first law of thermodynamics and pass from internal energy to enthalpy:

$$\delta Q = dH - VdP, \quad (1)$$

where δQ – heat flow, dH – enthalpy change, V – volume of matter, dP – pressure change. For sufficiently slow (practically equilibrium) processes with constant pressure, one can (1) takes the form:

$$\delta Q = dH. \quad (2)$$

Enthalpy is a function of state. Let us select in the computational domain a small element of volume V . For it, the first law of thermodynamics can be rewritten as:

$$-\int_{S=\partial V} \vec{q} \cdot d\vec{S} = \int_V \frac{\partial H}{\partial t} dV, \quad (3)$$

where \vec{q} – heat flow per unit area. Using Gauss's theorem, we turn to the continuity equation for heat:

$$\operatorname{div}(\vec{q}) + \frac{\partial H}{\partial t} = 0. \quad (4)$$

Applying the Fourier thermal conductivity formula, we obtain from (4):

$$\vec{\nabla}(-k(H,x,y,z)\vec{\nabla}T) + \frac{\partial H}{\partial t} = 0, \quad (5)$$

where $k(H,x,y,z)$ – coefficient of thermal conductivity, which depends on the substance and its phase state.

Let's introduce the function of heat content:

$$Q = \begin{cases} \rho_s C_s T, & T < T_0, \\ \rho_L C_L (T - T_0) + \rho_s C_s T_p + \rho_s \lambda, & T > T_0, \end{cases} \quad (6)$$

where ρ_s and C_s – density and specific heat of solid, and ρ_L and C_L – ones of liquid state, T_0 – the phase transition temperature, λ – specific heat of fusion in a given volume.

The inverse transition to temperature is possible by the formula:

$$T = \begin{cases} Q \cdot \rho_s^{-1} C_s^{-1}, & Q < \rho_s C_s T_s = Q_-, \\ T_0, & Q_- < Q < Q_+, \\ \frac{Q + (\rho_L C_L - \rho_s C_s) T_0 - \rho_s \lambda}{\rho_L C_L}, & Q > \rho_s C_s T_s + \rho_s \lambda = Q_+, \end{cases} \quad (7)$$

where \mathcal{Q}_- and \mathcal{Q}_+ – limits of the value of heat content at the phase transition temperature.

We believe that the thermophysical constants are determined by the substance, which is constant at a given point. Note that mapping (6) is not continuous with respect to temperature. This correlates with the fact that at the melting point, a substance can be in different phase states.

Enthalpy and heat content coincide up to a constant. Substitute expressions (6) and (7) into (5) and obtain a hyperbolic equation for the evolution of the system through the heat content:

$$\frac{\partial}{\partial x} \left(k(Q) \frac{\partial T}{\partial x} \right) + \frac{\partial}{\partial y} \left(k(Q) \frac{\partial T}{\partial y} \right) + \frac{\partial}{\partial z} \left(k(Q) \frac{\partial T}{\partial z} \right) = \frac{\partial H}{\partial t}. \quad (8)$$

Note that the thermal conductivity coefficients also depend on the coordinate of the point, but in our model, at each point, the substance remains constant and only its phase state changes, so this dependence is not reflected in this equation.

The value of thermal conductivity $k(Q)$ for each phase of the substance is known. For intermediate values, during phase transitions, for thermal conductivity, we can write:

$$k(Q) = \begin{cases} k_s, & Q < Q_-, \\ k_s + (k_L - k_s) \cdot \frac{Q - Q_-}{Q_+ - Q_-}, & Q_- < Q < Q_+, \\ k_L, & Q > Q_+, \end{cases}$$

where k_s – thermal conductivity of a solid state of matter, k_L – thermal conductivity of a liquid state.

2.2. NUMERICAL METHOD

For the numerical solution of equation (8), the Peasman-Reckford scheme (in the two-dimensional case, referred to as the longitudinal-transverse scheme) [18,19] was chosen since it showed the best results in terms of operating speed. In the two-dimensional case, it is unconditionally spectrally stable, which makes it possible to freely choose the time step, but at the same time it can be solved in a time linear in the number of nodes. The computation is carried

out in two steps: during the first, the scheme is explicit in one direction, and implicit in the second; during the second step, the directions change:

$$\begin{aligned} \frac{2\Delta V}{\tau} \left(Q^{j+1} - Q^{j+\frac{1}{2}} \right) &= \Lambda_x Q^{j+\frac{1}{2}} + \Lambda_y Q^{j+1}, \\ \Lambda_x Q_{i_x, i_y} &= k_{i_x, \frac{1}{2}} \frac{T(Q_{i_x+1, i_y}) - T(Q_{i_x, i_y})}{h_x} + k_{i_x, -\frac{1}{2}} \frac{T(Q_{i_x-1, i_y}) - T(Q_{i_x, i_y})}{h_x}, \\ \Lambda_y Q_{i_x, i_y} &= k_{\frac{1}{2}, i_y} \frac{T(Q_{i_x, i_y+1}) - T(Q_{i_x, i_y})}{h_y} + k_{-\frac{1}{2}, i_y} \frac{T(Q_{i_x, i_y-1}) - T(Q_{i_x, i_y})}{h_y}. \end{aligned} \quad (9)$$

The schematic template is shown in Fig. 1.

When modeling thermal processes in an ice island, it is necessary to take into account that ice melting in the upper part of the island can flow downward, thus changing the substance at the mesh point. For this, at each time step, all nodes of the computational mesh are checked for the fulfillment of the melting condition. If it is satisfied, the substance is replaced in the node. In addition, the model takes into account the flow in the liquid, as a result of which mixing occurs. The realization of all these effects implies the modification of the values of heat content and matter at the grid nodes after solving equations (8) when certain conditions are reached.

2.3. SOFTWARE IMPLEMENTATION

The developed program accepts as input a rectangular two-dimensional uniform mesh, as well as configuration files and initial temperature distribution. In the configuration file, it is possible to specify all the characteristics of substances, the parameters of the task, such as the time step and the total number of steps, as well as the frequency of recording the fields of temperatures, heat content and aggregate state into the VTK file for subsequent visualization.

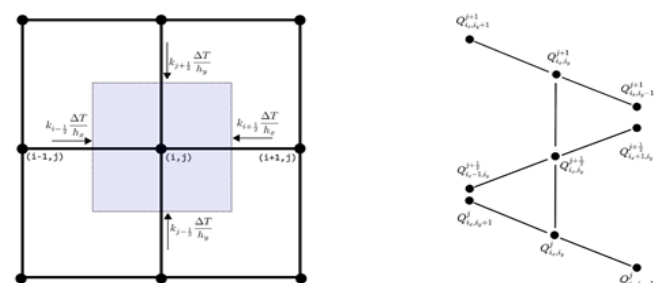


Fig. 1. Template (right) and illustration of the method working on a two-dimensional mesh (left).

The program solves the problem in several stages. At the beginning, the correctness of the input data is checked and a uniform mesh is built according to the transmitted data. After this, the initial field of heat content is computed using equation (6). Then equations (9) are solved by the sweep method. Moreover, method (11) allows for parallel execution. To do this, each step is divided into $i_x = 1, 2, \dots, N_x$ for the first half step and $i_y = 1, 2, \dots, N_y$ for the second separate iterations, which can be solved in parallel. OpenMP is used for parallelization.

The solution of the systems is found using the sweep method (Thomas's algorithm). For systems of this kind, a solution can be obtained in $O(n)$ operations. This algorithm will parallelize quite well using block decomposition:

- The original matrix is represented as a product of a block matrix and some modified matrix. In this case, the block matrix can be scattered between processes in blocks.
- Computation of blocks independently by different processes.
- Return to the original matrix.

After each time step, the grid nodes are checked for the fulfillment of the phase transition conditions. With a user-defined frequency, the values of the grid function of heat content are converted into temperature (7) and written to the VTK file.

Subsequent rendering of VTK files is possible using the open source ParaView software, as well as custom developed scripts.

To set the initial conditions, scripts have been implemented for constructing meshes from arbitrary substances of various shapes (circle, rectangle, etc.), as well as initial temperatures from VTK files of previous computations and arbitrary figures with constant temperatures.

3. RESULTS

3.1. PROBLEM FORMULATION

The integration area is an ice island with a height of 10 m and a horizontal length of 300

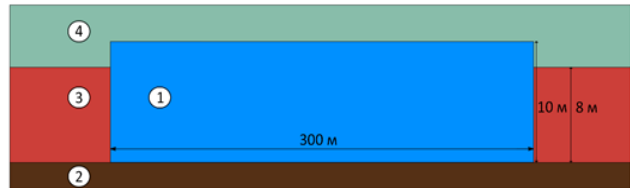


Fig. 2. Model of ice island.

m [3]. The island is submerged in water at a depth of 8 m and lies on the bottom. The geometrical dimensions of the area and the layout are shown in Fig. 2. The characteristics of the substances are presented in Table 1. We also assume that the melting point of ice is $T_0 = 0^\circ\text{C}$, and its specific heat of fusion $\lambda = 334 \text{ kJ/kg}$.

In Fig. 2, the designations of substances are introduced: 1 – ice (artificial ice island), 2 – bottom soil, 3 – water, into which the ice island is immersed, 4 – air.

The distribution of temperatures in the ice island was found at average temperatures in winter. Computations were also carried out to study the stability of the ice island to melting during seasonal temperature changes.

The computations were carried out using three main models:

- setting without taking into account the flow of water and freezing of the soil;
- setting taking into account water flow, but without soil freezing;
- setting taking into account water flow and soil freezing.

3.2. THE RESULTS OF MODELING THE PROBLEM IN THE FORMULATION WITHOUT TAKING INTO ACCOUNT WATER FLOW AND SOIL FREEZING

Modeling were carried out to determine the equilibrium temperature distribution in the ice island at an air temperature of -40°C ,

Table 1. Thermophysical properties of substances.

No	Substance	Density, kg/m ³	Thermal conductivity, W/(m·K)	Specific heat, J/(kg·K)
1	Ice	917	0.591	2100
2	Bottom soil	2500	0.8	750
3	Water	1000	2.22	4180
4	Air	1.60	0.022	-

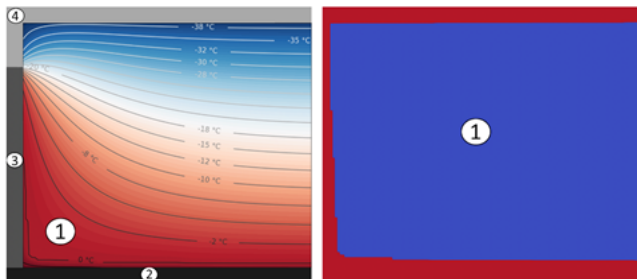


Fig. 3. Temperature distribution in an ice island (left) and a map of phase states (right) in the problem of establishing the temperature in an ice island in the setting without taking into account soil freezing.

a bottom soil temperature of 5°C and a water temperature of 3°C . The problem of establishing was solved, the initial temperature of the ice island was 10°C , the contacting substances (water, air, soil) were set in the form of boundary conditions with given temperatures, heat capacities, and thermal conductivity coefficients.

Fig. 3 shows the results of computing the temperature settling. A period of 150 days was simulated. On the left is a picture of the distribution of temperatures in the ice island, on the right is a map of phase states (blue – ice, red – water and air).

Further, the study of the stability of the ice island was carried out with seasonal temperature changes. The air temperature has been changed to 3°C . The results after 150 days are shown in **Fig. 4**. It can be seen that from the edges the ice island practically did not melt – since we do not take into account the flow of water, a

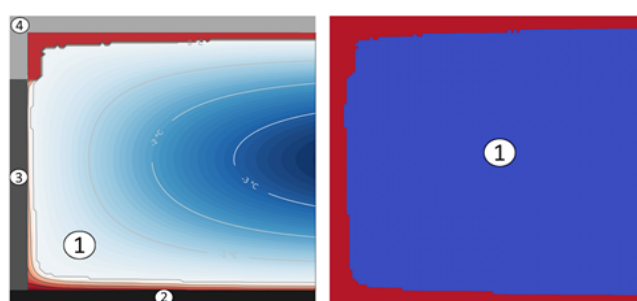


Fig. 4. Temperature distribution in an ice island (left) and a map of phase states (right) in the problem of melting an ice island under the influence of a change in air temperature in the formulation without taking into account the water flow and soil freezing.

temperature gradient simply established there. From above, the island melted significantly, since after melting the water immediately flowed down and the boundary condition with air was set on the remaining ice mass. Even a relatively low coefficient of thermal conductivity of the air provided a serious heat flow, which melted the island.

3.3. THE RESULTS OF MODELING THE PROBLEM IN THE FORMULATION TAKING INTO ACCOUNT THE WATER FLOW AND WITHOUT SOIL FREEZING

Obviously, without taking into account the flow of water, the ice island will practically not melt. Let's take into account the water flow as follows. For any melted water with a temperature strictly greater than zero, at the end of the time step, we explicitly set the temperature equal to three degrees Celsius. As a result, it will be possible to take into account the flow of water. We use the distribution of substances, the temperature distribution after freezing, and the thermophysical constants obtained in the problem of establishing the temperature distribution in Section 3.2. Similar to the previous calculation, the results after 150 days of melting of the ice island are shown in **Fig. 5**. It is clearly seen that the island has practically melted. This was due to the fact that a thin layer of water appeared in its bottom part during the establishment. Further, the constant water temperature created a large temperature difference with the ice and, as a consequence, an abnormally large heat flux through the lower edge.

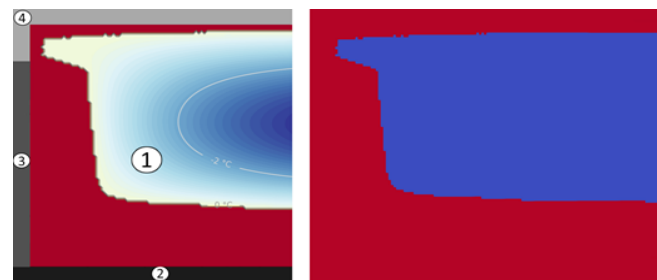


Fig. 5. Temperature distribution in an ice island (left) and a map of phase states (right) in the problem of melting an ice island under the influence of air temperature changes in the formulation taking into account the water flow.

3.4. THE RESULTS OF MODELING THE PROBLEM IN THE FORMULATION TAKING INTO ACCOUNT THE FLOW OF WATER AND SOIL FREEZING

In order to solve the problem that arose when taking into account the flow of water in paragraph 3.3, you can take into account the freezing of the soil. To do this, we use a computational area of 300 meters by 20 meters, where ice occupies the upper half, similar to the previous statements, and 10 meters below it is filled with soil (in previous calculations, the boundary of the island with the soil was set by the boundary condition). The initial temperature distribution is similar to paragraph 3.2, the soil has an initial temperature of +5°C. The boundary conditions for water and air are similar to the previous formulations with the addition of the condition of zero heat flux through the bottom and side faces of the soil massif.

The results of modeling the establishment of temperatures are shown in **Fig. 6**. It can be seen that the depth of soil freezing is about five meters. On the right in Fig. 6 there is a map of phase states in the computational domain. Dark blue denotes a solid medium (ice and soil), blue – liquid (water) and red – gaseous (air).

Further, for this temperature distribution, the problem of stability in extreme conditions with water flow was set. The air temperature was taken equal to +10°C. The simulation results are shown in **Fig. 7**. It can be seen that after 150 days the topside melted

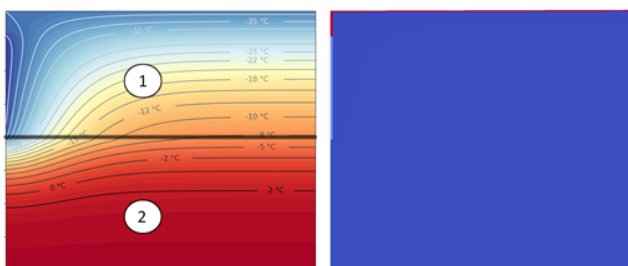


Fig. 6. Temperature distribution in an ice island (left) and a map of phase states (right) in the problem of establishing the temperature in an ice island in the setting taking into account soil freezing.

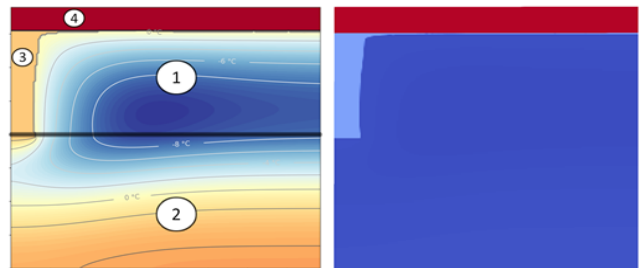


Fig. 7. Temperature distribution in an ice island (left) and a map of phase states (right) in the problem of melting an ice island under the influence of a change in air temperature in the setting taking into account the water flow and freezing the soil.

completely. The edge of the island has also seriously melted, the size of the thawed part is comparable to the size of the surface of the island. The temperature in the interior of the island and in the soil has practically not changed.

4. CONCLUSION

The enthalpy approach for solving the Stefan problem and the software for solving this problem in various settings were developed. On the basis of this program, various models of the ice island were tested and conclusions about its resistance to melting were drawn. The developed approach allows one to take into account various external influences, such as heat fluxes from man-made installations, water flow and seasonal temperature changes. Based on the data obtained, it is possible to more efficiently plan the development of the structure of future ice islands, and also an opportunity opens up for numerical modeling of existing ones in order to audit their integrity. Also, using this approach, it is possible to check the feasibility of using such materials as pykerite and other ice-composite materials, the introduction of additional heat-insulating layers, cooling the fins of the island and other ideas.

The developed methods can be applied in solving static and dynamic thermoelastic problems, which are a logical continuation of this study.

REFERENCES

1. Crawford A, Crocker G, Mueller D, et al. The canadian ice island drift, deterioration and detection (CI_2D_3) database. *Journal of Glaciology*, 2018, 64(245):517-521.
2. Gorgutsa EYu, Kurilo EYu. Stroitelstvo iskusstvennykh ledovykh ostrovov v usloviyakh Arktiki [Artificial ice islands construction in Arctic conditions]. *Gidrotekhnika. XXI vek*, 2017, 4(32):54-57.
3. Petrov IB, Muratov MV, Sergeev FI. The research of artificial ice islands stability by methods of mathematical modeling. *Doklady RAN. Mathematics*, 2020, 495: 33-36.
4. Buzin VA, Zinivev AT. Ledovye protsesy i yavleniya na rekakh I vodokhranilischakh. Metody matematicheskogo modelirovaniya i opyt ikh realizatsii dlya prakticheskikh tselei (obzor sovremenogo sostoyaniya problemy [Ice processes and phenomena on rivers and water reservoirs. Methods of mathematical modeling and experience of their realization for practical aims (the review of modern problem state)]. 2009, http://www.iwep.ru/ru/bibl/books/monograf/Zinovev_Buzin.pdf.
5. Comfort G, Abdelnour R. Ice Thickness Prediction: A Comparison of Various Practical Approaches. CGU HS Committee on River Ice Processes and the Environment, *17th Workshop on River Ice*, Edmonton, Alberta, 2013.
6. Anneck NN. Method for Prediction of Sea Ice Thickness Based on the Blowing Air Temperature and Speed. *Master Thesis* at University of Liege, 2015.
7. Albu AF. Primenenie metodologii bystrogo avtomaticheskogo differentsirovaniya k resheniyu zadach upravleniya teplovymi protsessami s fazovymi perekhodami [The application of quick automatic differentiation methodology for thermal processes with phase transitions management problems]. *PhD dissertation*, Moscow, 2016.
8. Biryukov VA, Miryakha VA, Petrov IB. Chislennoe modelirovanie trekhmernoi zadachi tayaniya iskusstvennogo ledyanogo ostrova entalpiinym metodom [Numerical modeling of artificial ice island melting 3D-problem by enthalpy method]. *Chetvertaya vserossiiskaya konferentsiya s mezhdunarodnym uchatiem ‘Polyarnaya Mekhanika-2017’*, 2017, 81-86.
9. Jonsson T. On the one-dimensional Stefan problem with some numerical analysis Bachelor of Mathematics. *180hp Department of Mathematics and Mathematical Statistics*, 2013.
10. White RE. An enthalpy formulation of the Stephan problem. *SIAM J. Numer. Anal.*, 1982, 19(6):1129-1157.
11. White RE. A numerical solution of the enthalpy formulation of the Stephan problem. *SIAM J. Numer. Anal.*, 1982. 19(6):1158-1172.
12. Samarskii AA. *Vvedenie v chislennye metody* [Introduction in numerical methods]. Moscow, Nauka Publ., 1987.
13. Vasil'ev FP. The method of straight lines for the solution of a one-phase problem of the Stefan type. *USSR Computational Mathematics and Mathematical Physics*, 1968, 8(1):81-101.
14. Bachelis RD, Mamelad VG, Schyaffer DB. Solution of Stefan's problem by the method of straight lines. *USSR Computational Mathematics and Mathematical Physics*, 1969. 9(3):113-126.
15. Budak BM, Solov'eva EN, Uspenskii AB. A difference method with coefficient smoothing for the solution of Stefan problems. *USSR Computational Mathematics and Mathematical Physics*, 1965, 5(5):59-76.
16. Dar'in NA, Mazhukin VI. Matematicheskoe modelirovanie zadachi Stefan ana adaptivnoi setki [Mathematical modeling of Stefan problem on adaptive mesh]. *Differentsial'nye uravneniya*, 1987, 23(7):1154-1160.
17. Buchko NA. Entalpiiniyi metod chislenного resheniya zadach teploprovodnosti v promezayuschikh ili protaivayuschikh

- gruntakh [Enthalpy method for the numerical solution of heat conduction problems in freezing or thawing soils]. *SPbGUNTiPT*. http://refportal.com/upload/files/enthalpiiny_metod_chislennoego_resheniya.pdf.
18. Albu AF, Zubov VI. Mathematical modeling and study of the process of solidification in metal casting. *Computational Mathematics and Mathematical Physics*, 2007, 47:843–862.
19. Albu AF, Zubov VI. Choosing a cost functional and a difference scheme in the optimal control of metal solidification. *Computational Mathematics and Mathematical Physics*, 2011, 51:21-34.

DOI: 10.17725/rensit.2021.13.087

Software architecture for display controller and operating system interaction

Konstantin V. Pugin, Kirill A. Mamrosenko, Alexander M. Giatsintov

Center of Visualization and Satellite Information Technologies, Federal Scientific Center Scientific Research Institute of System Analysis of the RAS, <https://niisi.ru/>

36/1, Nachimovsky av., Moscow 117218, Russian Federation

E-mail: rilian@niisi.ras.ru, mamrosenko_k@niisi.ras.ru, algts@niisi.ras.ru

Received January 15, 2021, peer-reviewed January 22, 2021, accepted January 29, 2021

Abstract: Article describes solutions for developing programs that provide interaction between Linux operating system and multiple display controller hardware blocks (outputs), that use one clock generation IP-block with phase-locked loop (PLL). There is no API for such devices in Linux, thus new software model was developed. This model is based on official Linux GPU developer driver model, but was modified to cover case described earlier. Article describes three models for display controller driver development – monolithic, component and semi-monolithic. These models cannot cover case described earlier, because they assume that one clock generator should be attached to one output. A new new model was developed, that is based on component model, but has additional mechanics to prevent race condition that can happen while using one clock generator with multiple outputs. Article also presents modified model for bootloaders graphics drivers. This model has been simplified over developed Linux model, but also has component nature (with less components) and race prevention mechanics (but with weaker conditions). Hardware interaction driver components that are developed using provided software models are interchangeable between Linux and bootloader.

Keywords: drivers, embedded, KMS, kernel module, development

UDC 004.454

Acknowledgments: Publication is made as part of national assignment for SRISA RAS (fundamental scientific research 47 GP) on the topic No.0580-2021-0001 (AAAA-A19-119011790077-1).

For citation: Konstantin V. Pugin, Kirill A. Mamrosenko, Alexander M. Giatsintov. Software architecture for display controller and operating system interaction. *RENSIT*, 2021, 13(1):87-94.
DOI: [10.17725/rensit.2021.13.087](https://doi.org/10.17725/rensit.2021.13.087).

CONTENTS

1. INTRODUCTION (87)
2. MATERIALS AND METHODS. GRAPHICS DRIVER DEVELOPMENT MODELS USING THE LINUX DRM SUBSYSTEM (89)
3. RESULTS. DEVELOPMENT OF A NEW DRIVER MODEL FOR A DEVICE WITH SEVERAL OUTPUT DEVICES AND ONE FREQUENCY SYNTHESIZER (90)

4. DISCUSSION (92)

5. CONCLUSION (93)

REFERENCES (93)

1. INTRODUCTION

In some cases, development of embedded systems requires compromise decisions to be made to secure compliance of the product with the applicable requirements. Such a situation can

be seen, for example, when restrictions apply to heat release or crystal size, or when transistor budget needs to be reduced.

Sometimes, such compromise solution is to reduce the number of frequency synthesizers (FS). Multiple display controllers use the same FS, but different display interface protocols (e.g. TMDS and LVDS) are used while the outputs operate concurrently.

In addition, such embedded systems can use a common configurable register. In such register, both general parameters of the whole display subsystem and some parameters of individual controllers are often configured. This complicates programming of the output subsystem, since such register becomes a shared resource and requires access control.

Such display system configuration requires new approaches to be developed to create drivers that ensure that the system is functional. Accordingly, our tasks are as follows:

1. Consider possible models for creation of drivers for such embedded systems;
2. Compare the models under consideration in terms of extensibility and functionality of the resulting drivers;
3. Develop a driver model that will allow solving the problem of interaction with the operating system when multiple display controllers and one frequency synthesizer are used.

The research will be conducted on the basis of Linux OS, which is a common operating system for embedded systems.

There are several kernel subsystems used in development of a display controller driver for Linux. The applied model depends on the subsystem used (which can be specified in documentation or identified from an analysis of sample drivers). Let us look at the most popular ones:

1. DRM. As stated in [1], the display controller and mode setting interface is

part of the Direct Rendering Manager (DRM) infrastructure. DRM developers [2] consider this subsystem in terms of 2 models — an external and an internal ones. According to their views, the external model includes 5 entities, such as framebuffer, plane, CRTC, encoder and connector, which are listed from proximity to the user space to proximity to the display. The internal subsystem model additionally includes a bridge between the encoder and the connector, while the connector can also include a panel. In contrast, software developers [3] and independent researchers [4] generally consider an external model or a simplified external model only.

2. FrameBuffer device (fbdev). If fbdev [4] is used, the model consists of 2 components: a memory buffer interacting with the user space and a monolithic virtual DC (display controller) device that controls several physical devices. The modes of the device were set directly from the user space thus causing problems [5]. Along with the identified problems, such simplified model has low extensibility and lower functionality than models based on the DRM subsystem [6]. Currently, the latest available drivers based on this model are being redeveloped into drivers based on DRM model variations [7]
3. Driver solutions for Android Display Framework (ADF) exist, but have the following disadvantage: standard hardware-independent protocol functions need to be developed from scratch in each driver increasing the possibility of errors and the complexity of the task. In addition, as the ADF subsystem is a development of fbdev, drivers need to be combined, as despite the atomicity, models based on this subsystem remain monolithic, which was the reason for replacement of the subsystem with DRM [8].

2. MATERIALS AND METHODS.

GRAPHICS DRIVER DEVELOPMENT MODELS USING THE LINUX DRM SUBSYSTEM

Controller driver solutions in a number of other Unix-compatible systems (e.g. FreeBSD) also use the DRM subsystem as the most extensible and functional open subsystem for development of such drivers [9].

To develop a driver using the DRM, an approach should be used so that the driver model is not in conflict with the external and internal subsystem models, thus allowing the use of the DRM API for programming display controllers, especially when an image is displayed by multiple display units simultaneously. Three models were analyzed during the development of the driver.

A completely monolithic type (**Fig. 1**) is characterized by relative simplicity of the device, but at the same time it has a very high cohesion. This implies that various DTLC (display transmitter link controller – a controller that encodes and decodes signals for a display unit and works with a graphics transmission protocol) subsystems and various FS types require writing of completely different drivers, despite an identical IP-block of the display controller. Despite that such driver formally belongs to the

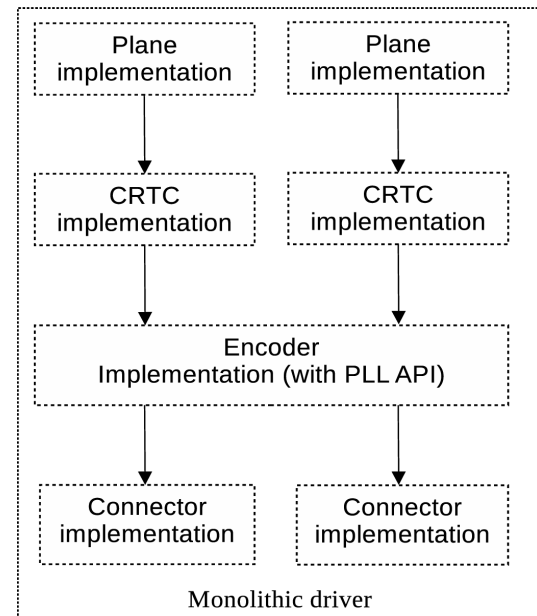


Fig. 1. Monolithic driver model.

DRM subsystem, the model has the advantages and disadvantages of the previous generation subsystems. This significantly limits the ability of the drivers based on such model to update and replace components – a new driver will have to be developed for each revision of the system. An advantage to be noted is the simplicity of the driver for each device.

The second type is a cohesive component model considering possible replacement of hardware (**Fig. 2**). Drivers based on this model have a slightly lower component

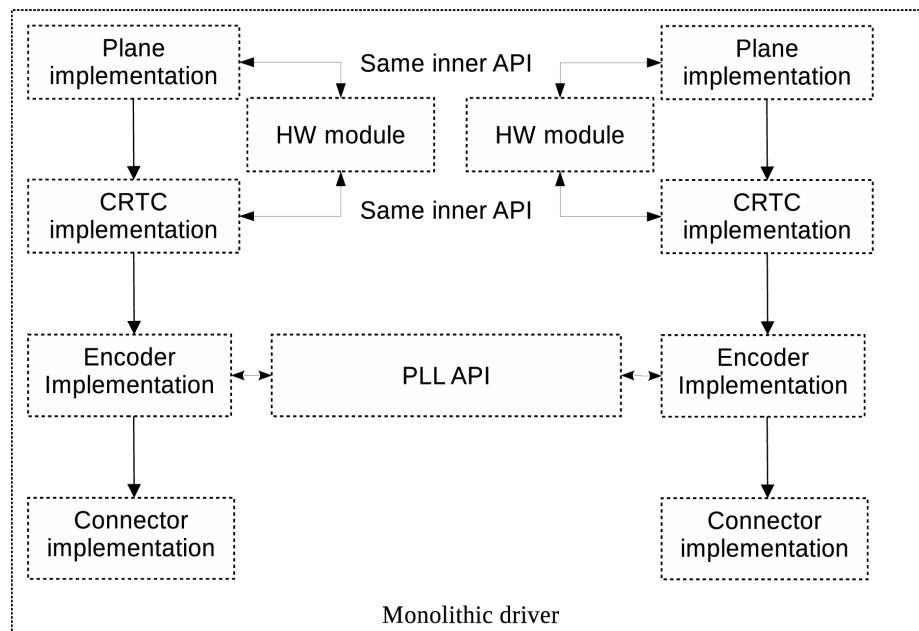


Fig. 2. Semi-monolithic driver model.

cohesion, which simplifies modification for a new controller type, but does not solve the problem of extensibility and adds complexity to the driver due to separation of components. Despite internal division into components and lower cohesion, drivers based on this model still have an important disadvantage of completely monolithic drivers, such as the need to modify the whole driver for each combination of components in all possible revisions, which complicates driver unification.

The third type is built on the basis of the external DRM model and following the example of other drivers for embedded systems that use the DRM subsystem [10] – a model that is developed on the principle of maximum independence and interchangeability of components (**Fig. 3**). Drivers based on this model are extensible and all their components are interchangeable. For example, it is possible to replace only a DTLC driver, or only a frequency synthesizer driver, or only a configuration device driver. It is also possible to use drivers that have been already developed (with minor modifications for integration), which is important when IP-blocks are purchased from other manufacturers. In addition, as the model

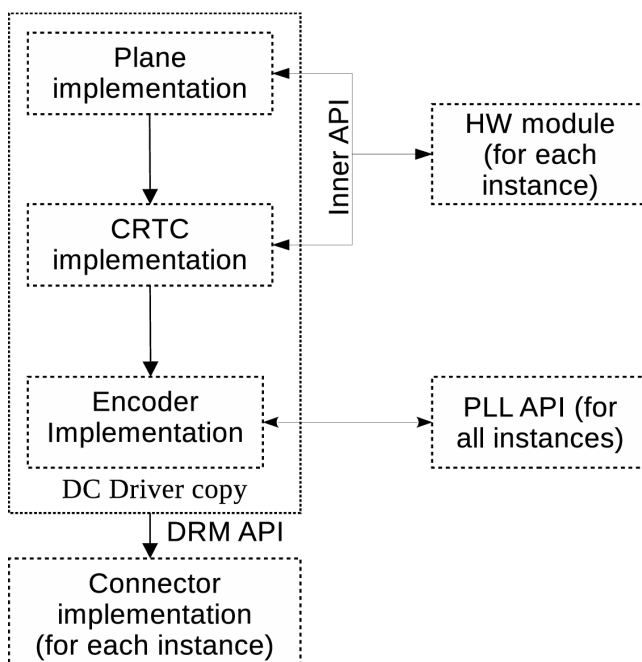


Fig. 3. Component driver model.

is not monolithic, it is possible to build an API that will address common devices avoiding the race condition and, at the same time, will not integrate the driver of the device into a monolithic structure.

When only the external model is considered and all the components have maximum independence, a more complex algorithm than the one implied by abstraction of the external model is required to control some DTLC controllers. For example, interaction with the DTLC component has to be taken into account when the controller is switched on and off.

Since many modern display interface protocols (e.g. DisplayPort) require the use of the above algorithm, the presented model needs to be modified considering their features.

3. RESULTS. DEVELOPMENT OF A NEW DRIVER MODEL FOR A DEVICE WITH SEVERAL OUTPUT DEVICES AND ONE FREQUENCY SYNTHESIZER

Among the solutions described above, the component solution was tested (Fig. 3) as the most extensible one, which uses the internal mechanisms of the Linux kernel to a greater extent. During testing of the driver based on solution 3, this solution revealed the following disadvantages:

1. Race condition when the clock generator is addressed. Since all instances work with the clock frequency control API, when the FS is addressed in parallel the frequency will vary in a chaotic manner, which will lead to a flickering screen and incorrect operation of an output.
2. When only the external DRM model is used, it is impossible to create such DTLC driver that requires complex interaction with the FS or display controller driver. In the external DRM model, the replaceable component is the connector, which does not have

- dynamic APIs for interacting with DTLC [2]. Therefore, an internal DRM model has to be used, which is incompatible with the model shown in Fig. 3.
3. Driver instances within the kernel based on the component model are completely independent, which makes it difficult to transfer data between them. Since the instances are identical, a race condition can occur when data are written in the configuration register.

To solve the above problems, modifications were made in the component model, which eventually became as follows (**Fig. 4**):

1. The first instance of the DC driver becomes the only instance that is able to transmit information to the FS driver. All instances are able to receive information.
2. The first instance of the driver determines configuration parameters that are common for all instances and sets the same in the common configuration register.
3. To link the display controller driver and the DTLC driver, the bridge component of the internal DRM model is used, which operates jointly with the connector component of the external model.

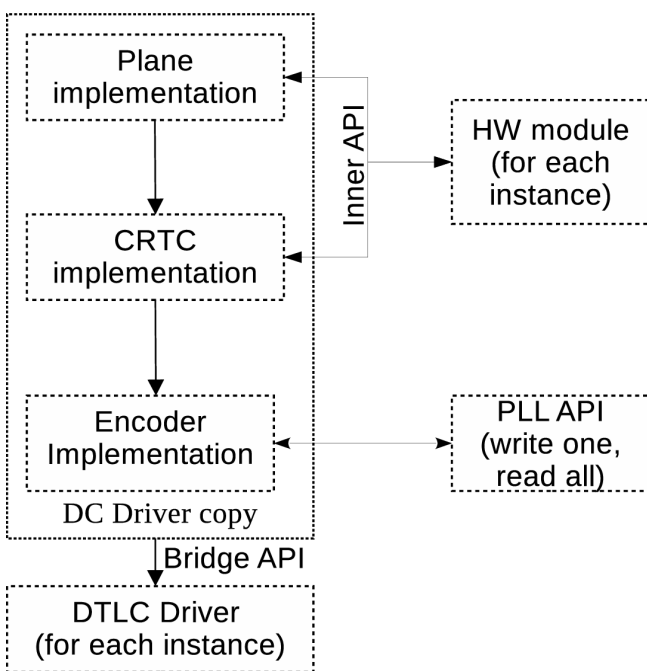


Fig. 4. Newly developed component-based model.

4. Parameters of permissible modes are calculated as:

$$a_1 \cdot x_1 - a_2 \cdot x_2 \leq b,$$

where a_i is the coefficients associated with DTLC (the exact value depends on the DTLC hardware), b is the error coefficient (which depends on the interface protocols; in particular, for DVI the coefficient is 0.025[11]), and x_i is the pixel frequency coefficients of the requested modes. In this case, a_i and b coefficients are parameters that are set when a driver based on the model shown in Fig. 4 is developed, while x_i is the variables calculated when the driver is running.

Most systems working under Linux use low-level bootloaders (U-Boot [12], BareBox [13]) for initial initialization and loading of devices, including display subsystem devices (**Fig. 5**). In such cases, apart from a driver for the OS, a bootloader driver that is capable of performing the basic display functions also has to be developed. With some modifications in the model due to simplified nature of the graphic API of the bootloader (if any) and incomplete suitability of the graphic API for the DRM subsystem, parts of the driver for Linux based on the developed model can be used. To be able to use low-level bootloaders (in particular, those listed above) in the drivers, the following modifications were made in the model:

1. There is no separate DTLC module in the bootloader, as no work with complex

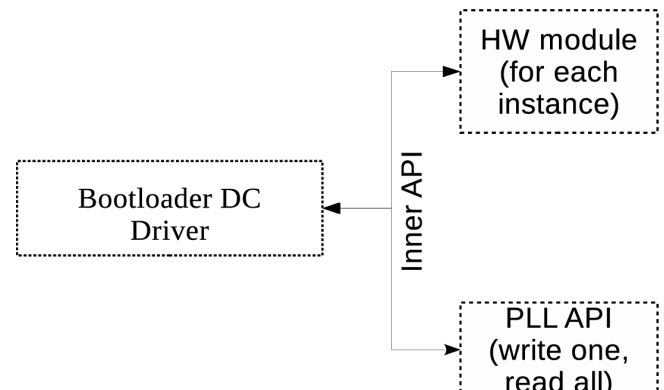


Fig. 5. Bootloader driver model

- protocols is carried out. Therefore, everything is included in the display controller driver.
2. The DC driver model in the bootloader does not have such entities as plane, encoder and crtc. All display operations are carried out in the same structure, so the DC driver is monolithic. Despite being similar to the model based on fbdev, the bootloader subsystem has fewer features. This is due to the bootloader's focus on quick booting of the operating system and reduction of the bootloader size.
 3. The bootloader does not require simultaneous use of several screens, so one instance of the display driver is sufficient in case of identical output devices.

Simultaneous use of the FS by multiple display devices is very rarely met in the graphic subsystem of the bootloader, so the only remaining option is simultaneous use of the same memory area by multiple devices. Consequently, drivers are significantly simplified.

An interesting point is also the relationship between the bootloader driver components and the OS driver. If the OS driver is based on the model described in the previous chapter, its module for interaction with the hardware will be applicable in the bootloader if the internal API is the same. This significantly simplifies writing of complex device drivers, where interaction with hardware requires algorithms for calculation of parameters (independent of the high level) or sequences of data records in the device registers.

Despite a simpler structure, bootloader drivers inherit the component principle. This allows an incremental update of driver components both in case of a change in the hardware and when the bootloader is modified making the update easier [14].

4. DISCUSSION

The developed model has the following advantages over the considered model options:

1. Extensibility – the DC driver based on this model can be extended with any DTLC driver (including those developed before creation of a driver based on the above model) that uses bridge API.
2. Accelerated transition to new controller models. As transition to a new controller model requires only development of a new module for interaction with hardware, no complete redevelopment of the driver is required in comparison with the model shown in Fig. 1, and no complete update of the driver (it is enough to update the module for interaction with hardware only) is required in comparison with model 2.
3. Unlike drivers based on the component model, as shown in Fig. 3, drivers based on the developed model do not go into the race condition if the application software constantly requests the DRM API to change the frequency.
4. Furthermore, unlike the model shown in Fig. 3, drivers based on the modified model are able to display multiple images on all display units at the same time (when the permissible modes are set). The driver based on model 3 will give an unstable image in case of constant recording in the FS (as different display units require different pixel frequencies, the image will flicker), and drivers based on models 1 and 2 will set the frequency of the display unit, which was connected last).

In comparison with the considered models, the developed model has the following disadvantages:

1. Increased complexity of driver development in comparison to model 1.
2. More failure possibilities due to a larger number of points of failure (more driver instances and possibilities of random recombination with DTLC drivers).
3. The use of Bridge API is complicated in architectures with no device tree; complex

data manipulations to find the bridge are needed.

5. CONCLUSION

In the course of the research, various possible variants of the driver architecture for a device with multiple display controllers and one frequency synthesizer were analyzed. From several known driver models, a new derived driver model for such a device was developed, which combines the advantages of all the proposed models, but has a disadvantage – creation of a driver based on this model is difficult if no device-tree is used. This disadvantage is not significant for embedded systems with Linux, as most of them use a device tree.

The created model was tested during the development of the driver for a device with DVI outputs, LVDS on a single FS, under Linux, with MIPS architecture. All model implementations were successfully tested using the Protium prototyping system [15].

The results of the research can be used to create new drivers for this class of devices for Unix-like systems if hardware with multiple outputs and one frequency synthesizer is used.

REFERENCES

1. Konstantin V. Pugin, Kirill A. Mamrosenko, Alexander M. Giatsintov. Visualization of graphic information in general-purpose operating systems. *Radioelektronika, Nanosistemy, Informacionnye Tekhnologii. (RENSIT)*, 2019, 11(2):217-224. DOI: 10.17725/rensit.2019.11.217.
2. Linux GPU Driver Developer's Guide [Electronic resource]. 2019. URL: <https://dri.freedesktop.org/docs/drm/gpu/index.html> (accessed: 06.03.2019).
3. Rob Clark. GStreamer and dmabuf. *GStreamer Conference*. San Diego, USA: Linux Foundation, 2012.
4. Laurent Pinchart. DRM/KMS, FB and V4L2: How to Select a Graphics and Video API. *Embedded Linux Conference Europe*. Barcelona, Spain: Linux Foundation, 2012.
5. Luc Verhaegen. X and Modesetting: Atrophy illustrated. *FOSDEM*, 2006, Brussels, Belgium, 2006.
6. Laurent Pinchart. Why and How to use KMS as Your Userspace Display API of Choice. *LinuxCon*. Tokyo, Japan, 2013, p. 52.
7. Michael Larabel. SUSE Develops New Driver That Exposes DRM Atop FBDEV Frame-Buffer Drivers [Electronic resource]. 2019. URL: https://www.phoronix.com/scan.php?page=news_item&px=FBDEVDRM-DRM-Over-FBDEV (accessed: 22.06.2019).
8. Alistair Strachan. DRM/KMS for Android. *Linux Plumbers*. Vancouver, BC: Linux Foundation, 2018.
9. Jean-Sébastien Pétron. Status of the Graphics Stack on FreeBSD. *X.Org Developer's Conference*. Bordeaux, France, 2014.
10. Marek Szyprowski. Linux DRM: New picture processing API. *LinuxCon*, Berlin, Germany: Linux Foundation, 2016.
11. Digital Display Working Group. Digital Visual Interface DVI Revision 1.0 [Electronic resource]. 1999. URL: https://web.archive.org/web/20120813201146/http://www.ddwg.org/lib/dvi_10.pdf (accessed: 30.12.2020).
12. Anatolij Gustschin. U-Boot video API [Electronic resource]. 2020. URL: [git https://gitlab.denx.de/u-boot/custodians/u-boot-video.git](https://gitlab.denx.de/u-boot/custodians/u-boot-video.git) (accessed: 29.07.2020).
13. Hauer S. BareBox [Electronic resource]. 2020. URL: <https://github.com/saschahauer/barebox> (accessed: 29.07.2020).
14. Y. Kang, J. Chen, B. Li. Generic Bootloader Architecture Based on Automatic Update Mechanism. *IEEE 3rd International Conference*

- on Signal and Image Processing (ICSIP).* Shenzhen,
China, 2018, p. 586-590.
15. Andrey Y. Bogdanov. Experience in the
Use of Protium FPGA-Based Prototyping
Platform to Verify Microprocessors. *SRISA
RAS Papers*, 2017, 7(2):46-49.

DOI: 10.17725/rensit.2021.13.095

The problem of increasing the capacity of mobile communication channels and possible solutions

Andrey S. Tyutyunik, Vladimir S. Gurchenko

V.I. Vernadsky Crimean Federal University, <https://cfuv.ru/>

Simferopol 295007, Russian Federation

E-mail: real-warez@mail.ru, gurchenko_v@mail.ru

Alexey A. Badashev

KTK TELECOM, <https://volnamobile.ru/>

E-mail: badasher@mail.ru

Received November 30, 2020, peer-reviewed December 12, 2020, accepted December 27, 2020

Abstract: In this paper the problem of the growing demand for increasing the capacity of communication channels is considered, using the example of real statistical data of the current mobile operator, and the search for possible ways to solve this issue. The analysis of the distribution of electromagnetic fields and SAR for a three-layer model of the human head when interacting with a cell phone is carried out. The results obtained allow us to conclude that it is impossible to significantly increase the capacity of mobile terminals. The increase in power is accompanied by a significant increase in the spatial peak SAR, which exceeds the value recommended by international standards. As an alternative, the main directions and developments for raising the energy potential in the fifth generation 5G cellular radio channels in the millimeter wavelength range have been identified.

Keywords: specific absorption rate, channel capacity, mobile phone antenna, electromagnetic effect

PACS 07.57. –, 84.40.Ba

Acknowledgments: The reported study was funded by RFBR, project number 19-32-90038. The authors are grateful to the organization "KTK TELECOM", the official mobile operator in Crimea, for providing real statistical data presented in the article.

For citation: Andrey S. Tyutyunik., Alexey A. Badashev, Vladimmir S. Gurchenko. The problem of increasing the capacity of mobile communication channels and possible solutions. *RENSIT*, 2021, 13(1):95-103. DOI: 10.17725/rensit.2021.13.095.

CONTENTS

1. INTRODUCTION (95)
2. PROBLEMS OF INCREASING MOBILE TRAFFIC VOLUME ()
3. EFFECT OF ELECTROMAGNETIC RADIATION ON HUMAN BIOLOGICAL SYSTEM ()
4. MODERN SOLUTIONS IN MOBILE COMMUNICATIONS SYSTEMS, 5G TECHNOLOGY ()
5. CONCLUSION ()
- REFERENCES ()

1. INTRODUCTION

Communication technologies are one of the most actively developing areas in the field of science and technology. With the advent of new developments, such as cloud storage, smart home, smart city, automated systems for medical, financial, technical services, etc., the problem in the growth of data transmission speed is becoming more and more urgent [1-3]. Humanity has come close to the era of the Internet of

Things (IoT devices), when the automation of processes no longer requires human participation, which in turn leads to an unprecedented variety of requirements and scenarios for developed applications [4,5]. Along with this, the amount of data that is generated by a huge number of IoT devices continues to grow exponentially [6]. The number of devices connected to the IoT - smartphones, personal computers, urban and industrial sensors, etc., has already exceeded the population and reached 9 billion [7]. Thus, the upward trend in traffic and data transmission is a big problem for the functional operation of the network [8,9], and the gap between the rapidly growing requirements for data transmission speed and existing network infrastructures with limited bandwidth has become more and more noticeable [10]. Unfortunately, the modern 4G communication system can no longer provide effective support for the above technologies in terms of transmission speed, connection density, end-to-end latency, etc. [11]. A more efficient and reliable mobile communication system is needed to meet all the growing needs.

On the other hand, an increase in the number of transceiver devices leads to an increase in the effect of radio waves on the human body [12]. The Institute

of Electrical and Electronic Engineering (IEEE) and the International Commission on Non-Ionizing Radiation Protection (ICNIRP) have established requirements for a peak absorption power standard to limit exposure to electromagnetic radiation [13,14]. When exposed to electromagnetic radiation, biological tissues absorb it, as a result of which the absorbed energy is converted into heat, which leads to an increase in tissue temperature, which negatively affects the biological functions of the body [15].

Based on the foregoing, the purpose of this work is to study the problem of increasing the demand for the bandwidth of communication channels using the example of real statistical data and to find possible ways to solve this problem. In particular, the analysis of the impact of microwave electromagnetic radiation on the human biological system.

2. PROBLEMS OF INCREASING MOBILE TRAFFIC VOLUME

With the development of the economy and the growth of material and cultural needs of people, the subscriber base of mobile operators is increasing, which subsequently leads to an increase in the number of terminals (**Fig. 1a**). The volume of mobile data transmission (voice and

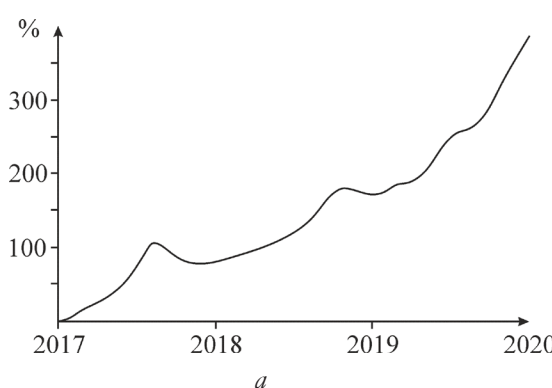
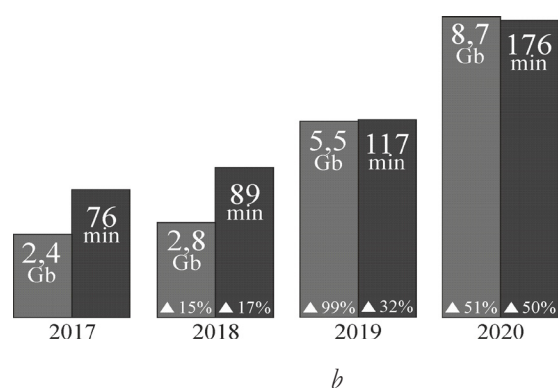


Fig. 1. (a) - Growth of the subscriber base for the period from 2017 to 2020; (b) - an increase in voice and Internet traffic consumed on average by one subscriber per day.



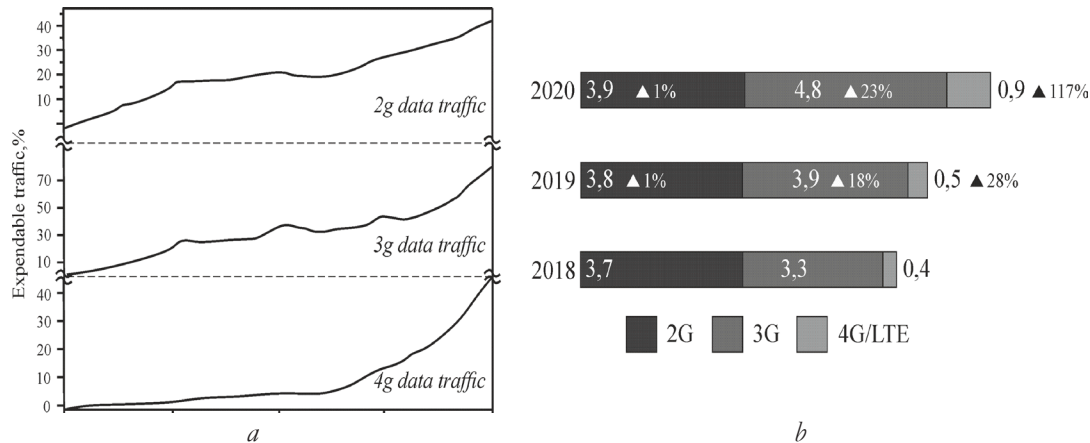


Fig. 2. (a) - The trend of growth in the total consumption of 2G/3G/4G traffic for the period from 2016 to 2020 in percentage terms; (b) - an increase in the number of BS cells for the period from 2018 to 2020.

traffic) is growing rapidly from year to year (Fig. 1b).

Over the past few years, the total consumption of mobile data has been increasing annually to a significant extent (Fig. 2a). In order to cope with the growth in the volume of transmitted information and ensure a high level of system reliability, mobile operators annually increase the number of hundreds of base stations (Fig. 2b) and the total throughput of communication channels (Fig. 3a). This has a positive effect on the increase in the average speed for subscribers (Fig. 3b).

Despite all the efforts being made to increase the number of base stations, improve coverage density, expand communication channels, the need for an increase in the

speed of information transmission leads to the need to increase the bandwidth of communication lines. The classical theorem of K. Shannon [16,17] allows you to theoretically describe the capacity of a communication channel:

$$\tilde{N} = \Delta f \log_2 \left(1 + \frac{P_c}{N} \right) = \Delta f \log_2 \left[1 + \frac{E_\delta}{N_0} \left(\frac{C}{\Delta f} \right) \right], \quad (1)$$

where Δf – the frequency band occupied by the system, P_c – the average signal power, N – the average noise power, E_δ – the bit energy, N_0 – the spectral density of the noise power.

Based on expression (1), it follows that there are two possible ways to solve the problem of increasing the capacity of communication lines. The first solution is to increase the average signal power P_c in

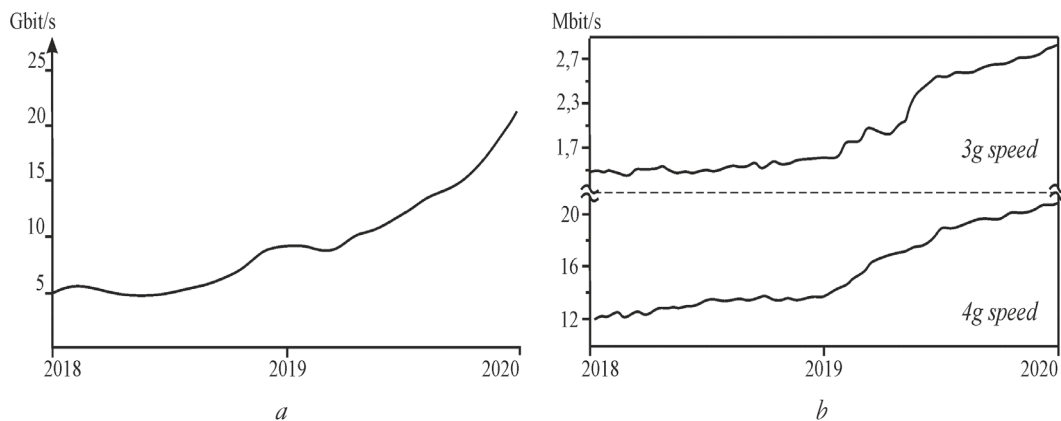


Fig. 3. (a) - Increase in the throughput of communication channels for the period from 2018 to 2020; (b) - an increase in the average subscriber speed for the period from 2018 to 2020.

relation to the total energy of noise and interference. The second is an increase in the capacity of the communication channel due to the expansion of the frequency band Δf occupied by the signal.

3. EFFECT OF ELECTROMAGNETIC RADIATION ON HUMAN BIOLOGICAL SYSTEM

To assess the interaction of electromagnetic radiation with a biological environment, it was decided to use SAR (Specific Absorption Rate) - specific absorbed power within the environment [18]. SAR (2) is defined as the ratio of the absorbed power in a given cell to the weight of biological tissue in it:

$$SAR = \frac{\sigma |E|^2}{\rho}, \quad (2)$$

where σ (S/m) - electrical conductivity, ρ (kg/m³) - material density, E (V/m) - electric field strength.

SAR is set by national and international standards. The SAR limit in the US is 1.6 W/kg, and in Europe it is 2.0 W/kg as set by the International Commission on Non-Ionizing Radiation Protection (ICNIPR) [19]. Analyzing the effect of electromagnetic radiation on the human body, the most interesting area is the head area, as it is the closest to the radiation source - a mobile phone.

The HFSS (High Frequency Structure Simulator) simulation software was used to calculate the SAR parameter based on the finite element method. A three-dimensional multilayer model consisting of skin (4 mm), skull (4.5 mm) and brain (50 mm) is considered as the initial model of the human head (**Fig. 4a**). The total estimated area of human tissue was 200×200 mm.

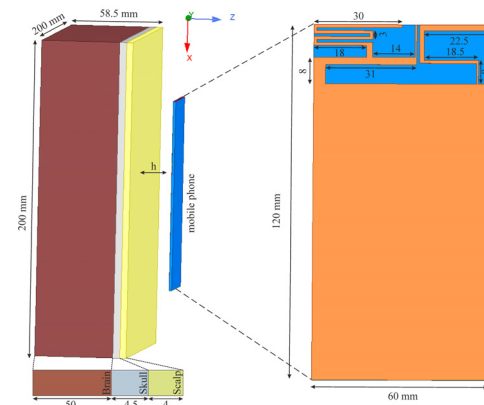


Fig. 4. (a) Three-layer model; (b) Dimensions of antenna structure (unit: mm).

The radiation source was a designed flat monopole antenna, the type of which is quite common in the design of 2G 3G/4G mobile devices [20-22]. The advantage of such an antenna is its low weight, ease of installation and low manufacturing cost. The antenna is designed on an FR4 dielectric substrate with a relative permittivity (ϵ_r) of 4.4 and a loss tangent (δ) of 0.2. The thickness of the substrate used was 1.6 mm. The upper conductive copper coating was 0.036 mm thick. The dimensions and dimensions of the antenna are shown in Fig. 4b.

To calculate the electrical parameters of human tissues, as a rule, the fourth-order Cole-Cole model is used [23].

$$\epsilon_r^* = \epsilon'_r - j\epsilon''_r = \epsilon_{r\infty} + \sum_{n=0}^4 \frac{\Delta\epsilon_m}{1+(j\omega\tau_n)^{1-\alpha}} + \frac{\sigma_i}{j\omega\epsilon_0}, \quad (3)$$

where ϵ_r^* – the complex relative permittivity; ϵ'_r – relative dielectric constant (real part of ϵ_r^*); ϵ''_r – loss factor (imaginary part of ϵ_r^*); $\epsilon_{r\infty}$ – dielectric constant at the field frequency; $\Delta\epsilon_m$ – increment in the relative permittivity; α – relaxation distribution time; ϵ_0 – dielectric constant of vacuum; σ_i – ionic conductivity; ω – angular frequency.

In our case, the values of the electrical parameters of the head tissues given in [21]

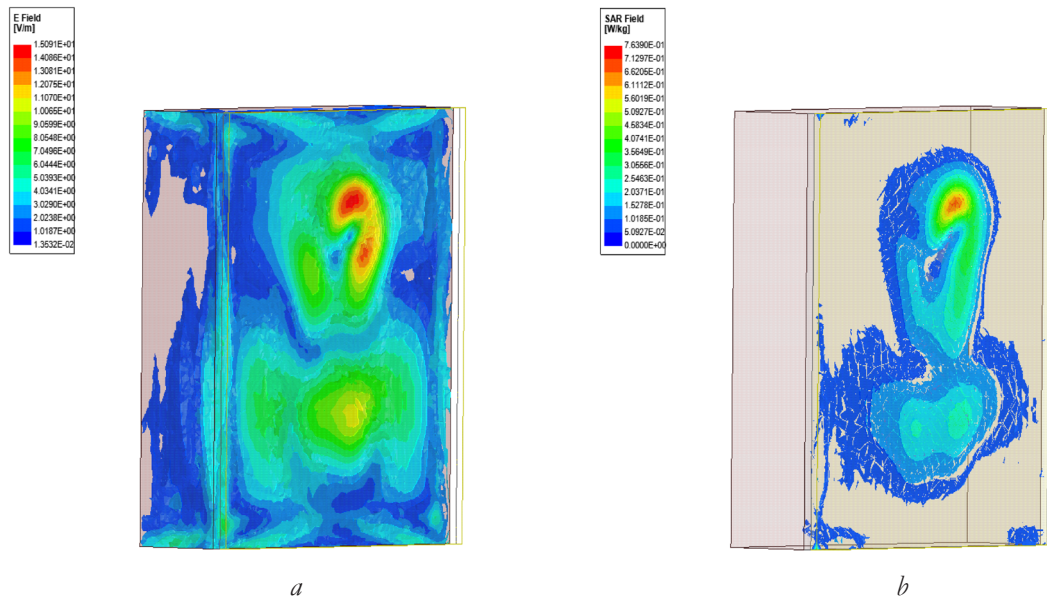


Fig. 5. Three-dimensional distribution of electromagnetic fields in the tissues of the head at a radiation power of 1 W,
(a) the distribution of the electromagnetic field; (b) SAR distribution.

for a frequency of 2600 MHz were taken as a basis. Fabric density values (kg/m^3): 1100 - for leather; 1850 - for the skull; 1030 - for the brain. The dielectric constant of the skin - 42.645, the skull - 11.293, the brain - 42.330. Conductivity (S/m) of skin - 1.684, skull - 0.424, brain - 1.603.

SAR distribution for the headform was calculated at 2600 MHz. As a comparative analysis, the antenna excitation power was 1

W (Fig. 5), which usually corresponds to the maximum usable power in the GSM standard, and 7 W (Fig. 6). The radiation source was located at a distance of 2 cm from the human head model.

At 1 Watt, the maximum SAR values do not exceed 0.763 W/kg for the skin, 0.53 W/kg for the skull and 0.33 W/kg for the brain (Fig. 5b). It should be noted that most of the incident energy is absorbed by the

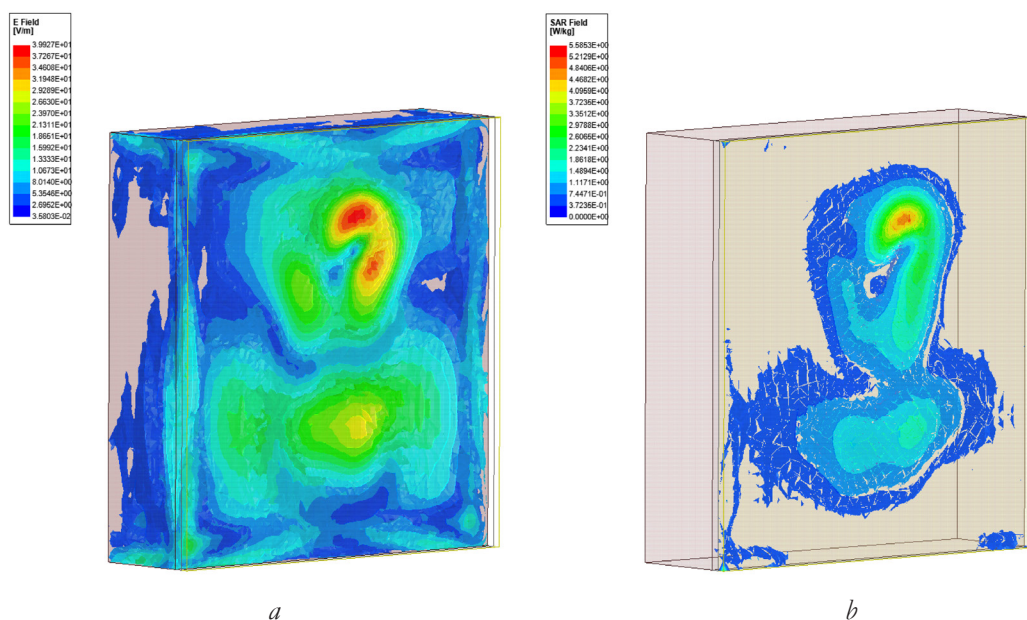


Fig. 6. Three-dimensional distribution of electromagnetic fields in the tissues of the head at a radiation power of 7 W, (a) distribution of the electromagnetic field; (b) SAR distribution.

scalp tissue. The closer the radiation source is to the head, the greater the harm from the electromagnetic effect of a mobile phone to the tissue of the human head. The highest values of the electric field strength (Fig. 5a) are observed on the surface of the human skin, in comparison with the brain and bone tissue, similar to SAR. The obtained values clearly demonstrate the possibility of using the simulated antenna as an element for a mobile phone device.

With an increase in the power of the emitter to 7 W, a sharp increase in the values of SAR (Fig. 6a) and electric field strength (Fig. 6b) is observed for all layers of the head tissue. The maximum SAR values for skin are 5.583 W/kg, for the skull - 3.23 W/kg, for the brain - 2.08 W/kg. The calculated data obtained indicate that the maximum permissible values of the specific absorbed power inside the human body are exceeded [19].

As can be seen from Figs 5 and 6, with an increase in the power of the radiation source by 7 times, the maximum SAR exceeds the allowable level according to the ICNIPR standard and is 2.08 W/kg for the human brain.

As an example, let us determine the bandwidth of the communication channel according to formula (1). To determine the signal-to-noise ratio (SNR), the useful signal power (P_u) values of 1 W and 7 W were selected, which translated into decibels is 30 dB and 38.45 dB, respectively. The noise power for both cases was $N = 5$ dB. The bandwidth of the communication channel was $\Delta f = 10$ MHz, which is standard for the territory of the Russian Federation, for the 4G/LTE frequency range (2500 - 2690 MHz). As a result of the calculation, the throughput of communication lines

(\tilde{N}) was 83.093 Mbit/s and 111.125 Mbit/s, for a signal power of 1 W and 7 W, respectively. A 7-fold increase in power gave an increase of $\sim 33\%$, which is not so significant. It follows from this that the method of increasing the throughput of communication channels by increasing the signal power of the receiving-transmitting device of the subscriber's terminal is unacceptable from the point of view of electromagnetic safety and insignificant in the context of the global problem of growing demand for expanding communication lines.

4. MODERN SOLUTIONS IN MOBILE COMMUNICATIONS SYSTEMS, 5G TECHNOLOGY

The solution to the problem of increasing the throughput of communication channels by increasing the signal power in relation to the total energy of noise and interference, by increasing the radiated power of the subscribers' terminals is not possible, due to the increase in the negative effect of electromagnetic radiation on the human body. Therefore, the best way to solve this problem is to expand the frequency band, in particular, the transition to 5G technology. 5G currently uses 160, 200, and 100 MHz bandwidths in the frequency range 2515 - 2675 MHz, 3.4 - 3.6 GHz and 4.8 - 4.9 GHz, respectively [24]. However, the frequency resources of these spectrum intervals are not unlimited and in the future there will be a number of problems associated with the limitations of the used frequency spectrum.

Currently, active work is underway to develop and conquer the millimeter wavelength range. The millimeter dimensions of the antennas and the frequency range

of tens of gigahertz make it possible to significantly increase the energy potential in millimeter-wave radio channels [25]. Nokia has carried out a number of experiments with data transmission at 70 GHz and 80 GHz. The initial results demonstrated the ability of the 5G system to provide reliable coverage and high performance of an experimental mobile communication system [26]. Samsung and Huawei also have some success in the development and creation of equipment for a new generation of mobile systems, qualitatively not inferior to the developments of Nokia [27,28]. Ericsson was able to achieve a data transfer speed of 5 Gb/s [29], and Samsung even announced that it had reached a speed of 7.5 Gb/s [27], which gives hope for the possibility of a significant increase in the data transfer speed and the introduction of new technologies in the near future.

5. CONCLUSION

In this article, by means of numerical simulations, the SAR values and the distribution of the electromagnetic field for a three-layer human head model at a frequency of 2600 MHz, at various powers of the radiation source, have been obtained. Calculated results show that an increase in power up to 7 W, with a distance from the head to a mobile phone of 2 cm, significantly increases the SAR values and amounts to 5.583 W/kg for the skin, 3.23 W/kg for the skull, 2.08 W/kg for the brain. ... Considering the reference ICNIRP limit of 2 W/kg, the increase in power is unacceptable from the point of view of the negative impact on the human body. In addition, an increase in power to 7 W gave an increase in channel capacity by only $\sim 33\%$, which is not significant in the

context of the global problem of growing demand for expanding communication lines. The results thus obtained provide valuable information for designing devices and assessing the effects of an electromagnetic field.

The optimal solution to the problem of expanding the bandwidth of information transmission channels is the transition to the millimeter frequency range. This, in turn, will make it possible to use the existing spatial, frequency redundancy when receiving, and transmitting information, which will open up some ways to raise the energy potential in millimeter-wave radio channels.

REFERENCES

1. Yuan Y, Lu Y, Cho TE, Ye C, Alyaqout A, Liu Y. The Missing Parts from Social Media-Enabled Smart Cities: Who, Where, When, and What? *Annals of the American Association of Geographers*, 2019, 1-14, doi: 10.1080/24694452.2019.1631144.
2. Sung W-T, Hsiao S-J. The Application of Thermal Comfort Control Based on Smart House System of IoT. *Measurement*, 2019:106997, doi: 10.1016/j.measurement.2019.106997.
3. Primova HA, Sakiyev TR, Nabiyeva SS. Development of medical information systems. *Journal of Physics: Conference Series*, 2020, 1441:012160, doi: 10.1088/1742-6596.1441.1.012160.
4. Huang M, Liu A, Xiong NN, Wang T, Vasilakos AV. An Effective Service-Oriented Networking Management Architecture for 5G-Enabled Internet of Things. *Computer Networks*, 2020, 173:107208, doi: 10.1016/j.comnet.2020.173.107208.

5. Li T, Zhao M, Wong KKL. Machine learning based code dissemination by selection of reliability mobile vehicles in 5G networks. *Computer Communications*, 2020, 152:109-118, doi: 10.1016/j.comcom.2020.01.034.
6. HuangM, Liu Y, Zhang N, Xiong NN, Liu A, Zeng Z, Song H. A Services Routing Based Caching Scheme for Cloud Assisted CRNs. *IEEE Access*, 2018, 6:15787-15805, doi: 10.1109/access.2018.2815039.
7. Velasquez K, Abreu DP, Curado M, Monteiro E. Service placement for latency reduction in the internet of things. *Annals of Telecommunications*, 2016, 72(1-2):105-115, doi: 10.1007/s12243-016-0524-9.
8. Liu Y, Liu X, Liu A, Xiong NN, Liu F A Trust Computing-based Security Routing Scheme for Cyber Physical Systems. *ACM Transactions on Intelligent Systems and Technology*, 2019, 10(6):1-27, doi: 10.1145/3321694.
9. Wang J, Wang F, Wang Y, Wang L, Qiu Z, Zhang D, Guo B & Lv Q. HyTasker: Hybrid Task Allocation in Mobile Crowd Sensing. *IEEE Transactions on Mobile Computing*, 2019, 19(3):598-611, doi: 10.1109/tmc.2019.2898950.
10. Liu X, Liu A, Wang T, Ota K, Dong M, Liu Y, Cai Z. Adaptive data and verified message disjoint security routing for gathering big data in energy harvesting networks. *Journal of Parallel and Distributed Computing*, 2020, 135:140-155, doi: 10.1016/j.jpdc.2019.08.012.
11. Khalid O, Khan IA, Rais RNB, Malik AW. An Insight into 5G Networks with Fog Computing. *Fog Computing*, 2020, pp. 505-527, doi: 10.1002/9781119551713.ch20.
12. Christopher B, Mary YS, Khandaker MU, Jojo PJ. Empirical study on specific absorption rate of head tissues due to induced heating of 4G cell phone radiation. *Radiation Physics and Chemistry*, 2020:108910, doi: 10.1016/j.radphyschem.2020.108910.
13. ICNIRP Guidelines, Guidelines for limiting exposure to time-varying electric, magnetic, and electromagnetic fields (up to 300 GHz). *Health Phys.*, 1998, 74:494-522.
14. IEEE Standard for Safety Levels with Respect to Human Exposure to Radio Frequency Electromagnetic Fields, 3 kHz to 300 GHz. *IEEE Std C95.1-2005* (Revision of IEEE Std C95.1-1991), 2006, 1–238.
15. Bhargava D, Leeprechanon N, Rattanadecho P, Wessapan T. Specific absorption rate and temperature elevation in the human head due to overexposure to mobile phone radiation with different usage patterns. *International Journal of Heat and Mass Transfer*, 2019, 130:1178-1188, doi: 10.1016/j.ijheatmasstransfer.2018.11.031.
16. Chen XM, Mak PU, Pun SH, Lam C-T, Che UK, Li JW, Du M. Initial investigation of channel capacity for galvanic coupling human body communication. *9th Biomedical Engineering International Conference (BMEiCON)*, 2016, doi: 10.1109/bmeicon.2016.7859612.
17. Feng M, Wu L. Special non-linear filter and extension to Shannon's channel capacity. *Digital Signal Processing*, 2009, 19(5):861-873, doi: 10.1016/j.dsp.2009.03.003.
18. Hirata A, Funahashi D, Kodera S. Setting exposure guidelines and product safety standards for radio-frequency exposure at frequencies above 6 GHz: brief review.

- Ann. Telecommun.*, 2019, 74:17-24, doi: 10.1007/s12243-018-0683-y.
19. Ahmed MI, Ahmed MF. A Wearable Flexible antenna integrated on a Smart Watch for 5G Applications. *Journal of Physics: Conference Series*, 2019, 1447:10-12, doi: 10.1088/1742-6596.1447.1.012005.
20. Cihangir A. *Antenna designs using matching circuits for 4G communicating devices*. Université Nice Sophia Antipolis, English, 2014.
21. Li Y, Lu M. Study on SAR Distribution of Electromagnetic Exposure of 5G Mobile Antenna in Human Brain. *Journal of Applied Science and Engineering*, 2020, 23(2):279-287.
22. Zhang HH, Yu GG, Liu Y, Fang YX, Shi G, Wang S. Design of Low-SAR Mobile Phone Antenna: Theory and Applications. *IEEE Transactions on Antennas and Propagation*, 2020:1–1, doi: 10.1109/tap.2020.3016420.
23. Gabriel S, Lau RW, Gabriel C. The dielectric properties of biological tissues: III. Parametric models for the dielectric spectrum of tissues. *Physics in Medicine and Biology*, 1996, 41(11):2271-2293.
24. Xiaofeng J, Xiaotao X, Junjie L. Performance Evaluation of Key Performance of 5G Mobile Communication System And Development Countermeasures. *Journal of Physics: Conference Series*, 2020, 1518, doi: 10.1088/1742-6596.1518.1.012077.
25. Polushin PA, Samoylov AG. Izbytochnost' signalov v radiosvyazi. Pod red. A.G. Samoylova. [Redundancy of signals in radio communications], *Radiotekhnika*, 2007, 256 (in Russ.).
26. Hattab G, Visotsky E, Cudak M, Ghosh A. Toward the Coexistence of 5G MmWave Networks with Incumbent Systems beyond 70 GHz. *IEEE Wireless Communications*, 2018, 25(4):18-24, doi: 10.1109/mwc.2018.1700436.
27. Gozalvez J. Samsung Electronics Sets 5G Speed Record at 7.5 GB. Mobile Radio. *IEEE Vehicular Technology Magazine*, 2015, 10(1):12-16, doi: 10.1109/mvt.2015.2390931.
28. Gozalvez J. 5G Tests and Demonstrations. *IEEE Vehicular Technology Magazine*, 2015, 10(2):16-25, doi: 10.1109/mvt.2015.2414831.
29. He Z, Wu W, Chen J, Li Y, Stackenäs D, Zirath H. An FPGA-based 5 Gbit/s D-QPSK modem for E-band point-to-point radios. *14th European Microwave Week 2011: "Wave to the Future"*, EuMW 2011 - 41st European Microwave Conference, 2011:690-692, doi: 10.23919/EuMC.2011.610175.

IN MEMORY OF

ARKADY B. TSEPELEV

PACS 01.60.+q

DOI: [10.17725/rensit.2021.13.104](https://doi.org/10.17725/rensit.2021.13.104)



On March 22, 2021, at the age of 72, Arkady Borisovich Tsepelev, Doctor of Physical and Mathematical Sciences, a full member of the Russian Academy of Natural Sciences, professor, leading researcher at the A.A. Baikov Institute of Metallurgy and Materials Science (IMET) RAS, member of the Academic Council of IMET RAS, professor of the Moscow Engineering Physics Institute (National Research Nuclear University), specialist in the field of solid state physics and radiation and space materials science died suddenly.

Arkady Borisovich was born on October 08, 1949 in Engels, Saratov Region, in the family of an aviation colonel of the Soviet Army. In 1966, after graduating from high school, he entered the Voronezh Polytechnic Institute at the Faculty of Physics and Technology, from which he graduated in 1971, receiving a diploma with honors as an engineer in metallurgical physics.

From 1971 to 1973, he studied at the graduate school at the A.A. Baykov Institute of Metallurgy of the Academy of Sciences of the USSR, and since 1974 he was assigned to work at this institute, in which he went from an engineer to a leading researcher.

In 1983, Arkady Borisovich defended his Ph.D. thesis on "The role of radiation-stimulated processes

in changing the mechanical properties of stainless steels", and in 2001 - his doctoral thesis on "Dynamic change in mechanical properties in metallic materials under cyclic irradiation".

The main direction of his scientific research throughout his scientific career was associated with radiation physics of solids. The research results were repeatedly reported at the largest international and domestic scientific forums, in many of which he took part not only as a speaker, but also as a member of the Program and Organizing Committees. Arkady Borisovich has published more than 200 printed scientific papers in leading scientific journals in our country and for abroad.

Along with extensive research activities, Arkady Borisovich Tsepelev constantly conducted various scientific and organizational work as a scientific secretary of the Scientific Council for New Structural Materials of the Russian Academy of Sciences, a member of the editorial boards of the RAS journals "Physics and Chemistry of Materials Processing" and "Perspective Materials", as well as their executive secretary and deputy editor-in-chief. He was also a member of the editorial board of RENSIT journal and an active reviewer.

Since 2008, Arkady Borisovich Tsepelev has combined work at the Russian Academy of Sciences with teaching at the Moscow Engineering Physics Institute (National Research Nuclear University), lectured and taught practical classes on the course "Radiation-stimulated processes in solids and nanomaterials".

In 2019, Arkady Borisovich Tsepelev was elected a corresponding member of the Russian Academy of Natural Sciences, and in 2020 he was elected a full member of the Russian Academy of Natural Sciences in the Department of Radioelectronics, Nanophysics and Information Technologies Problems.

The bright memory of Arkady Borisovich Tsepelev, a remarkable scientist and teacher, a man of the highest moral qualities, will forever remain in the hearts of all his friends and colleagues.

RENSIT journal editorial board

From the Editor

This section of the journal publishes a material about the defense of **the first doctoral dissertation in our country on graphene topics**. Scientific consultant of the work - Doctor of Chemical Sciences, Full Member of the Russian Academy of Natural Sciences, Professor Gubin Sergei Pavlovich, Chief Researcher of the N.S. Kurnakov Institute of General and Inorganic Chemistry of the Russian Academy of Sciences, scientific head of "AkKo Lab" LLC. *

Graphene oxide - a new electrode nanomaterial for chemical current sources

Denis Yu. Kornilov

"AkKo Lab" LLC, <http://www.akkolab.ru/>

Moscow 107143, Russian Federation

E-mail: kornilovdenis@rambler.ru

Received March 18, 2021, peer-reviewed March 22, 2021, accepted March 24, 2021

Abstract: The material of the defense of the dissertation for the degree of Doctor in Engineering Sciences is presented. The relevance of the search for new electroactive nanomaterials for current sources of portable electronic equipment in conditions of its high energy consumption with its miniaturization and increase in performance is noted, the object of research is characterized – graphene oxide as a cathode material for lithium chemical current sources, the formulation of research tasks is formulated, the physicochemical methods of analysis.

Keywords: chemical current sources, cathode materials graphene oxide

UDC 541.1: 539.23

For citation: Denis Yu. Kornilov. Graphene oxide is a new electrode nanomaterial for chemical current sources. RENSIT, 2021, 13(1):105-108. DOI: 10.17725/rensit.2021.13.105.

15 of December 2020, at the Dissertation Council 05.07 of the D.I. Mendeleev Russian University of Chemical Technology, Denis Kornilov defended his dissertation work on the theme "Graphene oxide – a new electrode nanomaterial for chemical current sources" for the degree of Doctor in Engineering Sciences. In the report of the doctoral candidate was outlined: the relevance of the search for new electroactive nanomaterials for current sources of portable electronic equipment in the conditions of its high energy consumption with its miniaturization and increased speed was noted, the object of research – graphene oxide as a cathode material for lithium chemical current sources

(in contrast to transition metal oxides – cathode materials of widespread use), formulated the research tasks, the physical and chemical methods of analysis are listed. The object of research was a wide range of functional materials based on graphene oxide with different stoichiometry, size and shape:

- Graphene oxide films obtained from the dispersion of graphene oxide by the spin-coating method;
- Graphene oxide films obtained from the dispersion of graphene oxide by the dip-coating method;
- Films of reduced graphene oxide obtained from by directed heating of the surface of the graphene oxide dispersion;

- Spheres made of reduced graphene oxide obtained by drip injection of heated oil into the graphene oxide dispersion;
- Aerogels based on graphene oxide obtained by freeze-drying of highly concentrated dispersion of graphene oxide.

Here it is necessary to clarify that in accordance with the ISO/TS 80004-13 dictionary of the International Organization for Standardization [1], graphene materials include:

- Graphene is a monolayer of carbon atoms;
- Double-layer graphene is a material consisting of two layers of carbon;
- Three-layer graphene is a material consisting of three layers of carbon atoms;
- Few-layers graphene is a material containing from 3 to 10 layers of carbon atoms;
- Turbostratic double-layer graphene – double-layer graphene whose layers are in an arbitrary azimuthal orientation relative to each other;
- Graphene oxide (GO) is a chemically modified graphene produced by the oxidation and exfoliation of graphite;
- Reduced graphene oxide (RGO) is a form of graphene oxide after chemical, thermal, microwave, photochemical, photothermal, or microbial/bacterial recovery.

This classification is consistent with publications [2-4] which indicated the presence of practically confirmed unique properties in graphene materials consisting of no more than 10 layers of carbon atoms.

For example, single-layer graphene has a large surface area, which is 2640 m²/g [5],

high electrical conductivity, high mobility of current carriers ($2 \cdot 10^5$ cm²/(V·s)) [6].

Graphene can withstand currents exceeding 10⁷ A/cm² [7].

Graphene is a strong material with Young's modulus of 1TPa [8], it can undergo 20% deformation without breaking the crystal lattice [9].

The thermal conductivity of a graphene monolayer is 5000 W/(m·°C) [10], which is 10 times higher than the values of copper.

The optical transmission coefficient in graphene reaches 97.7% [11].

Also, the advantages of graphene materials include the possibility of obtaining them in various ways, while various methods and technological techniques for the synthesis of graphene materials allow them to be obtained in various forms, which can be attributed to another advantage of this material. Changes in the properties of the objects of study from the conditions of production, heat treatment conditions, and the reducing agents used were established and analyzed.

The obtained results served as the basis for the study of the possibility of using graphene oxide in secondary chemical current sources (lithium-ion batteries) as an additive in cathode materials, namely, coatings of reduced graphene oxide on the surface of microparticles of the cathode material of the composition $\text{LiNi}_{0.33}\text{Mn}_{0.33}\text{Co}_{0.33}\text{O}_2$ flows; corrosion inhibitor of the current collector, namely, a coating of graphene oxide on the surface of an aluminum current collector; an anode material in the form of hollow spheres of reduced graphene oxide; cathode materials in the form of films, powders and aerogels of graphene oxide. At the same time, the results of electrochemical studies of graphene oxide allowed us to establish high values of the electrochemical potential and high values of

the irreversible energy intensity depending on the surface area of the objects of study, which indicated the direction of further research, namely, to establish the influence of the degree of oxidation and surface area on the energy-intensive characteristics of graphene oxide aerogels.

Also, complex physicochemical research methods were used to analyze graphene oxide-based aerogels as they were discharged. As a result, it was found that during the electrochemical reduction of graphene oxide, particles of about 20 nm in size are formed on its surface, the number of which increases when the discharge reaches 2.0 V, and when the voltage reaches 1.5 V, a sufficiently dense layer of particles is observed, which, when the voltage reaches 1 V, takes the form of a solid massive coating. The results allowed us to determine the products formed during the discharge on the surface of graphene oxide, which in turn served as the basis for establishing current-forming processes. Based on the obtained data, the theoretical capacity of graphene oxide reaching 3292 C was calculated, which exceeds the values of the discharge capacity of known cathode materials used in the production of primary chemical current sources by 1.5-3 times.

Thus, the presented chain of consecutive interrelated studies of graphene oxide allowed us to establish the practical possibility of its direct application as a high-energy cathode material of primary lithium chemical current sources since practical results were obtained at the level of 721 mAh/g. Based on the practical results, the model of the prototype of the electrochemical cell of the lithium|graphene oxide system is calculated, the specific (weight) energy intensity of which exceeds the values of the specific (weight) energy intensity of the galvanic cells

produced by industry by 25-400%, which in turn is of important socio-economic and economic importance since high-energy-intensive primary chemical current sources open up wide opportunities for autonomous electronic devices.

The results obtained in the dissertation work create a foundation for technical and technological solutions for the using of graphene oxide, and information about the electrochemical properties of functional materials based on graphene oxide will be in demand in the laboratory and technological processes when designing and predicting the characteristics of innovative chemical current sources, the introduction of which will make a significant contribution to scientific and technical development.

REFERENCES

1. ISO/TS80004-13 Nanotechnologies - Vocabulary - Part 13: Graphene and related two-dimensional (2D) materials 2017, p. 21.
2. Ferrari A. Science and technology roadmap for graphene, related two-dimensional crystals, and hybrid systems. *Nanoscale*, 2015, 7:4598-4810. DOI: 10.1039/C4NR01600A.
3. Wick P. Classification framework for graphene-based materials. *Chem. Int. Ed.*, 2014, 53:7714-7718. DOI: 10.1002/anie.201403335.
4. Bianco A. All in the graphene family - a recommended nomenclature for two-dimensional carbon materials. *Carbon*, 2013, 65:1-6. DOI: 10.1016/j.carbon.2013.08.038.
5. Worsley MA, Olson TY, Lee JR. High surface area, sp²-cross-linked three-dimensional graphene monoliths. *The Journal of Physical Chemistry Letters*, 2011,

- 2(8):921-925. DOI: 10.1021/jz200223x.
6. Baringhaus J, Ruan M, Edler F. Exceptional ballistic transport in epitaxial grapheme nanoribbons. *Nature*, 2014. DOI: 10.1038/nature12952.
 7. Sun H, Xu K, Lu G. Graphene-supported silver nanoparticles for pH-neutral electrocatalytic oxygen reduction. *IEEE Trans. Nanotechnol.*, 2014, 13(4):789-794.
 8. Papageorgiou DG. Mechanical properties of graphene and graphene-based nanocomposites. *Progress in Materials Science*, 2017, 90:75-127.
 9. Meyer J, Geim A, Katsnelson M. The structure of suspended graphene sheets. *Nature*, 2007, 446:60-63. DOI: 10.1038/nature05545.
 10. Balandin AA. Superior thermal conductivity of single-layer graphene. *Nano Lett.*, 2008, 8(3):902-907.
 11. Li X, Zhu Y, Cai W. Transfer of large-area graphene films for high-performance transparent conductive electrodes. *Nano Lett.*, 2009, 9(12):4359-4363.